Departamento de Física de Materiales
Facultad de Ciencias
Universidad Autónoma de Madrid

Design, fabrication and characterization of photonic crystals on III-V compounds: from classical to quantum light sources

Luis Javier Martínez Rodríguez

Instituto de Microelectrónica de Madrid
Centro Nacional de Microelectrónica
Consejo Superior de Investigaciones Científicas

Tres Cantos, October 2009

Departamento de Física de Materiales
Facultad de Ciencias
Universidad Autónoma de Madrid

Design, fabrication and characterization of photonic crystals on III-V compounds: from classical to quantum light sources

Memoria presentada por
D. Luis Javier Martínez Rodríguez
para optar al Grado de Doctor en Ciencias Físicas

Dirigida por: Dr. Pablo Aitor Postigo Resa

Tutor: Dra. Luisa Eugenia Bausá López

Instituto de Microelectrónica de Madrid
Centro Nacional de Microelectrónica
Consejo Superior de Investigaciones Científicas
Tres Cantos, October 2009

To my parents, Luis and Fina

A mis padres, Luis y Fina

6.36311 Que el sol saldrá mañana es una hipótesis; y esto quiere decir: no *sabemos* si saldrá.

Ludwig J. J. Wittgenstein

... en ciencia lo que se pretende es describir y (en la medida de lo posible) explicar la realidad.

Karl R. Popper

Agradecimientos

Después de tanto tiempo en todo aquello que da lugar a la presentación de una Tesis, llega el momento más agradable y merecido, el de agradecer a todas aquellas personas y organismos que han contribuido al desarrollo de este proyecto. Sin ellas, no hay duda de que no hubiera sido posible. En primer lugar quisiera agradecer a los distintos ministerios e instituciones que han aportado la financiación necesaria a través de distintas becas asociadas a proyectos, beca I3P y contratos.

En segundo lugar debo agradecer a mi director de Tesis Dr. Pablo Aitor Postigo el haberme dado la oportunidad de trabajar en el campo de los cristales fotónicos y por toda la ayuda que me ha brindado. Tampoco olvido a la Dra. Luisa E. Bausá, mi tutora en la UAM.

A esta Tesis han sido tres las personas que han aportado una ayuda inestimable: Alfonso Alija (siempre nos quedará París), en los comienzos. El Dr. Benito Alén en la parte final sobre todo por su inestimable ayuda en las medidas de caracterización óptica; ¡cuántas horas, día y noche!. E Iván Prieto (PG), todo ilusión y entusiasmo, dispuesto y servicial en todo momento desde su llegada al Instituto (tal vez nos quede el surrealismo).

Al Dr. Juan Pedro Silveira y al Dr. Antonio García-Martín; con Juan Pedro tuve la oportunidad de acercarme a la caracterización óptica y con Antonio, tomé contacto con las simulaciones de PCs.

Al Dr. José V. Anguita quien siempre ha estado dispuesto a prestar su ayuda, en especial, en lo referente a todo lo que ataña a los diversos equipos utilizados en los procesos de fabricación.

A todos los profesionales del grupo de MBE, representados en la imagen de la Prof. Luisa González.

A Rubén Álvarez (RAS), por la lectura minuciosa y paciente del manuscrito, con sus comentarios y sugerencias. Además, por esas largas horas de terapia biunívoca tan necesaria en el desarrollo de una tesis (aquellos maravillosos años).

A nuestros colaboradores del Instituto de Nanotecnología de Lyon, al Dr. Chistian Seassal y al Dr. Pierre Viktorovitch, así como al Dr. Matteo Galli, al Dr. Juan Francisco López-Galisteo, al Dr. Dario Gerace y al Prof. Lucio Claudio Andreani de la Universidad de Pavia, por toda la ayuda prestada en los distintos trabajos

realizados.

A Josep, a Guillermo y al Prof. Juan Martínez Pastor de la Universidad de Valencia con quienes tuve la ocasión de acercarme a un confocal y participar en las medidas de hilos en microcavidades a baja temperatura.

A Eva, a Anna Nowak, al Dr. Dipankar Sarkar, al Dr. H. van der Meulen y al Prof. José Manuel Calleja de la UAM por darme la oportunidad de participar en las medidas de cavidades con anillos cuánticos.

A Ridah Sabouni (persona incansable) y a la Prof. Evelyn L. Hu quien me dio la oportunidad de visitar su laboratorio y poder aprender tanto en tan poco tiempo, en especial, en lo relativo a la fabricación de cristales fotónicos en GaAs y a su metodología de trabajo. Tanto dentro como fuera del ámbito profesional siempre estaré en deuda por el trato recibido.

Al personal de administración del IMM, en especial a Margarita y a Mercedes, por haber hecho más llevaderos los entretejidos trámites burocráticos.

A los compañeros del Instituto, Pablo, Chon, Javi, Javier Martínez, Fuster, Piñera, Maki, D. Ramos, Mr. Kaldirim, Llorens, A. Rivera, Bautista, Ripi, Albariño, Mariane, Nuria, Carlos, Florian (Sinclair), y alguno más que siempre se olvida.

No me quisiera olvidar finalmente de todas aquellas personas que desde fuera del ámbito académico han contribuido a esta tesis, tal vez de manera indirecta, con su aliento; por ello, no menos importante: Paco, Blanca, Pilar, Ismael, Luis R. V., José Luis (Marqués de Sargadelos), y como no, mi familia, Fina, Luis, Javier, Isabel, Modesta, Pili y Pepe.

Mi más sincera gratitud a todos.

Resumen

Los cristales fotónicos son estructuras con una modulación periódica de la constante dieléctrica que permiten el control de la luz en tamaños del orden de la longitud de onda en el material. Un caso particular de estas estructuras son los cristales fotónicos bidimensionales que están constituidos por una guía de ondas plana cuya constante dieléctrica ha sido modulada periódicamente. En este caso, el confinamiento en la direccion vertical se consigue por reflexión total interna y en el plano mediante la modulación periódica.

Uno de los principales propósitos de esta Tesis ha sido la mejora de las propiedades de confinamiento de estructuras de cristal fotónico. Con este objetivo se han fabricado distintas estructuras como la red Fase-Suzuki en la parte superior de un reflector de Bragg. En esta estructura se ha medido un aumento importante de la intensidad de emisión (hasta 7 veces) para una banda plana. Siguiendo el principal propósito de la Tesis, se han usado distintas estructuras fotónicas para obtener nuevos dispositivos láser en la nanoescala. Para ello, se ha desarrollado un proceso de fabricación capaz de proporcionar cavidades de cristal fotónico con factores de calidad altos. Una nueva red, la hibrida triangular-grafito, ha sido fabricada en una configuración diseñada para la emisión vertical. Se ha medido emisión láser con factores de calidad altos ($\simeq$12000). Además, se ha demostrado emisión láser en régimen de excitación continua en microcavidades the cristal fotónico usando una sola capa de hilos cuánticos de InAs/InP. Para ello se han fabricado cavidades L7 con factores de calidad de hasta 55000. En excitación pulsada a medida que la potencia de excitación aumenta, se ha medido emisión láser con varios picos cuyas separaciones están en el rango de meV y en el rango de los μeV.

Por último, se ha conseguido la emisión de "luz cuántica". Para ello se ha desarrollado un proceso de fabricación de cristales fotónicos en GaAs. Estos resultados pueden ser útiles para el desarrollo en el futuro de fuentes eficientes de fotones individuales para dispositivos ópticos en tecnología de la información y computación cuánticas.

Conclusiones

Los resultados de esta Tesis se resumen en los siguientes puntos:

1. Se ha medido un aumento de la intensidad de emisión de entre 4 y 7 veces (1.9 veces para k=0) para la "banda plana" de la red Fase-Suzuki en la parte superior de un reflector de Bragg. Esta nueva estructura fotónica da lugar a una estructura de bandas fotónicas en la que los modos transversales magnéticos (TM-like) aparecen de modo natural debido a la ruptura de la simetría especular.

2. Se ha medido emisión láser con factores de calidad altos ($\simeq$12000) en estructuras de cristal fotónico de área extendida con emisión vertical usando la red hibrida triangular-grafito. Esta estructura proporciona un nuevo mecanismo de formación de modos de Bloch en torno al punto Γ.

3. Se ha obtenido emisión láser en el régimen de excitación continua en cavidades de cristal fotónico L7 con una sola capa de hilos cuánticos de InAs/InP. Se han medido factores de calidad hasta $\simeq$55000 en estructuras con un factor de calidad intrínseco de 70000. Se ha demostrado que el alineamiento espacial entre los hilos cuánticos y la cavidad juega un papel importante. El comportamiento bajo excitación pulsada muestra formas de línea asimétricas y separaciones entre picos en rangos de meV y de μeV a medida que la potencia de excitación se incrementa.

4. Se han diseñado y fabricado microcavidades de cristal fotónico con anillos cuánticos de In(Ga)As/GaAs embebidos; la emisión de la red de cristal fotónico ha mostrado emisión de fotones individuales. Este proceso abre el camino para futuros trabajos en tecnología de estado sólido de información cuántica y computación cuántica.

Abstract

Photonic crystals (PCs) are structures with a periodic modulation of the dielectric constant. PCs enable the control of light at the scale of the wavelength of the light in the material. A particular sort of these structures are the "two dimensional" PCs, which are made of a slab which dielectric constant has been modulated in a periodic way. In that case, the light is confined in the vertical direction by index guiding and in-plane by the effect of the periodic modulation of the dielectric constant.

One of the main goals of this Thesis has been the enhancement of the optical confinement of the fabricated photonic crystal structures. With this aim, different structures have been fabricated like the Suzuki-phase on top of a Bragg reflector. An important enhancement of the emission intensity (up to seven times) has been measured for a flat band. Different photonic structures aiming to enhance the confinement of the light have been used for the obtention of new laser devices in the nanoscale. A fabrication process on InP capable to provide high Q photonic crystal microcavities (PCMs) has been developed. A new hybrid triangular-graphite lattice has been fabricated in a configuration designed for vertical laser emission with high quality factors (Q$\simeq$12000). Continuous wave laser emission on PCMs using a single layer of InAs/InP quantum wires (QWrs) has been demonstrated in L7-PCMs, with Qs up to 55000. Moreover, under pulsed excitation multipeak emission (with splittings in the meV and in the μeV ranges as the excitation power is increased) has been measured.

Finally, an insight in the emission of "quantum light" has been achieved. For this purpose a fabrication process of PC structures on GaAs material has been developed. These results can be useful for the future development of efficient single photon sources which are building blocks for quantum information optical devices and quantum computing technology.

Contents

Chapter 1

Introduction

In this chapter a brief introduction to the photonic crystals is given. The concept of photonic crystal, photonic band structure, photonic band gap, photonic crystal microcavity and photonic crystal waveguides are presented. A short description of the light-matter interaction on microcavities is showed too. Finally, an overview and the goals of this Thesis is presented.

1.1 Photonic crystals

Current information society needs to handle a continuously increasing amount of information data. A way to overcome the bandwidth limitations of the electrical wiring and reduce the high energy consumption is to use light. This provides a way to manage a huge amount of data at high speeds and with lower consumption of energy [1, 2]. In this context, one of the most promising platforms to manipulate light are the photonic crystals (PCs). Due to their possibilities of tailoring the light in the micro-nanoscale (small footprint) the PCs constitute an important springboard for integrated nanophotonic networks [3], fast information processing, computing by optical means [4, 2] and potential quantum computing networks [5, 6]. Motivated by these facts, research in the field of PCs has suffered an exponential growth since the

proposals of E. Yablonovich [7] and S. John [8] in the late eighties. [7, 8], although the research in the field of periodic dielectric structures began some time before [9]. The work of [7] was focused in the control of spontaneous emission in periodic dielectric structures while Ref. [8] was about the localization of the light by disorder in certain dielectric material. This was the onset of the PCs research field.

The PC's can be defined as *a medium with a periodic modulation of the dielectric constant in 2D or 3D with high-index-contrast.*[a]

This periodic modulation of dielectric constants gives rise to a *photonic band structure* in an analogous way to what happens in solid state physics where a periodic potential gives the electronic band structure. This band structure can present a *photonic band gap* (PBG), i.e., a forbidden region where the photons cannot propagate. In that case, if the optically active electronic transitions overlaps with the PBG, a strong suppression of the spontaneous emission happens [7, 10], even in the case of 2D-PC slabs [11]. When a defect is created in the PC structure a strong confinement of the light can be obtained in a volume of the order of a cubic wavelength of the light in the material ($\sim (\lambda/n)^3$) [12, 13]. If the dielectric medium shows suitable properties, different effects and functionalities can be obtained like Purcell effect [14] and vacuum Rabi splitting [15, 16, 17], which can be applied to efficient single photon sources [18, 19], low-threshold lasers [20, 21, 22], high-speed modulation lasers [23], and so on. If a channel is created in the dielectric periodic structure, a lossless waveguide is obtained [24, 25] where, for example, by the suitable design for slow-light propagation, the creation of an ultracompact optical switch can be obtained [26]. Combining PC microcavities (PCMs) and PC waveguides (PCWs), multifunctional devices can be also obtained [27, 28, 29]. Instead, a PC device fabricated on silicon has allowed for the dynamic tuning of the Q of a PCM [30], that may help to stop the light in dielectric structures or obtaining large frequency shifts in linear media [4]. In addition, monolithic coupling of a PCM laser to a passive waveguide has been demonstrated [31] as well as the coupling of a PCM single photon source to another PCM through a PCW [32].

One important characteristic of the photonic band (PB) structure is the existence of

[a] A discussion about the use of the "Photonic crystal" term can be found at Ref. [9].

points where the group velocity ($\mathbf{v}_g = (d\omega/d\mathbf{k})_{k_0}$) is zero, which yields the formation of a standing wave that produces a resonant mode [33]. Depending of the band-edge point properties different lasing capabilities can be obtained: in-plane lasing [34], vertical lasing emission [35, 36] or the tailoring of the far-field emission pattern [37]. Moreover, the use of these features has allowed the obtention of high efficiency of extraction in blue-light emitting diodes [38].

A way to improve the capabilities of two-dimensional (2D) PCs is to combine them with a bottom Bragg reflector. This offers the possibility of improving the lasing characteristics of band-edge lasers [39], control the coupling from the free space modes to the guided modes [40], improve the vertical emission directionality of PCMs [41], and fabricate ultra-compact VCSELs [42, 43].

Due to the compatibility with the current semiconductor technology, the research has been mainly focussed in 2D-PC slabs where the PCs present the in-plane PBG and the confinement in the vertical direction is achieved by index guiding. With the improvements in fabrication technology, it is expected an important increase in the number of results in 3D-PCs, where for example the spontaneous suppression rate can be improved from 10 to 100 times [44], and the light can propagate without loss by optical scattering [2, 13]. In addition, the combination of 2D-PCs waveguides sandwiched in 3D "self-assembled" silicon PCs may allow for the fabrication of large area PCs and entirely on silicon [45].

1.2 Photonic band structure

Maxwell equations and eigenvalues equations[b]

The behavior of the electromagnetic waves in matter is given by the Maxwell equations. In a linear, homogeneous and isotropous medium without light sources (non free charges and currents), not magnetic ($\mu = 1$), where ϵ is real (lossless) and independent of the frequency, under the assumption of time harmonic dependence,[c]

[b]The section 1.2: *Photonic band structure* is based in the book of J.D. Joannopoulos *et al.* [46]

[c]Although theses simplifications could seem very restrictive are applied to a large number of

$\mathbf{H}(\mathbf{r},t) = \mathbf{H}(\mathbf{r})e^{-i\omega t}$, the macroscopic Maxwell equations in the magnetic field formulation[d] take the form:

$$\nabla \cdot \mathbf{H}(\mathbf{r}) = 0, \tag{1.1}$$

and the rotational equations summarize in

$$\nabla \times \left(\frac{1}{\epsilon(\mathbf{r})} \nabla \times \mathbf{H}(\mathbf{r}) \right) = \left(\frac{\omega}{c} \right)^2 \mathbf{H}(\mathbf{r}), \tag{1.2}$$

that constitutes the *master equation*. Solving this equation, taking into account Ec. 1.1 (transversality requirement) [46], provides $H(\mathbf{r})$. The electric fields can be obtained directly by the relation:

$$\mathbf{E}(\mathbf{r}) = i \frac{c}{\omega} \frac{1}{\epsilon(\mathbf{r})} \nabla \times \mathbf{H}(\mathbf{r}). \tag{1.3}$$

The master equation 1.2, using the definition of the operator $\widehat{\Theta}$:

$$\widehat{\Theta} = \nabla \times \left(\frac{1}{\epsilon(\mathbf{r})} \nabla \times \right), \tag{1.4}$$

can be transformed into an eigenvalues equation:

$$\widehat{\Theta}\mathbf{H}(\mathbf{r}) = \left(\frac{\omega}{c} \right)^2 \mathbf{H}(\mathbf{r}) \tag{1.5}$$

$\widehat{\Theta}$ is a linear and Hermitian operator. This allows us to use some concepts extracted from quantum mechanics and solid state physics. The eigenvalues of a Hermitian operator are real and its eigenvectors are orthogonal (if the eigenvalue are not degenerate).

Discrete translational symmetry

The discrete translational symmetry of the dielectric function $\epsilon(\mathbf{r}) = \epsilon(\mathbf{r}+\mathbf{R})$, where $\mathbf{R}$ belongs to the Bravais lattice of the PC [47], gives rise to the Bloch theorem and,

electromagnetic problems.

[d] An analogous formulation can be done in terms of the electric field ($\mathbf{E}(\mathbf{r})$).

hence, the solutions of the master equation are of the form:

$$\mathbf{H_k}(\mathbf{r}) = e^{i\mathbf{k}\cdot\mathbf{r}}\mathbf{u_k}(\mathbf{r}) \tag{1.6}$$

where the eigenvectors are labeled with $\mathbf{k}$, that belongs to Brillouin zone [47], and the $\mathbf{u_k}(\mathbf{r})$ functions have the periodicity of the Bravais lattice $\mathbf{u_k}(\mathbf{r}) = \mathbf{u_k}(\mathbf{r}+\mathbf{R})$. A direct consequence of the Bloch theorem is that $\mathbf{k}$ is preserved in a periodic system. For each value of $\mathbf{k}$ it is expected to be found an infinite set of solutions (modes) with discretely spaced frequencies, that can be labeled by the *band index* n. Since $\mathbf{k}$ is a continuous parameter, the frequency of each band n is expected to change in a continuous way too. In this way the solutions of the master equation are described by a set of continuous functions $\omega_n(\mathbf{k})$; that are the so-called *photonic band structure*.

Added to the translational symmetry, the dielectric constant can have another symmetries, like rotational symmetry, mirror symmetry, etc. These symmetries constitute the *point group* of the PC. Since the functions $\omega_n(\mathbf{k})$ have the same symmetries is not necessary to consider all the $\mathbf{k}$ vectors of the Brillouin zone, only those that do not show a symmetry relationship. These vectors constitute the *irreducible Brillouin zone*.

Solving the master equation, with $\mathbf{k}$ lying in the irreducible Brillouin zone, the Bloch modes $\mathbf{H}_{\mathbf{k},n}$ and the photonic bands $\omega_n(\mathbf{k})$ are obtained. If the PC presents the suitable features, like large enough index contrast and periodicity, a region where the density of states is null and where the photons can not propagate appears in the PB structure. This range of $\omega_n(\mathbf{k})$ is called the *photonic band gap*. Fig. 1.1 a) shows the PB structure of 2D PC conformed by a triangular lattice of holes in dielectric material. Partial PBGs (non-complete gaps) are observed for each polarization and a complete (full gap) PBG where the PBGs for both polarizations overlap. In the case of 3D-PCs a frequency region where the light propagation is inhibited in all space directions can be also obtained [48, 49].

Mirror symmetry

An important class of a symmetry operation, which is the especial utility, is the mirror symmetry. This let us, under certain conditions, to split the master equation,

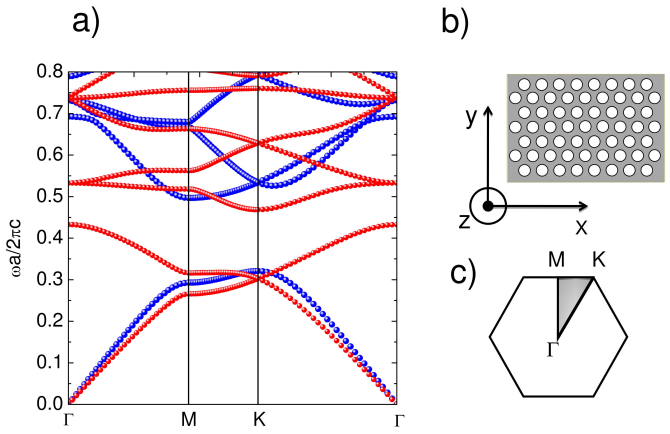

Figure 1.1: a) Two-dimensional photonic band structure of the triangular lattice of air holes in a dielectric matrix. The parameters of the structure are: the hole radius $r = 0.45a$, the lattice parameter a, and the dielectric constant, $\epsilon = 10.1$. Blue color: even modes $\sigma_{xy} = +1$ (TE-like). Red color: odd modes $\sigma_{xy} = -1$ (TM-like). b) PC structure layout. c) Brillouin zone of the PC.

into two equations, one for each polarization. This provides direct information about the symmetry of the mode and it can help in the numerical resolution of the eigenvalues equation. Let us consider the mirror symmetry M. An example of mirror symmetry is the reflection in the plane YZ $(x, y, z) \longrightarrow (-x, y, z)$. The mirror symmetry operator can be defined as $\widehat{\sigma}_M \mathbf{f}(\mathbf{r}) = M\mathbf{f}(M\mathbf{r})$. The possible eigenvalues of the mirror operator $\widehat{\sigma}_M$ are ± 1. If we apply the operator twice we recover the initial system. It can be demonstrated that if the $\widehat{\sigma}_M$ operator commutes with the operator $\widehat{\Theta}$, $M\mathbf{r} = \mathbf{r}$, and $M\mathbf{k} = \mathbf{k}$, then the solutions of the master equation can be classified either as even or odd (separation of modes) [46].

To illustrate the utility of this symmetry operation let us consider an "ideal" 2D PC. This structure has in-plane periodicity (XY plane) and it is infinity in the vertical direction (z). Then, our system is invariant over a mirror operation (M) in the XY

plane $(x, y, z) \rightarrow (x, y, -z)$[e], where the in-plane propagation is considered ($M\mathbf{k}$=$\mathbf{k}$). If we apply the mirror symmetry $\widehat{\sigma}_{xy}$, over the H and E fields, taking into account that the magnetic field is a ***pseudo vector*** and the electric field is a ***vector*** [50], we obtain: $\widehat{\sigma}_{xy}H = (-H_x, -H_y, H_z)$ and $\widehat{\sigma}_{xy}E = (E_x, E_y, -E_z)$. Then, any PC mode can be classified either as even (E_x, E_y, H_z) or odd (H_x, H_y, E_z). The former are usually called TE-modes, whereas the latter are called TM-modes. It is important to remark that this analysis also holds for symmetric 2D PC slabs taking as symmetry plane the one that crosses the center of the slab in the Z direction.

Time-reversal symmetry and scaling properties of the Maxwell equations

Two important properties are derived from the *time-reversal* symmetry and the scalability of Maxwell equations. The first one is a symmetry property of the band structure: $\omega_n(\mathbf{k}) = \omega_n(-\mathbf{k})$, which means that the PB structure has inversion of symmetry even if the PC does not. The second property, based on the fact that there is not a fundamental length in the Maxwell equations, means that if the problem (master equation) is solved for one longitudinal scale, then it is solved for all. Rescaling our system, represented mathematically by a variable change, $\mathbf{r}' = s\mathbf{r}$, the "new" dielectric function is $\epsilon'(\mathbf{r}') = \epsilon(\mathbf{r})$ and the new solutions of the master equation are: $\mathbf{H}'(\mathbf{r}') = \mathbf{H}(\mathbf{r}'/s)$ and $\omega' = \omega/s$, where $\mathbf{H}(\mathbf{r})$, and ω, are the solutions of the problem before being scaled. For example if we increase the size of the physical system by a factor of 2 the new frequency will be $\omega/2$. This invariance let us to express band structures in dimensionless units: $\omega a/2\pi c$ versus $\mathbf{k}a$.

1.3 Two-dimensional photonic crystal slabs

A 2D-PC slab[f] consists on a 2D waveguide which is periodically patterned. In that case, the optical in-plane confinement is due to the 2D-PC pattern and in the third direction is given by index guiding (total internal reflection). If the upper

[e]The symmetry operation is independent of the origin chosen since the system is infinite in the vertical direction.

[f]It is important to note that the properties of the 2D-PC slabs are different of the "ideal" 2D-PCs due to the behavior induced by the waveguide (finite size in the vertical direction).

cladding and lower cladding of the waveguide have the same dielectric constant the structure is symmetric with respect to a plane (XY) across the center of the slab. This let us to classify the modes either as even (TE) or odd (TM) as indicated in the previous section. If the cladding dielectric constants are different, the modes cannot be separated. However, it has been experimentally demonstrated that, in weakly asymmetric slabs, the PB structure can be approximated by the one of the PC slabs embedded in a material with the average dielectric constant of the upper cladding and lower cladding [51, 52]. Fig 1.2 shows two examples of 2D PB structure calculated by the guided-mode expansion (gme) [53]. An important feature of this kind of structures is the light line (upper green lines in the plots of Fig. 1.2) of the cladding material. This line is the limit between the Bloch modes: the ones that lie below the light line are confined by index guiding (non radiative, with no intrinsic losses); and the ones lying above the line are leaky modes (with intrinsic losses by diffraction out of the plane).

1.3.1 Photonic band-edges

As it was mentioned before there exist a collection of points in the band structure which are specially useful. These are the band-edge points where the group velocity is zero giving place to a standing wave (the density of states is strongly increased $\sim {v_g}^{-1}$). The arrows in the Fig. 1.2 indicate two of these points.

In Fig. 1.2 a) the band-edge point indicated lies below the light line and the mode is truly confined. Nevertheless, it is important to note that in fabricated structures the lateral size of the PC is finite giving place to in-plane losses and decreasing the Q of the Bloch mode. This point (K_1) was used by C. Monat *et al.* [34] to obtain laser emission at 1.55 μm. Laser emission using other band-edge points below the light line in the triangular and square lattices has been demonstrated [35, 54].

At the Γ point the Bloch modes always lie above the light line (Fig. 1.2 b)). Due to both the symmetry of the lattice and the Bloch modes at the Γ point, the mode can be coupled or uncoupled to the radiative modes [55, 56]. By a suitable choice of the Bloch mode at the Γ point, confinement in the vertical direction is obtained, despite

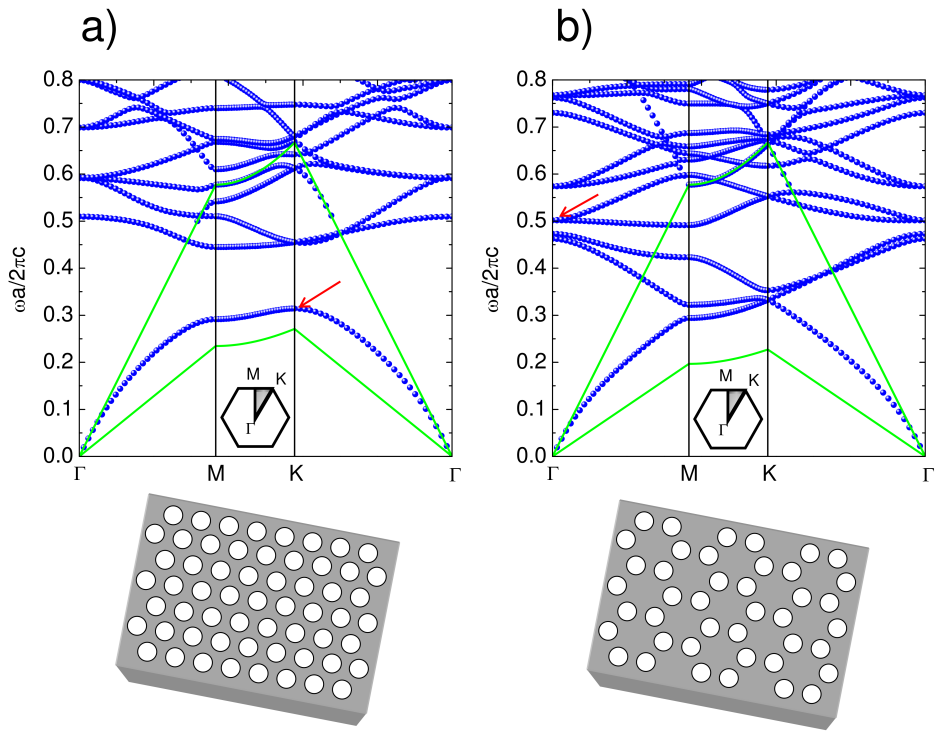

Figure 1.2: Photonic band structure of a 2D photonic crystal slab of InP ($\epsilon = 10.1$) on air for the triangular lattice a) and the graphite lattice b). The parameter of the structures are: a) hole radius r/a=0.35 and slab thickness d/a=0.45. b) hole radius r/a=0.15 slab thickness d/a=0.32. Only even modes ($\sigma_{xy} = +1$) are plotted. Green lines are the light lines of the cladding and average core materials.

the point lies above the light line. In finite size structures (realistic structures) there are two mechanisms for optical losses: the first one is the in-plane losses in an analogous way to what happens in finite size structures based on band-edge points below the light line. The second is due to that the mode contains components $k_{||} \neq 0$ and optical losses in the vertical direction can appear, as the mode is strictly confined only for $k_{||} = 0$. Another important feature of these Γ-point structures is that their emission is almost vertical as $k_{||} \simeq 0$. This kind of confinement has been used to obtain laser emission in PC slabs with different lattice geometry [35, 36, 57]; this kind of devices are sometimes named photonic-crystal surface-emitting lasers (PC-SELs).

The Γ-point PC structures have been used to obtain laser emission on structures with low-index contrast in the vertical direction [33, 58] and with electrical pumping. It is remarkable that single mode emission is obtained despite the large area of the device; by suitable design of the PC structure the far field patterns can be tailored [37]. In addition, photonic devices based in this especial point of the PB structure have demonstrated laser emission on GaN based at blue-violet wavelengths [59], hight light extraction efficiency (73%) on GaN based LEDs [38] and the enhancement of the efficiency in solar cells [60].

1.3.2 Photonic crystal microcavities

If a defect is created in the periodic PC structure a set of states appears inside the PBG of the PC, which are called "defect states" or if they are produced by a "cavity", "cavity modes". Depending on the characteristic of such defect, the number of cavity modes is different. In an ideal 3D-PC, where the propagation is inhibited in all the space the directions, the light is perfectly confined. In a 3D PCM with finite size the "quality" of the confinement will depend on the number of PC layers surrounding the defect [61]. In our 2D-PCs slabs case, the microcavity modes have intrinsic losses due to the incomplete band gap of the 2D-PC structures.[g] For the characterization of a microcavity mode two main parameters are commonly used: the quality factor (Q) and the modal volume (V).

The Q, a dimensionless parameter, accounts for temporal confinement of the cavity. It can be considered as the number of optical cycles before the cavity energy decays by a factor $e^{-2\pi} \approx 2 \times 10^{-3}$. It is important to note that the value of Q corresponds with $\nu/\Delta\nu$, being ν the mode frequency and $\Delta\nu$ the width at half maximum. In 2D-PC slabs Q commonly decomposes in two components, one called the vertical quality factor (Q_v) and the other the in-plane quality factor ($Q_{||}$). The first one depends intrinsically on the cavity mode (its value changes slightly with the number or surrounding layers) whereas the second one strongly depends on the number of in-plane PC layers, and its value increases exponentially with it (an example of this

[g] The defect created breaks the translational symmetry of the PC, then **k** is not conserved and the photonic mode can couple with the radiative modes above the light line with the same frequency.

can be found in Ref. [62]). The relationship between Q and its components is given by:

$$\frac{1}{Q} = \frac{1}{Q_v} + \frac{1}{Q_{||}} \tag{1.7}$$

The variable V is a measurement of the spacial confinement of the microcavity mode and, as it happens with Q, is an important parameter that appears in QED problems. The modal volume [63] is defined as:

$$V = \iiint \frac{\epsilon(\mathbf{r}) \mid \mathbf{E}(\mathbf{r}) \mid^2}{max\left(\epsilon(\mathbf{r}) \mid \mathbf{E}(\mathbf{r}) \mid^2\right)} d^3\mathbf{r} \tag{1.8}$$

The value of V is expressed typically in units of $(\lambda/n)^3$. One of the main properties of the PC microcativies is that they confine the light in volumes in the order of V$\sim (\lambda/n)^3$, considered by some authors as close to the minimum limit for an optical cavity [64]. This allows for the possibility of obtaining high ratios of Q/V with moderate values of Q that can be used to improve the properties of single photon sources [18] and to get high rate modulation lasers [23].

Another parameter related to the cavity mode is the effective index of the mode (n_{eff}). This gives a value of how big is the overlap between the cavity mode and the dielectric material. A low value of n_{eff} indicates a large overlap between the mode and the air region. The effective index is defined as:

$$n_{eff}^2 = \frac{\iiint \epsilon(\mathbf{r}) \mid \mathbf{E}(\mathbf{r}) \mid^2 d^3\mathbf{r}}{\iiint \mid \mathbf{E}(\mathbf{r}) \mid^2 d^3\mathbf{r}} \tag{1.9}$$

In 2D-PC slabs a large effort has been done to optimize the Q of the PCMs. One of the most commonly used methods consists of driving out of the light line the Fourier components of the mode [65, 12]. In this way, several structures have been designed and fabricated. Silicon based PCM with an intrinsic $Q \sim 1.5 \times 10^7$ with $V \simeq (\lambda/n)^3$ have been designed and fabricated in non active medium with a Q measured of $Q_m = 2.5 \times 10^6$ [66]. Furthermore, GaAs-based PCs, cavities with $Q \sim 3 \times 10^6$ have been designed and fabricated (in non active medium) with a measured $Q_m = 7 \times 10^5$ [67]. On InP based materials, cavities based on slow Bloch

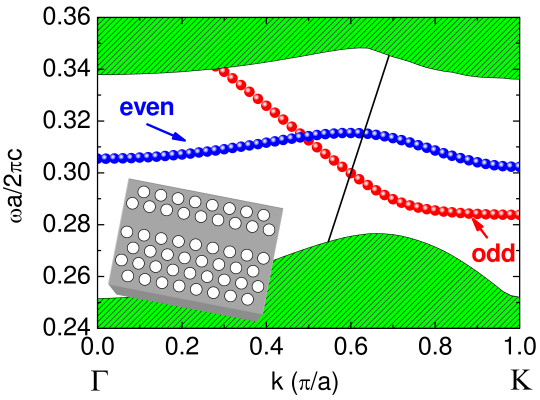

Figure 1.3: Dispersion relationship of a W1 photonic crystal waveguide on InP material. The parameters of the simulation are: hole radius r/a=0.27 and slab thickness d/a=0.539. Blue color: even modes ($\sigma_{yz} = +1$). Red color: odd modes ($\sigma_{yz} = -1$). Only even modes σ_{xy}=+1 (TE-like) are plotted. Black line is the light line of the cladding core material.

modes below the light line have been designed with $Q = 5\times10^7$ and $V \simeq 4(\lambda/n)^3$ [68]. It is important to note that the measured Q in structures with active material strongly decreases with respect to the ones without active medium. For example, on a PC containing InAs/GaAs quantum dots, $Q = 5\times10^6$ whereas the measured value is $Q_m = 1.9\times10^4$. The highest Q measured on InP material are $Q \sim 5\times10^4$ [69, 70], both in samples with active material, using PCMs with designed Q$\geq 7\times10^4$. There are few cases designed to obtain very low values of V, amongst them a remarkable case is the M0 PCM that has a $Q \sim 10^5$, with a $V \sim 0.15(\lambda/n)^3$ [71, 64].

1.3.3 Photonic crystal waveguides

If a linear defect is created in the PC structure, the light can propagate along the defect giving place to a channel for the light. In that case the symmetry holds along the PC and **k** is preserved along that direction. This provides to modes that are truly confined despite the non complete PBG of the 2D-PC slab. Fig. 1.3 shows the dispersion relationship of a 2D-PC waveguide created by filling up the holes of

a triangular lattice along the ΓK direction of the PCs. Although the modes below the light line are truly confined, in real structures the fabrication imperfections causes optical losses [72, 73]. In theory, only the channels created in 3D-PCs present lossless propagation [13]. Useful devices can be obtained using PCWs. For example, waveguides with very low group velocity of propagation can be obtained [74]. In an analogous way, for band-edge PC structures, laser emission can be obtained in points below [75] and above de light line [76]. Recently, an efficient source of single photons using on InAs/GaAs QDs coupled to a W1-PCW has been created [77].

1.3.4 Photonic crystals combined with a Bragg reflector

One of the drawbacks of 2D PCs slabs is the coupling of the guide modes to the radiative modes. A way to overcome this is combining the 2D-PC slabs with a bottom Bragg reflector. These new structures are named "2.5-D" photonic structures [78], and they offer the possibility of tailoring the coupling between the guide modes and the radiative modes. Using this approach, a compact VCSEL, where the top mirror of the VCSEL is replaced by a PC membrane, has been fabricated [79]. This device can be also used for in-plane emission [40]. Moreover, an ultracompact device where both Bragg reflectors are replaced by PC membranes has been proposed [43].

The improvement of the lasing properties of the Γ-point laser by a reduction of the threshold through an increment of the Q using a bottom Bragg reflector has been demonstrated [39]. In that case, there is a modification of the radiation pattern and, on the other hand, the coupling of resonant modes with radiative modes is notably reduced (increment of the Q). It must be noted that an important parameter is the spacing (d) between the PC membrane and the bottom Bragg reflector which must be kept $d \geq \lambda/2$ [39]. Depending on d, the value of Q oscillates between the minimum for $d = p\lambda/2$ and a maximum for $d = (2p+1)\lambda/2$, where p is an integer and λ is the wavelength of the resonant mode. Using a slow Bloch mode at the Γ-point with a bottom Bragg reflector, laser emission has been obtained in 2D-PC slabs with different PC symmetry. Using the graphite lattice laser emission with a single layer of InAs/InP quantum dots has been shown [80]. In addition, laser emission has been obtained in a 2D-PC lattice of dielectric rods in air using quantum wells as active

medium [81].

1.4 Light-matter interaction on microcavities

A way to introduce the light-matter interaction in microcavities is to consider the simplest case. It consists of a single two-level atom coupled to a single mode field. In solid state physics the role of the two-level atom can be played by an excitonic transition in a QD and the single mode field which can be a high Q mode of a PCM. In the *dipole approximation*, and *rotating wave approximation*, i.e., very fast and strong pulses are not considered, the problem is described by the *Jaynes Cummings* hamiltonian [82, 83]. The Hamiltonian of the system can be expressed as: $\widehat{H} = \widehat{H}_F + \widehat{H}_I$. The first term is the free Hamiltonian (non interaction between the atom and the cavity mode) and the second term represents the interaction atom-field. In the resonant case, when the frequency associated with the transition is the same than the resonant field, the eigenstates of the Hamiltonian can be expressed as a linear combination of the eigenstates of the Hamiltonian without the interaction term ($\widehat{H}_F$). The eigenstates of the interaction-free Hamiltonian are: $|n, e\rangle$, $|n+1, b\rangle$, where $\mid n, i\rangle = |n\rangle \bigotimes |i\rangle$, with $\mid n\rangle$ represents the field state (the number of photons, Fock state) and $|i\rangle$ the state of the atom, $|e\rangle$ for the excited state, $|b\rangle$ for the ground state. For each value of n there are two degenerated states ($|n, e\rangle, |n+1, b\rangle$) sometimes referred as *bare states*. Solving the Hamiltonian in each subspace "defined" by n, the eigenstates corresponding to $\widehat{H}_I$ are:

$$\mid n, \pm\rangle = \frac{1}{\sqrt{2}} \left(\mid n, e\rangle \pm \mid n+1, b\rangle \right), \tag{1.10}$$

sometimes called *dressed states*,where the eigenvalues are $\pm i\Omega_n$, with $\Omega_n = g\sqrt{n+1}$. g is the coupling constant between the radiation field and the atom [82]. For $n = 0$, the energy separation between the eigenvalues is $2g$, known as the vacuum Rabi splitting and Ω_n is the Rabi frequency. If the atom is initially in the excited state and the mode has exactly n photons, the probability to find the atom in the excited

state is given by [82]:

$$p_e = \mid \langle n, e \mid \Psi_n(t) \rangle \mid^2 = \frac{1}{2}\left(1 + \cos 2\Omega_n t\right) \tag{1.11}$$

This can be interpreted as the continuous oscillation between the electronic system (the atom) and the electromagnetic mode (cavity mode). In this way, considering the simplest case, we observe the strong change that can happen in the emission properties of an atom (emitter) coupled to a field (cavity mode). This points out that the emission spectrum of the emitter as well as the radiative lifetimes can be extraordinary modified by the cavity mode.

Weak coupling regime and Strong coupling regime

When we have a true system (for example, the previously mentioned: a quantum dot and a PCM) the phenomena of decoherence can appear. On one hand the photons can leak out the cavity and on the other hand the emitter can suffer other de-excitation than the emission of the photon in the cavity mode. Let us characterize those phenomena by the spectral width of the cavity mode γ_c and the emitter γ_e. The light matter coupling constant g, in the ideal case of perfect coupling between the cavity mode and the emitter (i.e, the emitter is placed in the maximum of the cavity electric field and the dipole orientation is parallel to the electric field) is given by [84]:

$$g = \frac{\mu}{\hbar}\sqrt{\frac{\hbar\omega}{2\epsilon_0\epsilon V}} \tag{1.12}$$

where μ is the module of the dipole momenta of the electronic transition, ω is the photon frequency, ϵ is the dielectric constant and V is the mode volume (defined by Ec. 1.8). The relation amount g, γ_c and γ_e, allows us to classify the different regimes of our system [84].

The weak coupling regime is defined by:

$$\gamma_c > g > \gamma_e \tag{1.13}$$

The strong coupling regime is defined by:

$$g > \gamma_c/4, \gamma_e/4 \tag{1.14}$$

Weak coupling regime and Purcell effect

When an emitter is placed inside a microcavity, its spontaneous emission rate is strongly modified and can be either enhanced or inhibited. In the weak coupling regime defined by Ec. 1.13 the spontaneous emission rate can be calculated by the Fermi golden rule considering a lorentzian density of states. The spontaneous emission rate relative to the spontaneous emission rate in the material without cavity is given by [18]:

$$\frac{\Gamma_0}{\Gamma_c} = F_P \left| \frac{\mathbf{E}(\mathbf{r}_e) \cdot \mu}{E_{max}\mu} \right|^2 \frac{1}{1 + 4Q^2 \left(\frac{\omega_c}{\omega_e} - 1\right)^2} \tag{1.15}$$

where the first term

$$F_p = \frac{3}{4\pi^2}\frac{Q}{V}\left(\frac{\lambda}{n}\right)^3 \tag{1.16}$$

depends only of the cavity mode properties. The second term represents the spacial overlap between the emitter and the cavity field, and the third factor represents the spectral overlap between the emitter and the cavity mode (ω_e and ω_c are, respectively, the angular frequency of the emitter and the cavity mode). In the case of the perfect spatial and spectral overlap the relationship is reduced to F_p, the well known Purcell factor, proposed by E. M. Purcell in 1946 [85]. The figure of merit of this process is $\propto Q/V$. Sometimes a fourth term (Γ_{PC}) is added to the Ec. 1.15 to take into account the effect of the PBG where the spontaneous emission is strongly inhibited [18]. In the case that the spectral width of the emitter is larger than the ones of the cavity mode (assuming the emitter and the cavity mode are in resonance), in Ec. 1.16, $1/Q$ has to be replaced by $1/Q + 1/Q_e$ [86, 87], being Q_e the quality factor of the emitter. If the emitter has a broadband emission, a small Purcell effect is expected.

Summarizing, if we have an emitter with a radiative time, for example an In(Ga)As QD, embedded in GaAs material, when the emitter is placed in a PCM, its radiative

lifetime will be decreased if its excitonic transition is in resonance with the cavity mode. On the other hand, if the transition is strongly detuned from the cavity mode, its radiative lifetime will be increased with respect to the same embedded QD in GaAs (without cavity).

Strong coupling regime and Vacuum Rabi splinting

If the relationship conditions 1.14 are fulfilled, the system can show a strong coupling regime and the emitter and the cavity mode exchange energy in a reversible and coherent way. The system can oscillate some cycles before the photon leaves the cavity. In that case of the strong coupling, for low power excitation ($n < 1$), the spectrum of the system is given by [84, 16]:

$$\Omega_{\pm} + i\Gamma_{\pm}/2 = \frac{\omega_c + \omega_e}{2} - i\frac{\gamma_c + \gamma_e}{4} \pm \sqrt{g^2 - \frac{1}{4}\left(\frac{\gamma_e - \gamma_c}{2}\right)^2} \tag{1.17}$$

where for $g > |\frac{\gamma_e - \gamma_x}{4}|$ the spectrum consists of two lines at frequencies $\Omega_{\pm}$ with average linewidths $\Gamma_{\pm}$. The splitting between both lines is $2\sqrt{g^2 - \frac{1}{4}\left(\frac{\gamma_e - \gamma_c}{2}\right)^2}$. The experimental way to measure that the system exhibits strong-coupling is to find an anticrossing between the cavity mode and the emitter transition [88]. Nevertheless, the pumping conditions play an important role in the observation of the strong coupling in solid state systems [89]. Finally, it is important to note that the figure of merit is $\propto Q/\sqrt{V}$.

In agreement with the previously mentioned conditions regarding the weak coupling and the strong coupling regimes, the engineering of the Q and V of PCMs, and the spectral and spatial overlapping of the emitter and the cavity field of the PCM is a mandatory task.

1.5 Semiconductor quantum nanostructures

In a semiconductor system, when its characteristic lengths are comparable with the Fermi wavelength of the carriers (λ_F) in the material, the quantum confinement

arrives. In these nanostructures, the carriers are confined spatially, which favors the overlapping between the wavefunction of the electron and hole that increases the excitonic character of the system. In addition, the density of states is strongly modified with respect to the bulk material [90]. The typical way to obtain this confinement effect in semiconductor materials (in a simple case) is to sandwich a layer of semiconductor (1D-confinement) with a semiconductor material of larger electronic band gap. Thus, if the thickness of the layer $\lesssim \lambda_F$, a confinement like a potential well in quantum mechanics is obtained [91] and, hence, the so-called QWs. One of the bests ways to fabricate this kind of structures is by molecular beam epitaxy (MBE)where the thickness of the layer can be controlled with sub-atomic layer accuracy [92].

The next step in the enhancement of the spatial confinement of the carrier are the QWrs. One dimensional nanostructure provides carriers confined in two space spatial dimensions (2D-confinement). These semiconductor nanostructures can be obtained by MBE on self-assembled [93] or isolated [94] forms. One particular characteristic of the QWrs is that their emission is polarized along the wire [95].

The last step is the three dimensional (3D) confinement of the carriers. In this case the material of lower band gap is surrounded in the three dimensions by the higher band gap material. In that case, we obtain the so-called QDs. These nanostructures present discrete energy levels [96] with a density of states given by a Dirac delta function. Due to their discrete energy levels, sometimes they are referred as *"artificial atoms"*.

The three kinds of semiconductor nanostructures most commonly used in semiconductor optoelectronic devices are: quantum wells (QWs), quantum dots (QDs) and quantum wires (QWrs). These nanostructures have provided a way to improve the characteristic of optoelectronic devices, and specially, diode lasers [97, 90]. On the other hand, they made possible the obtention of more exotic phenomena like Bose-Einstein condensation of exciton-polaritons [98, 99, 100]. In our case, the quantum nanostructures used in this Thesis are InAsP/InP QWs, InAs/InP QWrs embedded on InP material, an In(Ga)As QDs (with ring shape) in GaAs. The nanostructures in InP yield photoluminescence (PL) emission at 1.55 μm. The nanostructures in

GaAs give PL around 980 nm. These structures are the active material that provides enough gain as to obtain laser emission. It is important to note that the surface recombination of InP based devices is one or two orders of magnitude smaller than in GaAs based devices, which degrades the internal quantum efficiency on GaAs microcavity lasers [86].

1.6 Goal and overview of the Thesis

The goals of this Thesis can be summarized as follows:

1. To design, fabricate and characterize new photonic structures with improved performance for the confinement of light.
2. To apply such structures in new photonic devices such low threshold lasers, vertical emission lasers, and enhance their emission intensity.
3. To explore the new properties of active emitters embedded in highly confined photonic structures for quantum light emitters.

The overview of the Thesis is, by chapters:

Chap. 2 describes the development of the fabrication process of InP-based PC. After a careful design, a state-of-the-art fabrication process for PCs was obtained.

Chap. 3 describes the improvement in the optical properties of confinement of a PC structure with a Bragg reflector underneath. For this purpose, the Suzuki-phase PC structure was fabricated with and without a Bragg reflector, and their optical properties were characterized. A remarkable improvement in the intensity of emission was achieved.

Chap. 4 describes the obtention of laser emission using the triangular-graphite PC lattice to provide high Q values and vertical emission in wide area PC structures.

Chap 5 describes lasing action in the continuous and pulsed regimes of QWrs coupled to the fundamental mode of L7 PCM. High Q and low threshold lasing has been

obtained for both regimes.

Chap. 6 describes the fabrication process of PC structures on GaAs material as well as the optical characterization of such structures, where single photon emission has been measured.

Chapter 2

Fabrication of high quality factor photonic crystal microcavities in InP membranes combining reactive ion beam etching and reactive ion etching

The process of fabrication of high quality factor photonic crystal microcavities in slabs of InP with light emission at 1.5 μm is reported. It includes e-beam lithography, reactive ion beam etching with a CHF_3/N_2 gas mixture and reactive ion etching with a CH_4/H_2 and O_2 cycling. An InGaAs sacrificial layer is removed by chemical wet etching in order to obtain the photonic crystal membrane. Microphotoluminescense measurements have been performed to assess the quality of the fabricated structures. Quality factors up to $\simeq 30000$ and laser emission with thresholds of excitation pump power around 34 μW have been obtained in samples with InAsP/InP quantum wells as active material.

2.1 Introduction

Photonic crystal microcavities (PCMs) allow to confine the light in volumes in the order or less than a cubic wavelength [12, 71]. Their high quality factors (Qs) and small modal volume have shown the potential of PCMs for creating small size lasers [20], cavity quantum electrodynamics test beds [16], self-tuning lasers [22] till the basic elements of the integrated photonic crystal circuits [30, 101]. A high quality fabrication process, reliable, reproducible, and presenting high accuracy is mandatory for achieving such devices, focusing on minimizing the diffraction losses. In-plane shape inhomogeneities, variation of the size of the hole and variation in the position of the holes are parameters that increase the optical losses. These imperfections preserve the transversal symmetry of the slab. In addition, surface roughness, angled sidewalls and sidewall roughness produce the coupling between the even (TE-like) and the odd modes (TM-like) of the slab modes, and are also important sources of optical losses [102, 103][a].

Here the fabrication of PCMs in InP semiconductor slabs containing quantum wells (QWs) as active medium is described, which has been also used for the fabrication of PCM with InAs/InP quantum wires (QWrs) [104] and can be generally used for the fabrication of PCMs on InP material. We have used e-beam lithography combined with reactive ion beam etching (RIBE) with a CHF_3/N_2 gas mixture for transferring the e-beam resist pattern to a SiO_x hard mask layer. Reactive ion etching (RIE) with a CH_4/H_2 gas mixture and O_2 cycling is used to drill the semiconductor material. Finally, the PC membrane is released by wet etching in a $HF(1) : H_2O_2(1) : H_2O(20)$ solution. Optical microphotoluminescense (μ-PL) has been used to assess the quality of the PCMs. Qs up to 30000 have been measured in samples with QWs as active material. The development of this process will allow for the study of the emission and coupling properties of InAs quantum dots [105], recently obtained in our laboratory, embedded in high Q PCMs operating around 1.55 μm.

[a] Note that we are referring to "cool" cavity: a cavity without active material that provides the absorption (and emission) of light.

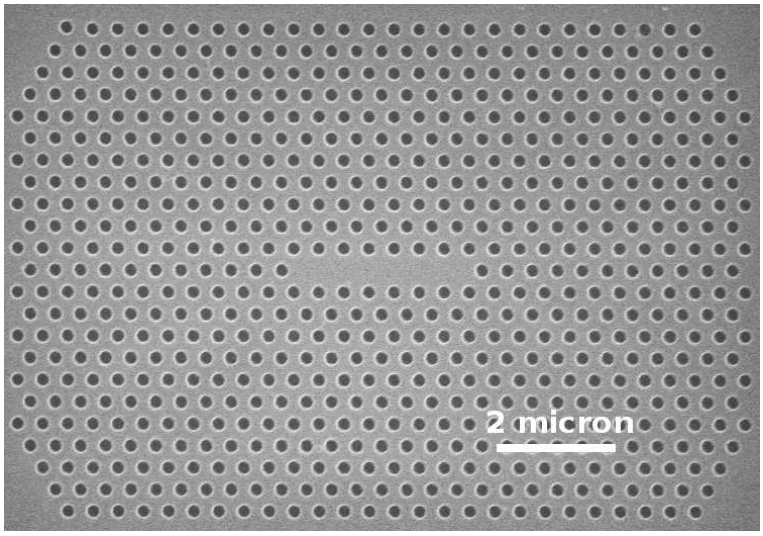

Figure 2.1: Scanning electron microscopy image of a L7 PCM.

2.2 Photonic crystal structure

A periodic lattice of holes with triangular symmetry has been selected as the PC structure. This lattice presents a large photonic bandgap for the TE-like polarization modes (even modes, $\hat{\sigma}_{xy} = +1$) [106]. We have fabricated the so-called L7 PCM [107, 108], which is created erasing seven holes along the $\Gamma - K$ direction of the lattice (Fig. 2.1 shows a scanning electron microscopy (SEM) image of the L7 PCM after the fabrication process). This cavity belongs to the Ln type of PCMs, with optical modes that can be classified either as even or odd with respect to the longitudinal plane across the center of the cavity [62]. In our case the cavity parameters (lattice constant, radius hole ratio, and slab thickness) of the L7 PCM are the following: $a = 440$ nm, $r/a = 0.28$ and $d = 237$ nm. This structure presents a low-energy mode (e1) well isolated in energy from the higher order modes. This mode exhibits a calculated quality factor $Q_{e1} \sim 78000$[b] at $\omega = 0.285(a/\lambda)$, with polarization perpendicular to the longitudinal direction of the cavity. The PCM simulation has been carried out by a 3D fully-vectorial FDTD commercial software [109]. As the Q

[b]The accuracy on this value is estimated around 5%.

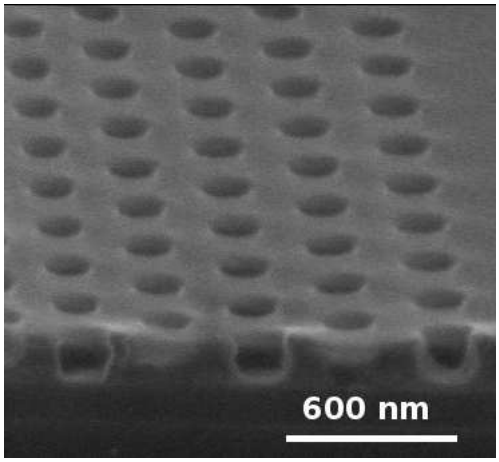

Figure 2.2: SEM image after resist development. Inhomogeneities in the edge are due to the cleaving process of the structure.

increases the modes become more sensitive to the imperfections of fabrication [108]. The experimental determination of the value of the Q constitutes a good test for the fabrication process of the PCMs [110].

2.3 Fabrication

2.3.1 Epitaxial material and mask creation

Epitaxial material and SiO_x deposition

The starting material consists of a 237 nm thick InP layer containing as active layer four InAsP/InP QWs grown by molecular beam epitaxy (MBE). A 1156 nm InGaAs sacrificial layer was grown on the top of an InP substrate.[c] The sample presents a strong luminescence around 1500 nm. On top of the structure a 120 nm layer of SiO_x was deposited at 300 °C by plasma enhanced chemical-vapor deposition

[c]This epitaxial material was provided by Institut des Nanotechnologies de Lyon (INL), Lyon, France.

(PECVD). This is the highest temperature of deposition of our system. The SiO_x density increases as a function of the temperature. It is important to point out that the SiO_x room temperature deposited is slightly porous. In order to ensure the reproducibility of the process, the PECVD machine must be kept at the target deposition temperature around one hour before launching the deposition process due to the long thermic remanence of the deposition plate of the PECVD system. This provides the same substrate temperature among several depositions.

E-beam lithography

The patterning of the PC structure was done by e-beam lithography on a LEO 1455 SEM with a laser interferometric stage (LIS). The sample was spin-coated at 4900 rpms during 30 s setting the acceleration parameter at 5[d] with polymethylmethacrylate anisole 4% (PMMA-A4) resist.[e] The resist was baked in a conventional oven at 170 °C for 70 mins. After baking the resist thickness was measured with an optical thickness meter. The typical value measured is 200 nm and no smaller thicknesses have been obtained in these conditions. Nevertheless, higher values up to 220 nm have been measured. These variations in the resist thickness, that are probably related to the size of the sample, do not yield a change in the quality of the final result. The thickness of the resist is optimum in order to obtain the necessary resolution for the shape of the holes using an acceleration voltage of 26 kV. On the other hand, this thickness is enough to withstand the RIBE etching necessary for transferring the pattern to the hard SiO_x mask. The developing process was performed submerging the sample for 45 s in solution isopropanol/methyl isobutyl ketone (1 : 3), and for 45 s in isopropanol. After this process the sample was post-baked in a hot plate for 1 min at 100 °C in order to increase the hardness and the holes homogeneity. The reduction of imperfections produced in the e-beam lithography process by means of the resist post-baking has been shown in ZEP520A resist [111] for silicon microdisks fabrication.

In order to correct for the proximity effect we used the proximity correction module

[d] The spin coating machine at the IMM do not measure angular accelerations.
[e] Resit characteristics: *http : //www.microchem.com/products/pdf/PMMA_Data_Sheet.pdf*

NanoPECS integrated in the Raith ELPHY *Plus* lithography system. The correction of the proximity effect is a key point in the fabrication of PC structures. If this correction is not applied a strong inhomogeneity in the radii of the holes is observed that produces an important degradation of the optical properties of the structure [112, 113]. The proximity effect is mainly due to the electrons backscattering, forward scattering, secondary electrons and the finite size of the exposure beam [114]. The basic element for solving the proximity effect is the point exposure distribution (also referred as proximity function) that describes the dose cross distribution [114]. The proximity function has the same shape as electrons absorbed energy distribution in the material with respect to the lateral distances [115]. Typically, the proximity correction functions used are a double gaussian, a double gaussian plus an exponential or simply a gaussian plus an exponential term [114, 116, 117]. We have used the double gaussian with an exponential term as proximity correction function. It must be noted that the exponential term has been used with good results on dense patterns with involved dimensions $\sim$ 0.1-0.25 μm [114]. The proximity function used is:

$$f(r) = \frac{1}{\pi(1+\eta+\nu)}\{\frac{1}{\alpha^2}exp(-r^2/\alpha^2) + \frac{\eta}{\beta^2}exp(-r^2/\beta^2) + \frac{\nu}{2\gamma^2}exp(-r/\gamma)\}. \quad (2.1)$$

where α represents the range of the forward scattering, β represents the range of the backward scattering, and η is the backscattering coefficient (the ratio between the integrated proximity effect function of the backscattered electron and that of the forward scattered electrons). The third term is introduced in order to improve the fitting of the double gaussian term [114] and is an arbitrary term. Finally, ν and γ does not have physical interpretation. For the determination of the proximity correction function parameters there are several methods described in [114], [116], see references therein too. In our case, the determination of the optimal parameters values has been done empirically. We have used several values from the literature[f] for III-V semiconductors (InP and GaAs) and the procedure that follows:

1.- The function parameters have been slightly modified.

[f]References cited in this section.

2.- The pattern with the corrected doses, together with the previously selected parameters have been determined using the NanoPECS module.

3.- The pattern was SEM exposed for several doses at a beam current of $\sim$ 37 pA (our working current), from lower to higher doses.

4.- The dry etching process (to be described in the following sections) is carried out.

5.- Finally, the best parameters for the proximity correction function are determined from the SEM picture after dry etching.[g]

The selected parameters were: $\alpha = 0.025$ μm, $\beta = 1.96$ μm, $\gamma = 0.76$ μm, $\eta = 0.47$ and $\nu = 2.19$. Our (α, ν) values are similar to those found in Ref. [114], whereas (β, γ) are close to those reported in Ref. [118], and η to the values showed in Ref. [116]. Nevertheless, our parameters slightly differ from the ones reported in Ref. [117] for an InP material with PMMA resist. However, it must be noted that their acceleration voltage is different and their sample has not a SiO_x layer. In addition, the exposure current can be different too. In order to compare the parameters selected with a "system" with the same characteristics as ours, we performed Monte Carlo simulations within the NanoPECS module. A gaussian distribution for the e-beam with a FWHM of 25 nm was selected. The obtained parameters were: $\alpha = 0.025$ μm, $\beta = 1.67$ μm, $\gamma = 0.55$ μm, $\eta = 0.53$ and $\nu = 1.63$. These parameters can be considered in general in agreement with the empirically determined ones. Fig. 2.2 shows a SEM image of the PMMA-A4 after the e-beam exposure and development where a $\sim$2 nm thick layer of gold was deposited on the sample for a clearer SEM picture.[h]

RIBE etching of the SiO_x mask

The e-beam resist pattern was transferred to the SiO_x hard mask by dry etching in an ECR-RIBE machine (Plasma Technics ECR-160). For more details about the

[g] The proximity effect is observed more clearly for structures under- and over- exposed than in the structure close to the target parameters.

[h] In the this chapter we refer to this deposition as *"2 nm metal deposition"*.

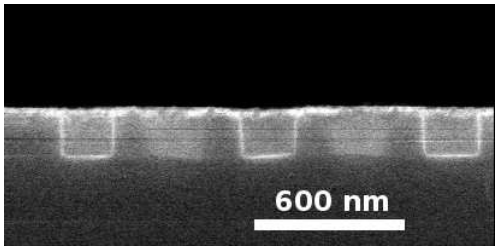

Figure 2.3: SEM cross section image after the RIBE etching where the remanent of resist was eliminated.

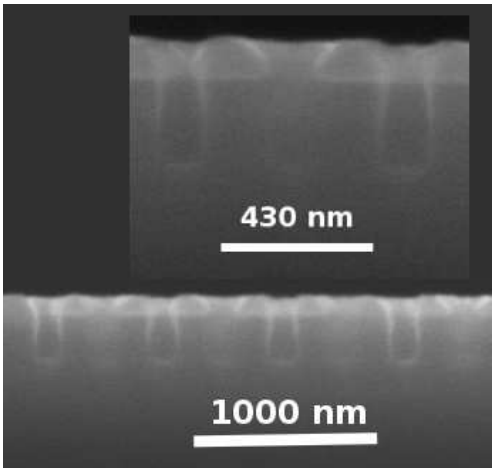

Figure 2.4: SEM cross section image after the RIE etching. The inset shows a detail.

system see Ref. [119]. The RIBE etching has, among other features, the advantage of independently control of the physical and chemical components of the etching.

The chamber pressure was kept at a base pressure of $\sim 2 \times 10^{-7}$ Torr. Flows of 5.6 SCCM (SCCM denotes cubic centimeter per minute at standard conditions for temperature and pressure (STP)) of CHF_3 and 4 SCCM of N_2 was injected, yielding a chamber pressure of $\sim 3 \times 10^{-4}$ Torr. The addition of N_2 was used in order to produce stable ECR discharges [119]. A beam voltage of 250 V and an accelerating voltage of -450 V were selected for the etching process. The sample steel plate was not refrigerated and was rotating during all the etch process. Fig. 2.3 shows a cross

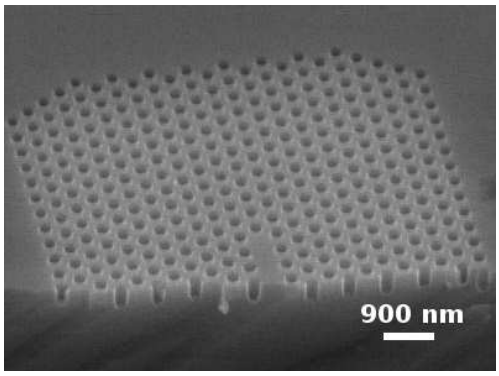

Figure 2.5: SEM cross section image after the RIE etching where the SiO_x has been removed.

section SEM image of the structure after the RIBE etching where a 2 nm metal deposition was done on the sample to avoid the SiO_x charging during the SEM inspection. The remanent of the PMMA-A4 resist was eliminated submerging the sample in hot acetone ($T \simeq 50$ °C) during 15 min and oxygen plasma at 200 W of coil power, 100 V of DC bias, and 450 mTorr of pressure during 10 min. Smooth[i] and straight sidewalls are obtained. The obtention of a hard mask with enough thickness, smooth and with no angled sidewalls is critical in this process in order to increase the Q. If the mask does not present such properties the imperfections can be translated to the semiconductor material in the following etch process [120].

2.3.2 Hard mask transfer and membrane realization

RIE etching of the InP

In order to transfer the SiO_x pattern to the InP semiconductor material RIE etching was used on an Oxford ICP-RIE Plasmalab 80 machine. We selected CH_4/H_2 as the etching gases, which provides a non corrosive and low toxicity gas mixture. This mixture has been widely used for etching InP material in RIE [121] due to its good properties in terms of anisotropy, surface morphology, smooth sidewalls and

[i] According to the SEM pictures.

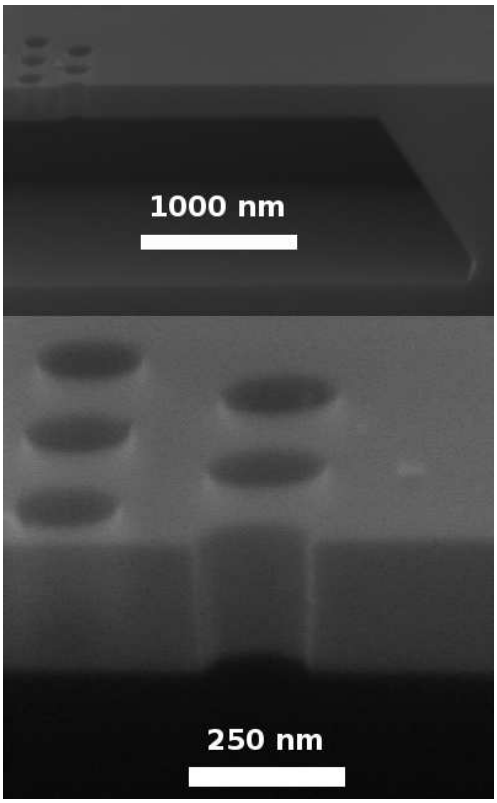

Figure 2.6: Top: SEM cross section image after the membrane fabrication. Bottom: Detail of one of the fabricated holes.

high quality of the InP surface [122]. The main disadvantage of this mixture is the carbon-based polymer formation during the etching process. This affects the etching process in two ways: the first one is the deposition of the polymer in the walls of the chamber that plays an important role in the etching process and can affect the reproducibility [119]. The second way is the deposition of polymer on the surfaces of the sample that can be critical in structures with high aspect ratio like PCs. To avoid this, polymer removal was proposed by O_2 cycling in $CH_4/H_2/Ar$ gas mixtures [123] and was carried out in PCs fabrication [124]. Our process consists on several steps of one minute of CH_4/H_2 etching and 15 s of O_2 for removal of the polymer. Between both etchings a 100 SCCM flux of N_2 (with the valve that regulates the pressure

at the maximum of aperture) was injected during 1 min in the chamber in order to remove (to sweep away) any possible gas remanent in the chamber from the previous plasma etchings. The optimized parameters for the etching process are: 5 SCCM of CH_4 and 30 SCCM of H_2, pressure of 20 mTorr and power of 300 W, giving a self-bias of 495 V. In order to make the plasma discharge it is necessary a strike pressure of 80 mTorr. The system takes an average time of 12 s to reach this value (then the plasma discharge) and it takes 14 s decreasing the pressure till the 20 mTorr. In both cases the time dependence of the pressure is linear. The parameters of the O_2 plasma are: flux of 50 SCCM, pressure 20 mTorr and power 200 W, yielding a self-bias of 460 V. Before the etching a preconditioning of 150 s is performed in the same conditions as the methane etching step. This step is carried out in order to obtain the same initial conditions and to ensure the reproducibility of the process. It is also performed to mask the possible rest (remanent) of different previous etchings carried out in the RIE chamber. The complete etching process consists of eight CH_4/H_2 steps and one more of O_2 in order to remove the last polymer deposition. Fig. 2.4 shows a SEM cross section image of the structure after the RIE etching process, where the remanent of SiO_x can be observed on the top of the InP semiconductor material. A 2 nm metal deposition was done as in the previous SiO_x pictures. The SiO_x etching rate is $r_{SiO_x} \simeq 3$ nm/min, measured in the area out of the holes for several samples by means of an optical thickness meter. The InP etching rate at the holes is $r_{InP(holes)} \simeq 47$ nm/min.[j] In order to simplify the obtention of the InP etching rate, these values have been obtained in samples without InGaAs sacrificial layer. The InGaAs etch rate is expected to be smaller than the InP etch rate [121]. Figure 2.5 shows an image of one of the samples used to determine the InP etch ratio. We can define a selectivity $S = r_{SiO_x}/r_{InP(holes)} = 1/15$ as the ratio between the etching rates. This value reveals this process as a promising procedure for deep etching of InP materials for low index contrast photonic crystal circuits [125].

[j]The etch rate is slightly underestimated, since the real etching time is 48 s instead 1 min. Nevertheless, this does not affect the selectivity value.

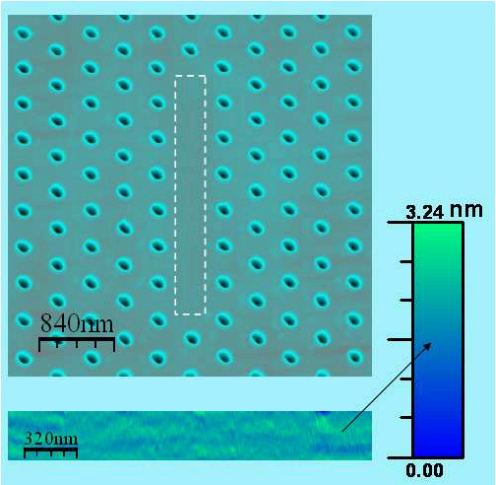

Figure 2.7: Up: AFM image of one PCM fabricated. The lattice parameter is ~ 400 nm. Dashed lines marks the area detailed in the bottom figure. Bottom: Detail of the center structure. The RMS value is 0.22 nm.

Membrane release

The remanent SiO_x after the RIE etching is removed in hydrofluoric acid water diluted $HF(1) : H_2O(5)$ submerging the sample during 90 s. To eliminate the InGaAs sacrificial layer a $HF(1) : H_2O_2(1) : H_2O(20)$ solution was used [126] during 5 min. The mixture was done according to the procedure that follows: first the water, second the H_2O_2, and finally the HF. It has been observed that slight variations of the HF and H_2O_2 concentrations on the solution do no affect significantly the etching speed. Figure 2.6 shows a cross section SEM image of the membrane after wet etching: smooth and straight sidewalls are obtained. Figure 2.7 shows an atomic force microscope (AFM) image of a PCM after the membrane is released.[k] A surface roughness in the cavity area of 0.22 nm of RMS has been measured, showing that our process does not change the sample surface morphology (this is the typical value of the "*epiready*" substrates), which makes the optical losses due to this effect negligible [103].

[k] AFM picture courtesy of Dr. J. Martín-Sánchez.

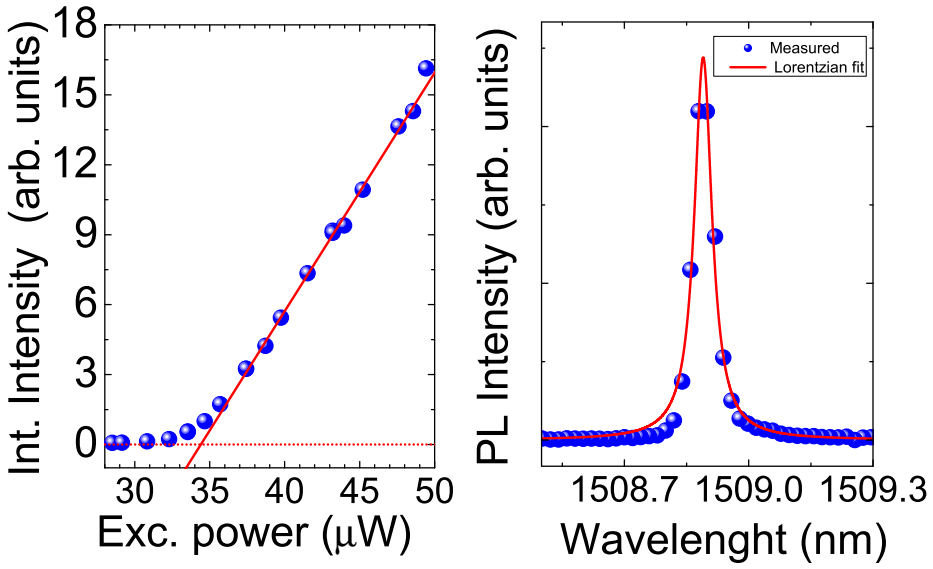

Figure 2.8: Integrated PL spectra intensity as a function of the pump power (left). The continuous line corresponds to the linear fitting. Spectrum of the emission measured just below the threshold (right). The blue dots represent the experimental measurements. The continuous line corresponds to the Lorentzian function fitting ($Q = 30000$).

2.4 Optical characterization

In order to validate our fabrication process the best procedure is to perform an optical measurement of the Q of the fabricated structures. The characterization was performed by μ-PL spectroscopy at room temperature. The structures were optically pumped with a 785 nm pulsed laser diode. The pulsed frequency was 1 MHz and the duty cycle 2.5 %. An objective lens (0.5 NA) was used to focus the excitation spot over the PCM. The emitted light was collected through the same objective and focused into an optical fiber connected either to an optical spectrum

analyzer or dispersed by a 0.85 m focal length double spectrometer with a cooled InGaAs photodiode array as detector. It must be noted that the emission is very sensitive to the excitation conditions. Fig 2.8 shows the integrated PL spectra intensity as a function of the average incident pump power and one of the spectra measured just below the threshold. The value of the Q measured is 30000, which is obtained from the estimated transparency pump power using the procedure from Ref. [127]. This value is in agreement with other values reported in the literature for InP microcavities with active material [128]. The lasing threshold value was around $\sim$ 34 μW, which can be further optimized by fine tuning of the optical pumping experimental setup.

2.5 Summary

We have fabricated high Q PCMs on InP containing InAsP/InP QWs as active material. Electron-beam lithography combined with dry etching has been used for the nanopatterning of the semiconductor material. A process combining RIBE with a CHF_3/N_2 gas mixture for etching SiO_x hard mask and RIE with CH_4/H_2 and O_2 cycling was used for etching the semiconductor material. An InP etch rate on holes $\simeq$ 47 nm/min was obtained. L7-kind PCMs with Q of the fundamental mode up to 30000 have been obtained. These results open the possibility to study the emission properties of InAs quantum wires and quantum dots in high Q PCMs.

Chapter 3

Effect of the implementation of a Bragg reflector in the photonic band structure of the Suzuki-phase photonic crystal lattice

In this chapter it is investigated the change of the photonic band structure of the Suzuki-phase photonic crystal lattice when the horizontal mirror symmetry is broken by an underlying Bragg reflector. The structure consists of an InP photonic crystal slab including four InAsP quantum wells, a SiO_2 bonding layer, and a bottom high index contrast Si/SiO_2 Bragg mirror deposited on a Si wafer. Angle- and polarization-resolved photoluminescence spectroscopy has been used for measuring the photonic band structure and for investigating the coupling to a polarized plane wave in the far field. A drastic change in the k-space photonic dispersion between the structure with and without Bragg reflector is measured. An important enhancement on the photoluminescence emission up to seven times has been obtained for a nearly flat photonic band, which is characteristic of the Suzuki-phase lattice.

3.1 Motivation

Since the beginning of the research in photonic crystal (PC) structures at the Instituto de Microelectrónica de Madrid (IMM) several kinds of structures have been developed with the main intention of improving the optical confinement properties of the PCs. First, we studied the spontaneous emission in photonic crystal microcavities (PCM) and how the emission of the modes varies (wavelength emission change) with the slab thickness [129]. In that case, a triangular lattice of holes was patterned in the semiconductor material. Some holes were eliminated in order to create hexagonal shape microcavities $H1$, $H3$ and $H5$ [130]. The slab thickness was decreased by means of reactive ion beam etching (RIBE) and the change of emission of the modes was characterized by microphotoluminescence. Second, the laser emission in ring-like resonators (created inside of a triangular lattice of holes) was studied and how the number of electromagnetic modes inside the photonic band gap can be reduced by means of H1 PCMs inserted inside the ring-like (a hexagonal PC waveguide) structure. A strong-modal supression for one particular disposition of the PCMs [131, 132] was obtained. The third kind of structure studied was the Suzuki-phase (SP) lattice [51]. There, instead of studying intentionally created defects in the structure (PCMs), and since the first photonic band gap is mainly above the light line [51] making the design of PCMs with high quality factor (Q) not straightforward, we studied the photonic band structure by angle revolved photoluminescence (ARP). Photonic band structure showed several features [133], being a flat photonic band along the direction ($\Gamma X1$) the main one. Such band yields a strong lateral confinement along the mentioned direction. The natural way to improve the electromagnetic confinement of this photonic band is to combine the 2D PC slab with a bottom Bragg reflector.[a] This work had to be done in parallel with the development of the fabrication process of PCMs in GaAs slabs [113].

[a]The semiconductor material for this study was provided by Institut des Nanotechnologies de Lyon, INL-Lyon, (France).

3.2 Introduction

The combination of one-dimensional (1D) and two-dimensional (2D) PCs with a Bragg reflector has been demonstrated to be a powerful tool for engineering the light confinement properties [40, 134], giving place to the so-called 2.5D micro-nano-photonics [78]. Some devices combining a 2D-PC and a one-dimensional Bragg reflector have been already fabricated [39, 80, 135, 136]. The combination of a Bragg reflector with an active 2D-PC slab can enhance the Q of the resonant mode [39, 137]. In this way, we want to study the actual effect of the Bragg mirror on the photonic bands. For this purpose, we have fabricated the Suzuki-phase (SP) 2D-PC [51] in samples with and without bottom Bragg reflectors. The Suzuki lattice belongs to a set of 2D structures, like the graphite, triangular-graphite, and the Archimedean lattices [138, 139, 140], which possess a basis consisting on several rods/holes per unit cell. All these lattices seem to support several low-dispersive photonic bands, similar to coupled cavity arrays [141]. The SP lattice presents four features that are very useful for our study:

1. It has a complex photonic band structure in two dimensions, which allows to probe several bands in the region of wavelengths of interest (around 1500 nm).

2. The SP pattern presents a flat band along the direction $\Gamma X1$, well isolated from other bands and which shape remains almost unchanged when we calculate the band structure in the "symmetric" and in the "non-symmetric" or full band approach [51]. Fig. 3.1 shows the photonic bands of the SP lattice calculated by guided-mode expansion (gme) [106][b] in the "symmetric" and in the full band approach[c], where the "unchanged" photonic band is observed.

3. The photonic bands have a finite Q (lower than 600), which makes easier to observe the Bragg effect on it.

4. The three previous features take place above the light line [51] which makes possible a study using angled-resolve photoluminescence (ARP).

[b] The simulation has been done by Prof. L.C. Andreani from Università degli Studi di Pavia, Italy.

[c] The polarization criteria of the figure is explained in Sec.3.3.2

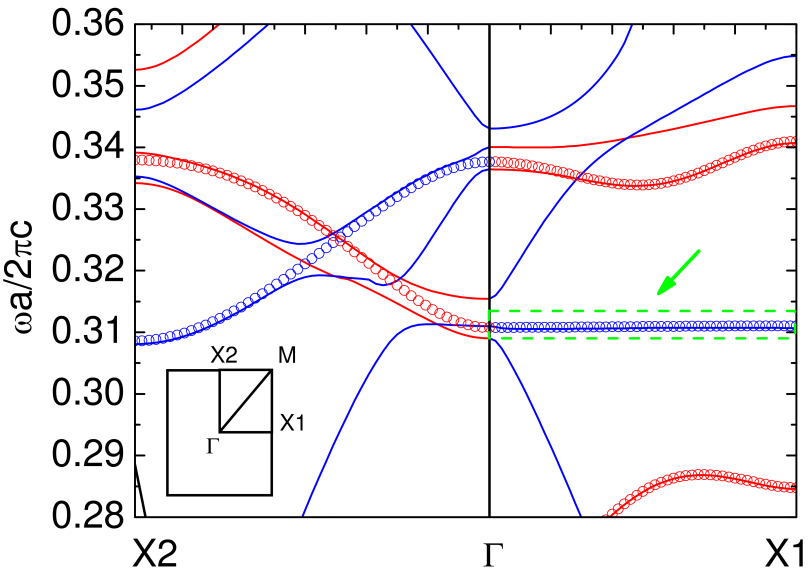

Figure 3.1: Photonic band structure of the Suzuki-phase lattice. Blue color correspond to the bands with $\sigma_{kz} = +1$ polarization. Red color for bands with $\sigma_{kz} = -1$ polarized. Doted lines show the bands calculated by gme in the "symmetric" approximation with the parameters $d/a = 0.514$, $r/a = 0.33$, and $\epsilon = 1.55/10.1/1.55$. Only $\sigma_{xy} = +1$ or TE-like modes are shown. Continuous lines shows the full band structure calculated by gme with the parameters $d/a = 0.514$, $r/a = 0.33$, $\epsilon = 1.0/10.1/2.1$. Green color highlights the flat band.

The fabricated structures were characterized by an extended ARP method that includes measurement of polarization, called polarization-resolved angle-resolved photoluminescense (PR-ARP) in order to obtain the photonic band structure and its polarization. A drastic difference in the photonic band structure was measured between the samples with and without Bragg mirror. Moreover, a remarkable enhancement up to seven times of the intensity of the photoluminescense (PL) emission has been measured for one particular photonic band.

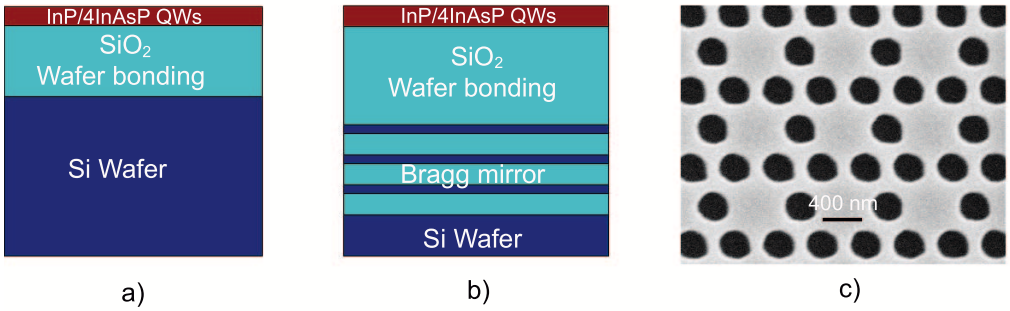

Figure 3.2: Layout of the transversal section of the fabricated structures. a) InP/InAsP layer epitaxy bonded to a Si wafer through a SiO_2 layer. b) InP/InAsP layer epitaxy bonded to Bragg reflector on top of the Si wafer through a SiO_2 layer. c) Scanning electron microscopy (SEM) image of the fabricated structure with Bragg mirror.

3.3 Fabrication and Optical characterization

3.3.1 Fabrication

The SP PC lattice was fabricated in two kinds of semiconductor slabs. The first one (Fig. 3.2 a)) consists of an InP slab incorporating four $In_{0.65}As_{0.35}P/InP$ quantum wells grown on an InP substrate by molecular beam epitaxy. The layer has a thickness $d = 237$ nm. The epitaxy is transferred onto a silicon-on-silica substrate by wafer bonding (SiO_2 thickness $=0.9\pm0.1$ μm) [142]. The second one (Fig. 3.2 b)) consists of an InP slab containing the same quantum well structure as before. The thickness is $d = 250$ nm. A three pair quarter-wavelength Si/SiO_2 is deposited in the top of a Si wafer by low pressure chemical vapor deposition. The thickness of the Si and SiO_2 $\lambda/4$ layers are 110 nm and 255 nm, respectively. A reflectance spectrum of the Bragg mirror is shown in Ref. [39]. The epitaxial structure is transferred on the top of the Bragg mirror by SiO_2 wafer bonding. The thickness of the SiO_2 bonding layer is $d_{SiO_2} = 790$ nm [39]. Both structures present a strong PL around 1.5 μm.

A 90 nm-thick SiO_2 layer was deposited by plasma assisted sputtering on top of

both samples as mask layer for the etching process. Electron-beam lithography and reactive ion-etching were used for the patterning.[d] For the structure without Bragg mirror the lattice parameter a is 455 nm ($d/a = 0.514$) whereas for the structure with Bragg mirror $a = 484$ nm ($d/a = 0.516$). It is important to have the same d/a value for both samples because the photonic bands change with the thickness of the slab [143, 106, 53], which may prevent easy comparison of the emission properties between structures. Both structures preserve the same r/a ratio (r/a=0.33). The size of the fabricated structures was 25 μm × 25 μm for the sample without Bragg and 30 μm × 30 μm for the sample with Bragg.

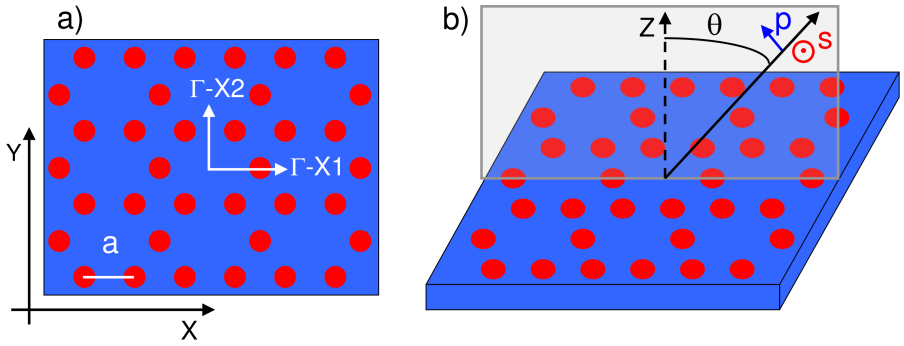

Figure 3.3: a) Suzuki lattice with the axes in the XY plane. b) Schematic drawing of the experimental geometry, for the specific case of Γ-$X1$ orientation, with the polarization directions of the electric field with respect to the plane of observation. Under specular reflection $\hat{\sigma}_{kz}$ with respect to a vertical mirror plane including the wavevector, transverse magnetic or p-modes are even ($\sigma_{kz} = +1$) while transverse electric or s-modes are odd ($\sigma_{kz} = -1$).

3.3.2 Optical characterization

PR-ARP spectroscopy was used for optical characterization.[e] The samples were optically pumped with a 635 nm laser diode through a 10× (NA=0.26) objective

[d] At this time the InP RIE etching was not developed at IMM. The dry etching process was performed at Institut des Nanotechnologies de Lyon, INL-Lyon, (France).

[e] The measurements were performed by Dr. M. Galli and Dr. J. F. Galisteo-López at Università degli Studi di Pavia, Italy.

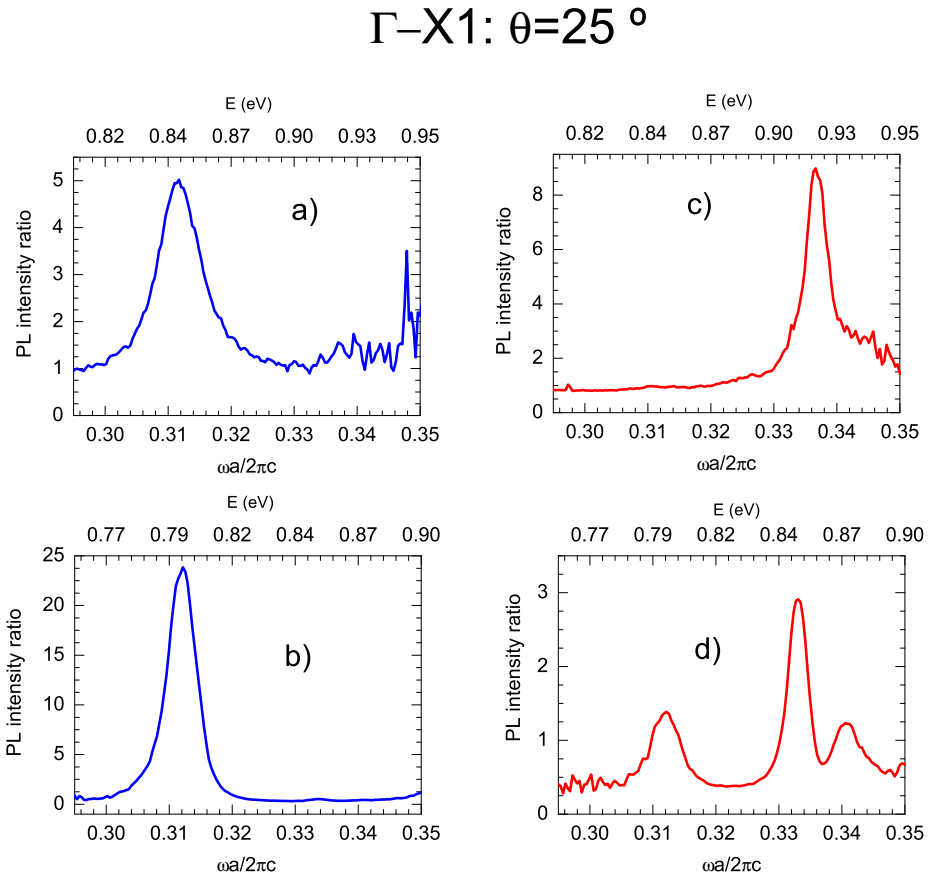

Figure 3.4: Normalized PL spectra along the direction Γ-$X1$, for the sample without Braggs a,c) and for the sample with Braggs b,d) at angle $\theta = 25°$. Blue line for even ($\sigma_{kz} = +1$) or p-polarization, red line for odd ($\sigma_{kz} = -1$) or s-polarization with respect to a vertical mirror plane.

placed at an angle of 45° with respect to normal incidence. The angle-resolved PL emission was collected by a fiber coupled to a Fourier-transform spectrometer (Bruker IFS66/s). An InGaAs p-i-n photodiode was used as detector. The PL at room temperature can be collected with an angular resolution of ±1°. The PL was collected at different angles from 0° to 30° at intervals of 5° along the directions $\Gamma - X1$ and $\Gamma - X2$ with a linear polarizer in the collection arm. A diagram of the experimental set-up is shown in Ref. [133]. The measured PL spectra were used to determine the photonic band dispersion through conservation of the wavevector parallel to the sample surface [144, 145, 146, 58, 147], and their polarization.

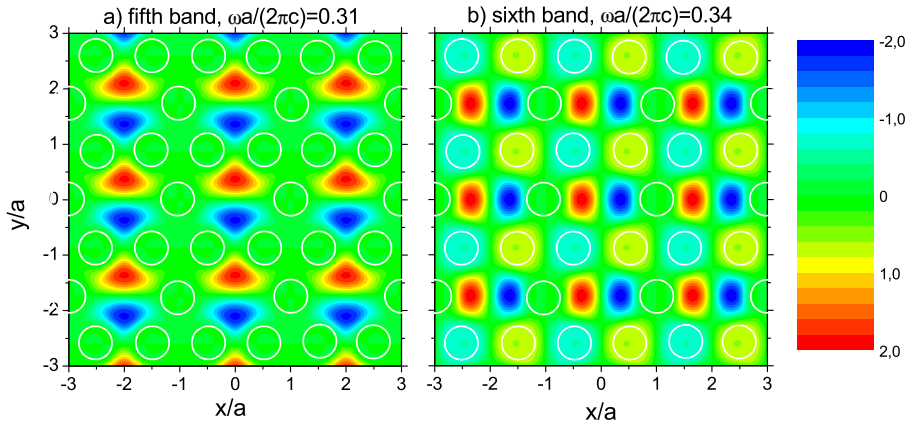

Figure 3.5: Real part of magnetic field component H_z at the Γ point for the photonic modes corresponding to the resonant structures in Fig. 3 a) at $\omega a/(2\pi c) = 0.31$ (fifth band) and in Fig. 3 c) at $\omega a/(2\pi c) = 0.34$ (sixth band).

The axes of polarization and the experimental geometry are defined according to Fig. 3.3.[f] For incidence in a plane along the Γ-X1 direction, since the XZ plane is a mirror plane of the Suzuki-phase lattice, the electromagnetic field can be even or odd under the mirror reflection operation $\hat{\sigma}_{kz} = \hat{\sigma}_{xz}$: the former states are denoted as $\sigma_{kz} = +1$, while the latter are denoted as $\sigma_{kz} = -1$. For incidence in a plane along the Γ-X2 direction, since the YZ plane is again a mirror plane of the Suzuki lattice,

[f]Sketch courtesy of Prof. L. C. Andreani, Università degli Studi di Pavia, Italy.

the eigenstates of the electromagnetic field can be even ($\sigma_{kz} = +1$) or odd ($\sigma_{kz} = -1$) under the mirror reflection operation $\hat{\sigma}_{kz} = \hat{\sigma}_{yz}$. We notice that $\sigma_{kz} = +1$ states are coupled to transverse-magnetic or p-polarized light with respect to the observation plane shown in Fig. 3.3 b), while $\sigma_{kz} = -1$ states are coupled to transverse electric or s-polarized light [145]: these denominations, however, relate only to vertical mirror symmetry $\hat{\sigma}_{kz}$ and have nothing to do with specular reflection $\hat{\sigma}_{xy}$ with respect to the XY plane, which is not a symmetry operation of the structure with Bragg.

Four typical normalized PL spectra along the $\Gamma - X1$ direction, for one particular angle ($\theta = 25°$), for the samples with and without Bragg reflector, are shown in Figure 3.4. The PL spectra were normalized dividing the PL intensity from the patterned area over the PL intensity of a close unpatterned area. Similar spectra were obtained for the rest of the angles of measurement. A clear change in the intensity (Fig. 3.4 a,b)) and number of peaks (Fig. 3.4 c,d)) for each polarization ($\sigma_{kz} = +1$ (p), $\sigma_{kz} = -1$ (s) respectively) is observed between the samples with and without Bragg reflector. For each angle (θ), the observed peaks were fitted to gaussian functions. The center of the fit function was extracted and plotted versus the parallel component of the wave vector ($k_{||}$). The values of the $k_{||}$ are obtained by the relation 3.1, where ω is the radiation angular frequency, θ is the angle of measurement, E is the radiation energy measured in eV (the center of the fit), and a is the lattice constant of the PC lattice.

$$k_{||} = \frac{\omega}{c} sin\theta \Longrightarrow k_{||}\frac{a}{\pi} = 1.1613E[eV]a[\mu m]sin\theta \tag{3.1}$$

Figure 3.5 shows the real part of the magnetic field component H_z at the Γ point for the photonic modes corresponding to the resonant structures in Fig. 3.4 a) around $\omega a/(2\pi c) = 0.31$ and in Fig. 3.4 c) around $\omega a/(2\pi c) = 0.337$. These modes correspond to the fifth and the sixth band, respectively, of the sample without Bragg (the horizontal mirror symmetry $\hat{\sigma}_{xy}$ is not broken). Considering that the magnetic field **H** is a pseudo (or axial) vector [50], we notice that the fifth band is even along the $\Gamma - X1$ direction ($\sigma_{xz} = +1$) and odd along the $\Gamma - X2$ direction ($\sigma_{yz} = -1$). Thus, we expect the fifth band to couple to p-polarized light along the $\Gamma - X1$ direction and to s-polarized light along the $\Gamma - X2$ direction. The sixth band, instead, is

odd along the $\Gamma - X1$ direction ($\sigma_{xz} = -1$) and even along the $\Gamma - X2$ direction ($\sigma_{yz} = +1$), thus it couples to s-polarized light along $\Gamma - X1$ and to p-polarized light along $\Gamma - X2$. These results are in agreement with those shown in Fig. 3.4 a,c) and shown that polarization-resolved PL is a powerful tool to identify photonic bands through their symmetry properties.

3.4 Results

The photonic bands and their polarization measured for both samples with and without Bragg reflector are shown in Fig. 3.6. Figure 3.6 a) shows the photonic bands measured for the sample without Bragg and the calculated band structure in the "symmetric" approach [51, 53] where mirror symmetry $\hat{\sigma}_{xy}$ with respect to a horizontal plane through the InP slab is enforced and only the even modes $\sigma_{xy} = +1$ (sometimes called TE-like) are shown. The parameters of the fitting are $a = 455$ nm, $r = 0.33a$ and $d/a = 0.514$. It is remarkable that the fifth band ($\omega = 0.31$ in Γ) and the sixth band ($\omega = 0.34$ in Γ) have well defined polarization (p or s) for all k-vectors. The fifth band has $\sigma_{kz} = +1$ or p-polarization along the direction $\Gamma - X1$ and $\sigma_{kz} = -1$ or s-polarization along $\Gamma - X2$. The sixth band shows the complementary behavior, i.e, it shows s-polarization along the $\Gamma - X1$ direction and p-polarization along $\Gamma - X2$. This is in good agreement with the expected field patterns calculated by guided-mode expansion for several k-vectors along both directions $\Gamma - X1$ and $\Gamma - X2$, as exemplified in Fig. 3.5 at the Γ point, and is also analogous to previous results found in reflectance spectra of macroporous silicon [145]. The bands are dipole-active (i.e., coupled to polarized light in the far field) with the following orientation: For the fifth band the axis of the dipole is parallel to the $\Gamma - X1$ direction. For the sixth band, the axis of the dipole is parallel to the $\Gamma - X2$ direction. The same measurements were performed in samples with Bragg reflector. Figure 3.6 b) shows the photonic bands measured for the sample with the Bragg reflector and the calculated full band structure [51, 53]. The parameters of the fitting are $a = 484$ nm, $r = 0.33a$ and $d/a = 0.514$. In this case a drastic change in the photonic band structure is observed with respect to the sample without Bragg mirror. The experimental data are best fitted by the full band structure, showing

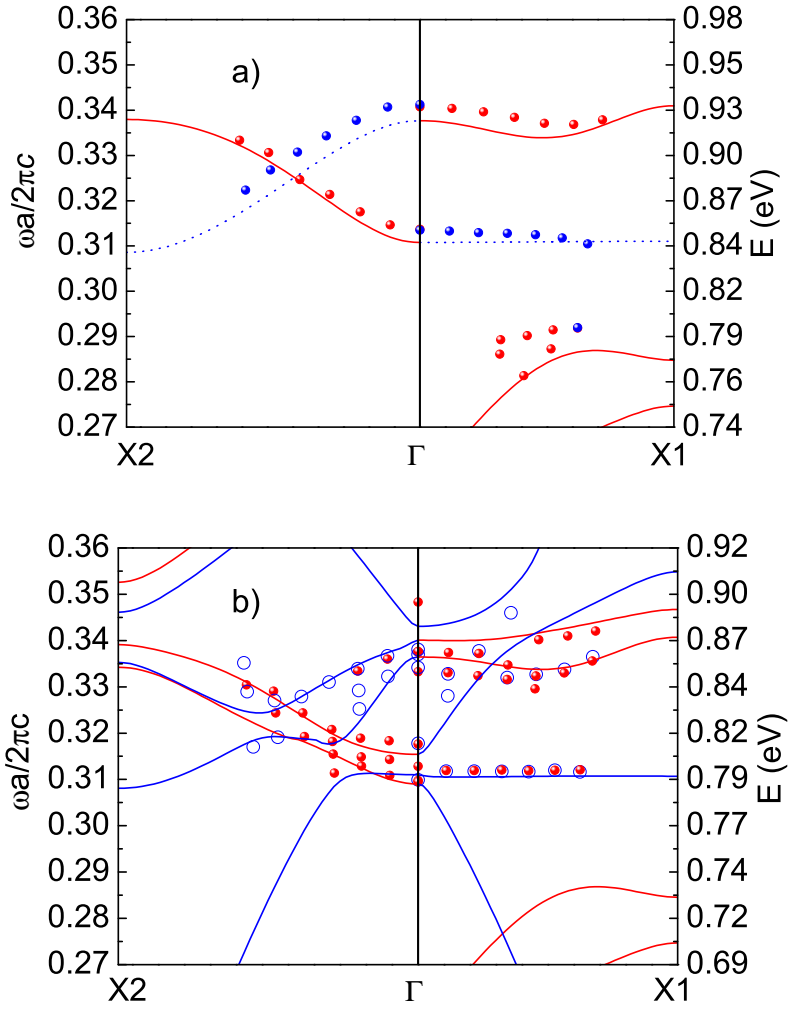

Figure 3.6: Photonic band structure of the Suzuki-phase lattice. Blue color for bands with $\sigma_{kz} = +1$ polarization. Red color for bands mainly $\sigma_{kz} = -1$ polarized. a) Sample without Braggs: Solid lines show the bands calculated by guided-mode expansion in the "symmetric" approximation with the parameters $d/a = 0.514$ and $r/a = 0.33$. Only $\sigma_{xy} = +1$ or TE-like modes are shown. Circles: measured points. b) Sample with Bragg reflector: Solid lines show the full band structure calculated by guided-mode expansion with the parameters $d/a = 0.514$ and $r/a = 0.33$. Filled points for $\sigma_{kz} = -1$ polarization. Blue open circles for $\sigma_{kz} = +1$ polarization.

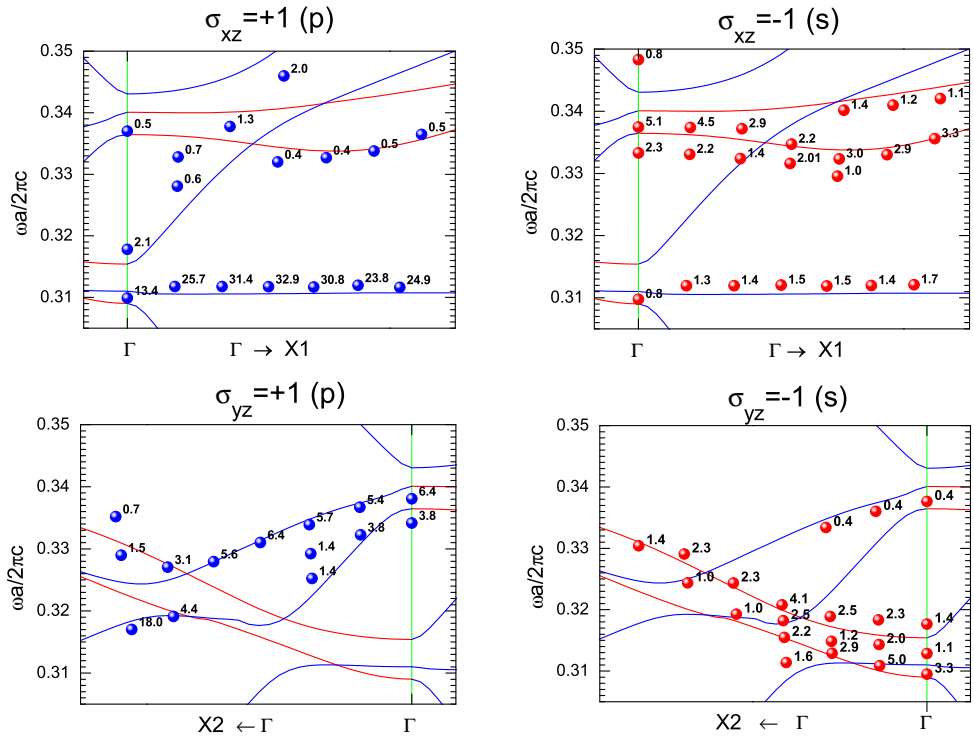

Figure 3.7: Polarization resolved photonic band structure measured for the sample with Bragg mirror. Point label indicates the normalized intensity of emission. Solid curves are calculated with guided-mode expansion: blue bands for bands with $\sigma_{kz} = +1$ or p-polarization, red color for bands with $\sigma_{kz} = -1$ or s-polarization. Arrow indicates the direction of the k-vector. Labels above the graphs indicate the direction of the axis of the polarizer in relation to the axes defined in Fig. 3.3.

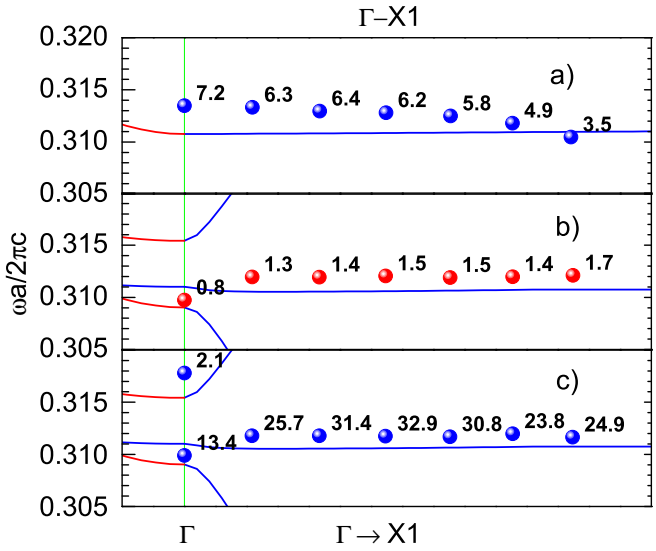

Figure 3.8: Fifth band along the direction $\Gamma - X1$. The numeric labels indicate the normalized intensity. (a) Sample without Bragg: Blue color for bands with $\sigma_{kz} = +1$ or p-polarization. Red color for bands mainly $\sigma_{kz} = -1$ or s-polarization. Blue dots for measured points detecting p-polarized light. b) Sample with Bragg: $\sigma_{kz} = -1$ or s-polarization. Red dots for experimental points detecting s-polarized light. c) Sample with Bragg: $\sigma_{kz} = +1$ or p-polarization. Blue dots for measured points detecting p-polarized light.

that more photonic bands arise in the sample with Bragg mirror. Those bands are due to the breaking of the horizontal mirror symmetry $\hat{\sigma}_{xy}$ of the structure caused by the introduction of the Bragg mirror, which couples TE-like to TM-like modes of the structure without Bragg.

Figure 3.7 shows the normalized intensities measured for the $\Gamma - X1$ and $\Gamma - X2$ directions of the sample with the Bragg mirror. The data show that the photonic bands that should correspond to "TM-like" modes (electric field along z) can be measured, despite the emission of the quantum wells is mainly "TE-like" polarized (electric field in XY plane). This is naturally explained by the breaking of horizontal mirror symmetry $\hat{\sigma}_{xy}$ in the sample with Bragg. On the other hand, vertical mirror

symmetry $\hat{\sigma}_{kz}$ along the $\Gamma - X1$ and $\Gamma - X2$ orientation is preserved even in the sample with Bragg and pure $\sigma_{kz} = +1$ (p) or $\sigma_{kz} = -1$ (s) modes are expected. However, mixing of p/s polarizations is also observed in some bands and for some k-vectors with different intensities for each polarization. Nevertheless, it is important to note that the intensity of emission of the *"unexpected"* polarization component is much more smaller than the *"expected"* one (pure modes). In general the degree of polarization defined as $\rho = |(I_x - I_y)/(I_x + I_y)|$ corresponds to the mixing induced by any symmetry-breaking effect present in the sample. It is remarkable that the fifth band which has p-polarization along the direction $\Gamma - X1$ shows also s-component which was not observed in the sample without Bragg mirror. This band has a degree of polarization (ρ) between 86% and 91%. The polarization mixing effect is attributed to the presence of disorder (variation of hole size, position, microroughness of hole sidewalls, mainly) which breaks mirror symmetry and whose effect may be enhanced in the sample with Bragg.

Figure 3.8 shows the fifth band for both samples and the calculated photonic band structure. According to the calculations, the fifth band is nearly flat along the $\Gamma - X1$ direction, well isolated in frequency and remains almost unchanged in the "symmetric" and full band approach. This makes the fifth band very suitable for the comparison of the intensity of emission between both samples with and without Bragg mirror. For this band the Qs are slightly higher (below two times) for the sample with Bragg mirror. The intensity of the emission for p-polarization is between 4 and 7 times higher for the sample with Bragg mirror in the whole wavevector (corresponding to angular) range, except for the Γ point, where the enhancement is 1.9. The enhancement of PL signal towards the vertical direction arises from multiple reflections by the Bragg mirrors in the SiO_2 wafer bonding layer, as previously analyzed in Ref. [39]. Notice that even at the X1 point, the internal angle in the SiO_2 layer is calculated to be around 20 degrees, which is well within the angular acceptance of a Si/SiO_2 Bragg reflector. This results in an almost k-independent enhancement.

3.5 Summary

We have fabricated and measured the SP lattice on two kinds of InP semiconductor slabs with InAsP/InP quantum wells as active layer with and without an underlying Bragg mirror. PR-ARP spectroscopy was used for the optical characterization. For the structure without Bragg reflector the experimental data are well fit by a "symmetric" calculation. For the sample with Bragg mirror are best fit by a full band calculation (i.e., TE-like and TM-like modes are coupled). A mixing of p/s polarizations defined with respect to a vertical mirror plane is observed for the structure with Bragg, whereas the polarization is well defined for the non-Bragg sample. An enhancement on the photoluminescence emission up to seven times has been obtained for a flat photonic band along the $\Gamma - X1$ direction, which is the main distinctive feature of the Suzuki-phase photonic lattice. For this band, the Qs are slightly higher (below two times) for the sample with Bragg mirror.

Chapter 4

Two-dimensional surface emitting photonic crystal laser with hybrid triangular-graphite structure

In our search of the enhancement of the optical confinement in photonic crystal structures a two-dimensional photonic crystal lattice conformed in a hybrid triangular-graphite configuration was designed for vertical emission. This lattice was created as a periodic perturbation of the triangular lattice, and includes, as limiting cases, two major well-known structures, the triangular and the graphite lattices. The structures have been fabricated in an InP slab, including four InAsP quantum wells as active layer, on the top of a Si substrate SiO_2 wafer bonded. A compact surface-emitting micro laser, optical pumped and operating at 1.5 μm at room temperature was obtained. Laser emission with thresholds around 70 μW and quality factor up to 12000 have been measured. The Bloch mode selected for the emission keeps a high quality factor ($\geq 2 \times 10^5$) around the Γ point for a wide range of in-plane values $k_{||} \leq 0.1(2\pi/a)$ which is related to the peculiar properties of the hybrid lattice.

4.1 Introduction

Since the first photonic crystal (PC) laser [20] several kinds of 2D-slab (PC) lasers have been studied up to now, like microcavity PC lasers [64], ring-like lasers [148, 131], large area PC lasers [149], and recently the so-called 2.5-D microresonators [134]. In microcavity lasers a high quality factor (Q) and a small modal volume are necessary in order to get low threshold emission [22]. In spite of its high efficiency the PC microcavity (PCM) lasers have two "*drawbacks*": first, the low emission power (a few nW) which is low for many practical applications [150] and second, the low directionality of the emission beam pattern [39] which strongly reduces the fraction of emitted photons that can be collected. In order to overcome those problems, large area two-dimensional (2D) PC lasers can be used. These 2D PC slab lasers are based in the low group velocity close to the high symmetry points of the reciprocal lattice [34, 54, 35, 36]. In this way the light-matter interaction is increased and laser operation is reached easier. One part of those band-edge PC lasers uses specific reciprocal points below the light line [34, 54]. In that case the light is confined in the vertical direction by total internal reflection (TIR) and the optical losses are mainly in-plane due to the finite size of the structure. The other part is based in the low dispersive bands close to the Γ point [35, 36]. In that case, if the Bloch modes are weakly coupled to the radiative modes, laser emission can be reached. The emission is very directional around the Γ point favoring the efficient coupling to, for example, an optical fiber [151]. The threshold and Q vary widely among those structures depending on the kind of the PC lattice, its size and the active material used.

In this chapter we demonstrate laser emission at 1.55 μm in a Γ-point PC laser conformed in the hybrid triangular-graphite lattice [152, 139] with low-threshold and a high Q. Specifically, we have used the Γ_3 point of the photonic bands due to its special properties: first, it favours the vertical emission; second, the Bloch mode selected presents a large vertical quality factor $Q_v \geq 2 \times 10^5$, and third, this happens for a wide set of in-plane values $k_{||} \leq 0.1(2\pi/a)$. This high Q for a large set of $k_{||}$ values above the light line is due to that the selected Bloch mode at Γ_3 of the hybrid lattice corresponds also to the maximum of the first K point of the triangular lattice (K_1), which is below the light line. That point becomes weakly

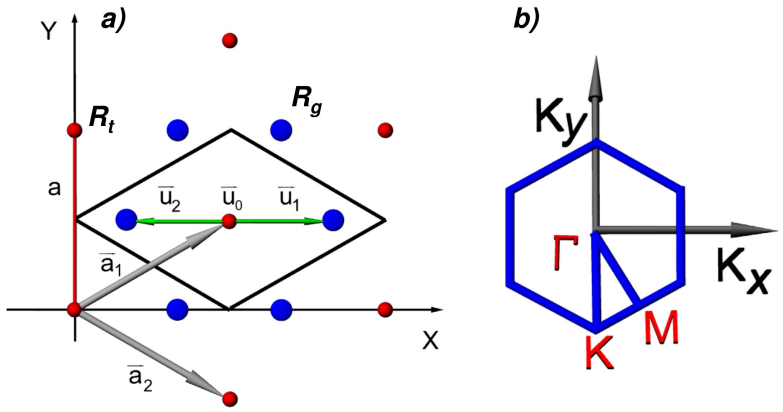

Figure 4.1: a) Schematic representation of the hybrid triangular-graphite lattice. b) High symmetry directions in the k space.

radiative by the small perturbation corresponding to the different radius between the two set of holes of the hybrid lattice, as it will be discussed. Hence, the hybrid structure provides a new physical mechanism for vertical lasing and high Q.

4.2 Two-dimensional photonic crystal description

The hybrid triangular-graphite lattice, also known as the "reduced-symmetry triangular lattice" was proposed for the first time by Ch. M. Anderson *et al.* [152] to increase the absolute band gap in the graphite lattice [138]. However, it was shown by T. Trifonov *et al.* [153] that any modification (square and circular cross sections) of the triangular crystal structure reduces the absolute photonic band gap. In our case the hybrid lattice was created as a periodic perturbation of the triangular lattice (keeping in mind the heterostructure confinement [154] as it will be shown in the next section) where a reduction of the radii of some of the holes of the triangular lattice (with lattice constant $a/\sqrt{3}$) gives birth to a new hybrid structure with two sublattices with triangular and graphite symmetries (that share the same Bravais lattice with underlying lattice constant a, see Fig. 4.1 a)).

The 2D periodic structure used throughout this work is depicted in Fig. 4.1 a). Let R_t be the radius of the cylinders of the triangular sub-lattice and R_g the radius of the cylinders of the graphite sub-lattice, being a the lattice parameter. The hybrid triangular-graphite lattice is generated by means of triangular Bravais lattice with primitive vectors $\overrightarrow{a_1} = a(\sqrt{3}/2, 1/2)$, $\overrightarrow{a_2} = a(\sqrt{3}/2, -1/2)$ and three cylinders by unit cell at positions (with respect to the center of the cell): $\overrightarrow{u_0} = (0,0)$, $\overrightarrow{u_1} = (\overrightarrow{a_1} + \overrightarrow{a_2})/3$ and $\overrightarrow{u_2} = -(\overrightarrow{a_1} + \overrightarrow{a_2})/3$. The radius of the cylinder placed in $\overrightarrow{u_0}$ is R_t (its replication alone would give rise to the triangular lattice) and the radius of the cylinders placed in $\overrightarrow{u_1}$ and $\overrightarrow{u_2}$ is R_g (whose replication alone would give rise to a graphite type lattice). The distance between the center of nearest neighbor cylinders is $a/\sqrt{3}$ and the conditions of non-overlapping cylinders are: $R_t/a \leq 0.5$, $R_g/a \leq 1/2\sqrt{3}$, and $R_g/a + R_t/a \leq 1/\sqrt{3}$. When R_t is equal to R_g the hybrid triangular-graphite lattice becomes a triangular lattice with reduced lattice parameter $a/\sqrt{3}$. Moreover, when R_g is equal to zero the standard triangular lattice is obtained (lattice constant a), and when R_t is equal to zero we recover the usual graphite lattice. The variation of the values of R_t and R_g leads to different configurations for the hybrid triangular-graphite lattice. The reciprocal lattice is given by the primitive vectors: $\overrightarrow{b_1} = \frac{2\pi}{a}(1/\sqrt{3}, 1)$ and $\overrightarrow{b_2} = \frac{2\pi}{a}(1/\sqrt{3}, -1)$, that yields a hexagonal first Brillouin zone with the same symmetry points as the triangular or graphite lattice. The high symmetry points are: $\mathbf{\Gamma} = (0,0)$, $\mathbf{M} = \overrightarrow{b_2}/2$ and $\mathbf{K} = 1/3(-\overrightarrow{b_1} + \overrightarrow{b_2})$, (see Fig. 4.1 b). The hybrid structure (in 2D) is completely described by the radii values R_g/a and R_t/a, and the dielectric constant ϵ. For ϵ, we have chosen the value $\epsilon = 10.1$ since it is the InP dielectric constant at λ=1.55 μm. Using a plane-wave expansion method consisting on the fully vectorial solution of Maxwell's equations with periodic boundary conditions computed by preconditioned conjugate-gradient minimization of the block Rayleigh quotient [155] the dispersion relations are obtained.

Figure 4.2 a) shows the 2D band diagram calculated for radii parameters $R_t/a = 0.12$ and $R_g/a = 0.17$ where several low dispersive bands are observed. This hybrid triangular-graphite lattice belongs to a set of 2D structures, like the Suzuki-phase [51], and the Archimedean [140] lattices, which have a basis made of several rods per unit cell, similar to coupled cavity arrays [141]. All these lattices seem to support several low-dispersive photonic bands. Fig. 4.2 (b-d) shows the Hz-field pat-

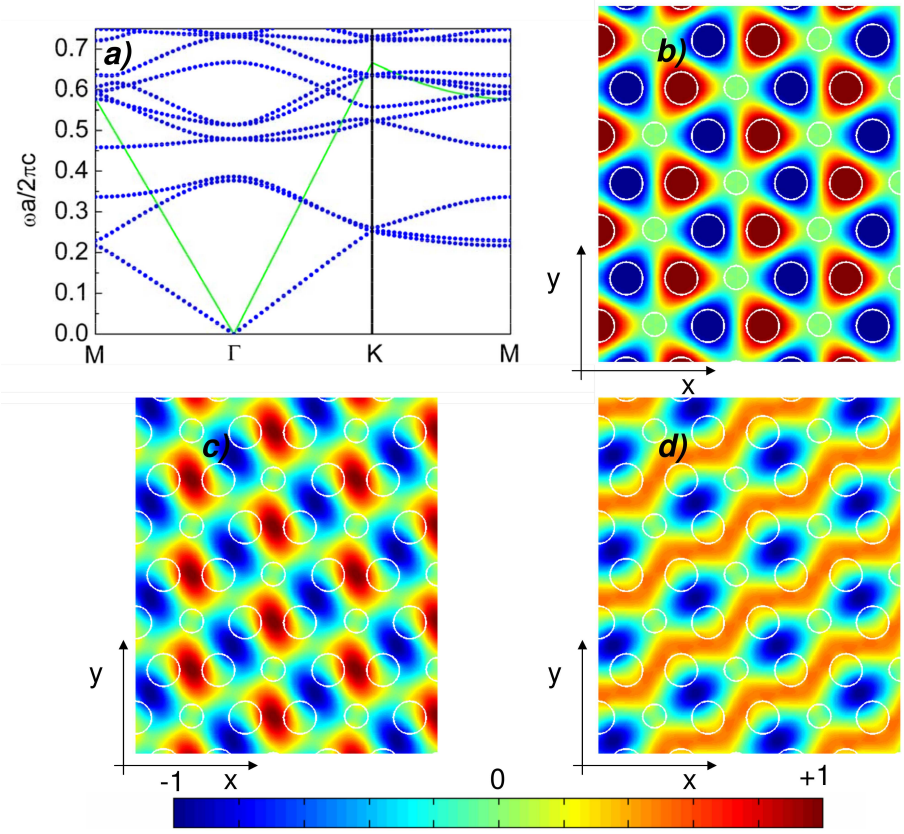

Figure 4.2: a) Photonic band structure (only even modes $\hat{\sigma}_{xy} = +1$ are plotted). b) Normalized imaginary part of the Hz-field profile at the Γ_3 point. c) Normalized real part of the Ex-field profile at the Γ_3 point. d) Normalized real part of the Ey-field profile at the Γ_3 point. The parameters of the simulation are: $R_t/a = 0.12$, $R_g/a = 0.17$, $\epsilon = 10.1$.

tern, the Ex-field pattern and the Ey-field pattern of the third band at the Γ-point (Γ_3). This band is selected for the obtention of laser emission as it was mention in the Introduction of this chapter. This mode shows hexapole Hz distribution [156] being a nondegenerate Bloch mode.

4.3 Design of the 2D photonic crystal slab structure

Figure 4.3 b) shows the band structure of the hybrid triangular-graphite lattice and the Q calculated for the third band (TE-like mode) using the guided-mode expansion method (gme) in the symmetric approach [53, 51].[a] This approach has shown a good agreement between the calculated band structure of 2D PC waveguides embedded in air and SiO_2 [51, 52] and the measured counterparts. We have selected the Γ_3 point of the third band for the laser emission. At this point the photonic band structure presents a well isolated hexapole Bloch mode (Fig. 4.3 c)) with low dispersion and negative curvature around the Γ_3 point. This mode is uncoupled to the scattering states of the electromagnetic field at the Γ point keeping a large Q ($\geq 2 \times 10^5$) for a relatively wide set of values of in-plane $k_{||} \leq 0.1(2\pi/a)$ (see Fig. 4.3 b)). This high Q for large $k_{||}$ values can be explained as follows. When $R_g/a = R_t/a \leq 1/\sqrt{3}$, the hybrid lattice becomes a triangular lattice of pitch $a/\sqrt{3}$. The triangular lattice can be calculated either with the 2D Bravais lattice of the hybrid lattice, lattice constant a (Fig. 4.3 a)), or with its natural lattice constant ($a/\sqrt{3}$). Using the Bravais lattice of the hybrid structure (blue line in Fig. 4.4), the bands are folded within a Brillouin zone which area is a factor of three times smaller. The calculated photonic bands using the Bravais lattice of the triangular lattice with its natural constant $a/\sqrt{3}$ are also shown in Fig. 4.4 (red dots). The Γ_3 state of the hybrid lattice (see Fig. 4.3 b)) corresponds to a maximum of the first band at the K_1 point of the triangular lattice (see Fig. 4.4), which is below the light line. The mode of the triangular lattice is non-radiative, and is rendered weakly radiative by the small perturbation consisting in the different radius between the two sets of holes of the hybrid lattice. The mechanism for the formation of these high-Q states is unrelated with the flat

[a] The simulation has been done by Prof. L.C. Andreani from Università degli Studi di Pavia, Italy.

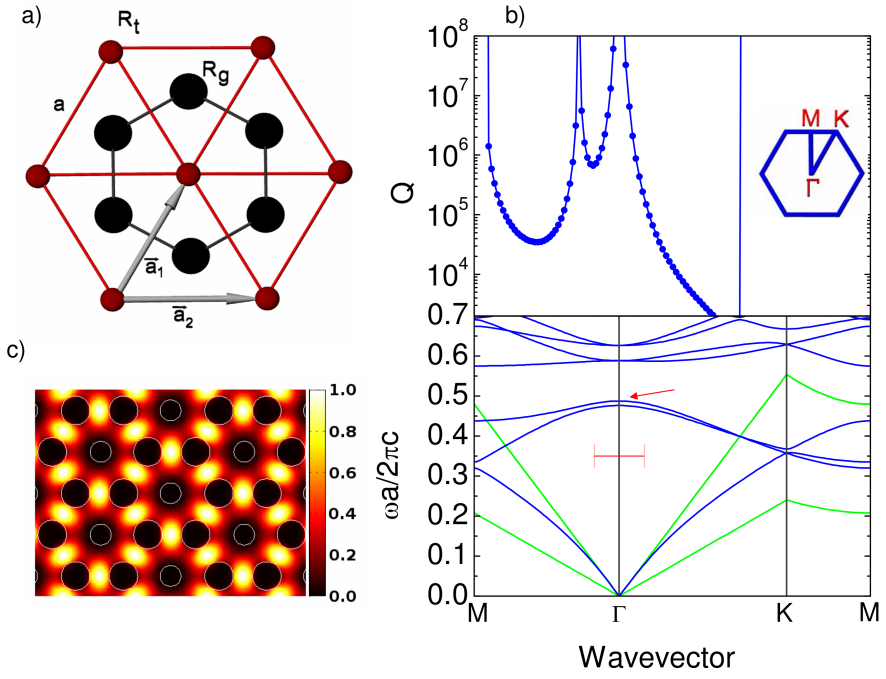

Figure 4.3: a) Schematic representation of the hybrid triangular-graphite lattice and the high symmetry directions in the k space. b) Calculated quality factor of the third band and photonic band structure (only even modes $\hat{\sigma}_{xy} = +1$ are plotted). Upper green line represents the light line with the average cladding dielectric constant. Bottom green line represents the InP light line. The red bar denotes the region with $k_{||}$ <0.1(2π/a) around the Γ point, where the Γ_3 band (indicated by a red arrow) is flat. c) Normalized E-field intensity profile at the Γ_3 point. The parameters of the gme simulation are: $a = 780$ nm, $R_t/a = 0.12$, $R_g/a = 0.17$, $\epsilon = 10.1$, $t/a = 0.304$. Being t is the thickness of the slab.

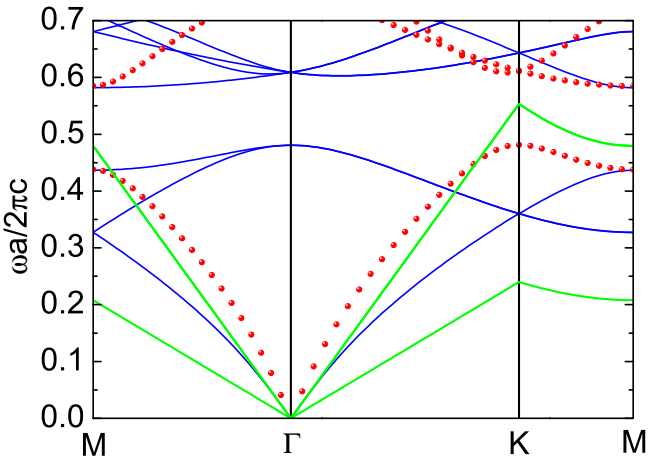

Figure 4.4: Photonic band structures (only even modes $\hat{\sigma}_{xy} = +1$ are plotted) of the triangular lattice calculated with the same filling factor that the hybrid lattice of Fig. 4.3 (b). The parameters of the gme simulation are: $a = 780$ nm, $R_t/a = 0.155$, $R_g/a = 0.155$, $\epsilon = 10.1$, $t/a = 0.304$. Blue line: calculated with the Bravais lattice of the hybrid triangular-graphite. Red dots: calculated with its natural Bravais lattice ($a \longrightarrow a/\sqrt{3}$). Green lines are the light lines of the average cladding and core materials.

.

bands of the hybrid lattice (which are number 4 and 5), and is more similar to the mechanism of heterostructure cavities [154], where a small perturbation in the lattice yields a very high Q. However, the Γ_3 state is a delocalized state (not a cavity mode) because the perturbation is periodic rather than localized. It must be noted that calculated Q corresponds to an infinite in-plane structure where there is no in-plane losses and the Q of the structure is limited by the vertical quality factor Q_v. For finite size structures, with lateral size L, the value of the Q calculated by the gme method, i.e., for an infinite lateral size structure, must correspond to the Q_v of the finite size structure assuming $k_{||} \sim 1/L$ is very close to Γ.

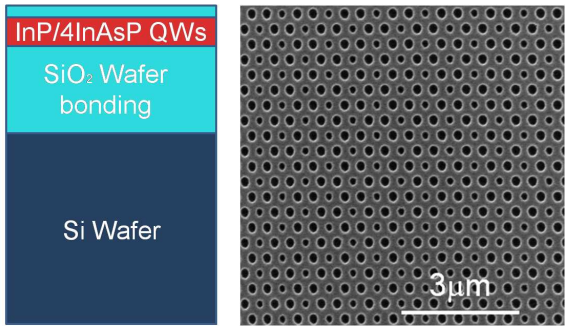

Figure 4.5: Left: Layout of the transversal section of the fabricated structures. Right: Scanning electron microscopy image of a fabricated structure. The lattice parameter is $a \simeq 780nm$, $R_t/a \sim 0.12$ and $R_g/a \sim 0.17$.

4.4 Fabrication and Optical characterization

4.4.1 Fabrication

The PC consists of an InP slab with a thickness of $t = 237$ nm. It contains four InAsP quantum wells as active layer grown by molecular beam epitaxy (MBE) on an InP wafer. A 300 nm InGaAs layer is used as sacrificial-stop layer in the selective wet etching. The structure is transferred to the top of a Si substrate by SiO_2 wafer bonding [78]. The thickness of the SiO_2 is 0.9 ± 0.1 μm. The InP carrier wafer is removed by wet chemical etching.[b] A 120 nm thick SiO_2 layer is deposited by plasma enhanced chemical vapor deposition. Processing of the PC structures was done by electron beam lithography on a polymethylmethacrylate (PMMA-A4) layer on top of the SiO_2. Reactive ion beam etching (RIBE) was used to open the holes in the SiO_2 by a CHF_3/N_2 mixture. The hard mask pattern was transfered to the semiconductor material by reactive ion etching (RIE) by a CH_4/H_2 mixture combined with O_2 plasma cycling [157]. After the process, a thick layer of SiO_2 ($\sim$ 80 nm) remains on top of the sample. The lateral size of the fabricated structures was 30×30 μm^2. Structures with lattice parameters ranging from 760 nm to 1050 nm were fabricated. Laser emission was obtained in structures with lattice constants

[b]The semiconductor material was provided by Institut des Nanotechnologies de Lyon, INL-Lyon, (France).

ranging from 760 nm to 815 nm. We have selected two structures with a=760 and a=780 nm (Fig. 4.5) in order to tune the selected Bloch mode with the optimum region of the photoluminescence (PL) spectra. The values of the hole radii have been kept around $R_t/a \sim 0.12$ and $R_g/a \sim 0.17$. It is important to note that structures from a=815 nm to 1050 nm with steps of 20-25 nm have been fabricated in other to probe higher energy bands. Nevertheless, no laser emission has been obtained from the higher energy bands. Moreover, the structures were fabricated in air suspended membranes and nonlaser emission was obtained for all of the probed bands including the third band. This is due to the high thermal resistivity of air suspended membranes that prevents the laser emission.

4.4.2 Optical characterization

The optical characterization was performed by microphotoluminescence (μ-PL) spectroscopy at room temperature. The structures were optically pumped with a 785 nm laser diode to a frequency of 1 MHz and a 2.5% duty cycle. An objective lens 5× (0.14 NA) was used to focus the excitation spot (diameter is $\sim$ 10 μm). The emitted light is collected through an optical fiber connected to an optical spectra analyzer or dispersed by a 0.85 m focal length double spectrometer with a cooled InGaAs photodiode array as detector.[c]

Laser emission from 1.55 μm to 1.57 μm has been obtained for different fabricated structures, with effective pump power [158] threshold around 70 μW, and Qs in the range 10000-12000. The absorbed pump power was obtained by the method described in Ref. [158]. The reflectivity of the InP was estimated to be $\sim$ 30%, and the absorption coefficient α=12900 cm^{-1} [159] giving an absorption fraction of $\sim$ 24%. Fig. 4.6 bottom shows spectra for two of the structures, A with a= 760 nm and B with a=780 nm, well below of the excitation pump power threshold. The spectra of both structures have a lorentzian lineshape more clearly noticeable at high excitation powers. At low excitation powers the PL background added with the Bloch mode emission yields a not lorentzian shape of the peak. A decrease of the linewidth and a blue-shift is observed as the excitation power is increased. The

[c] A detailed description of the optical characterization set-up was done in Chap. 5.

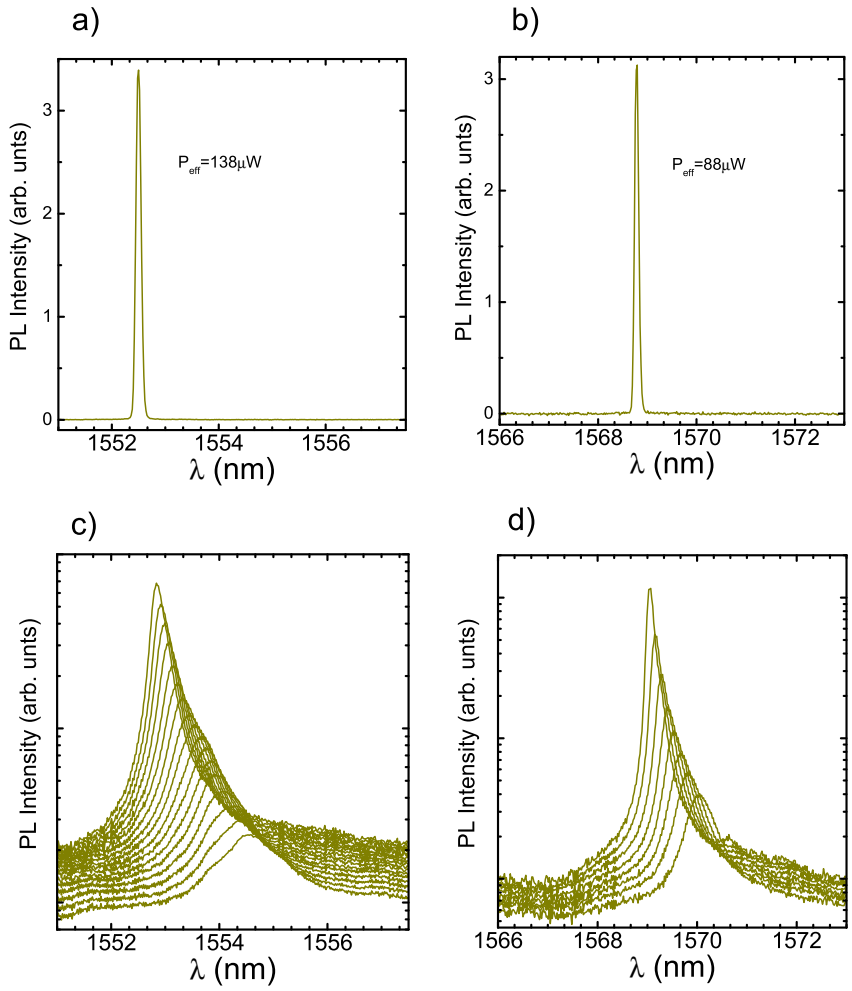

Figure 4.6: Top graphs shown spectra measured above the threshold for two structures: a) Spectrum of the A structure. b) Spectrum of the B structure. Bottom graphs shows the spectra measured well below the threshold for A, B structures. c) Spectra of the structure (A) with a=760 nm at excitation effective power range from 36 to 108 μW. d) Spectra of the structure (B) a=780 nm at excitation effective power range from 36 to 68 μW.

emission wavelength of the peak is in good agrement with the calculations (Fig. 4.3 b)).

Figure 4.7 shows the emission wavelength of the laser peak, the linewidth, and the integrated emission intensity versus the effective pump power for both structures. A clear non linear emission is observed with an effective pump power threshold $P_{th} = 120$ μW and with a Q=10000 just below the threshold for the structure A. Taking into account the excitation spot size, we obtain a threshold density of power excitation of ~ 150 W/cm^2. Similar behavior is observed for the second structure with $P_{th} = 70$ μW, Q=12000, and a threshold density of power excitation ~ 100 W/cm^2. It is important to note that we approximate the Q of the cold cavity for the value $\lambda/\Delta\lambda$ just below the lasing threshold [160]. This does not make sure that we are exactly at the transparency pump power, though. The Q measured bellow the threshold is similar for all the structures studied and is close to previously Γ-point 2D-PC lasers [35, 36] operating a 1.55 μm without bottom Bragg reflector. Nevertheless, the threshold value is around three times higher (in terms of incident peak power at threshold) than the reported in Ref. [36] on InAsP/InP substrates bonded to SiO_2. In that case, however, the pumping conditions are different.

The lasing linewidth well above the threshold is limited by the linewidth enhancement factor (α). The linewidth measured is not limited by the spectral resolution of our experimental set-up. For the sample A the linewidth saturates before than sample B (see Fig. 4.7). This means that $\alpha_A > \alpha_B$. Since the differential refractive index is mainly a material parameter, the variation of α from structure to structure has its source in the variation of differential gain [161]. On the other hand, α is inversely proportional to the emission wavelength and to the variation of the optical gain with the number of carriers (dg/dN). Then, we conclude that $(dg/dN)_B > (dg/dN)_A$. This means that the emission of sample B is in a better spectral position than for A, which implies the reduction in the power threshold, which is due to the best relation absorbtion-gain for the spectral position of the Bloch mode of the B structure and its higher Q [142]. The evolution of the peak position with the excitation power presented for both structures a linear behavior with two different stages. Below the threshold the blue-shift is faster than above the threshold as it is expected for lasers with good heat dissipation [162]. This is the common case for the structures wafer

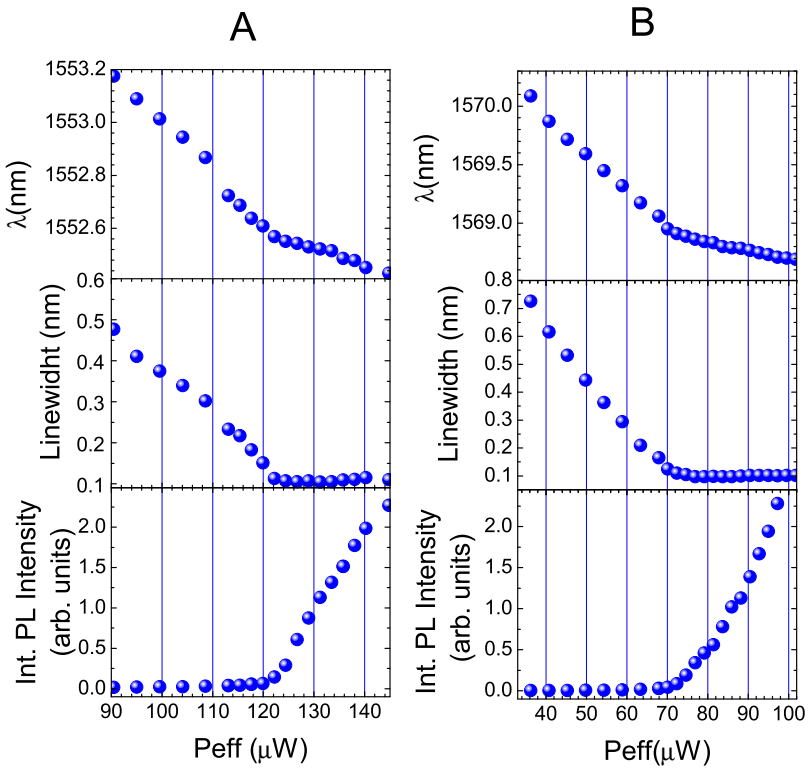

Figure 4.7: Evolution as a function of the excitation effective power. Left: Structure *A*. Right: Structure *B*.

bonded to a Si substrate [80]. The blue-shift above the threshold is due to the carrier induced modification of the refractive index [163, 81]. It has been shown in previous publications [163, 81], that free-carrier optical generation can significantly blue-shift the emission wavelength. Beyond threshold, free carrier density is clamped (at least partially [81]), which results in the observed saturation of the blue-shift.

In order to explain the Q measured in the fabricated structures an estimation of the Q of the finite size structures is necessary. Figure 4.8 shows the Hz field profile of the 2D PC slab with hybrid symmetry for a finite size structure calculated by three dimensional finite differences in the time domain (3D-FDTD). A clear localization

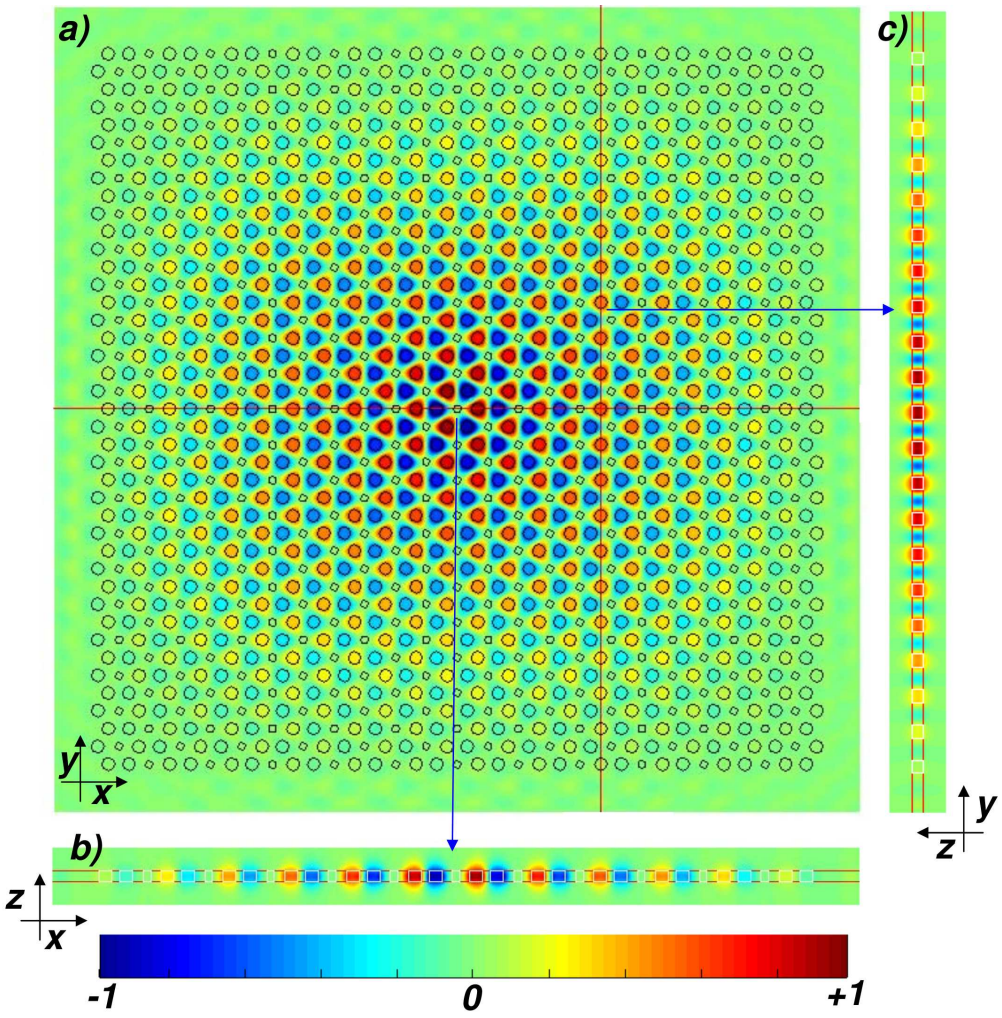

Figure 4.8: Normalized real part of the Hz-field calculated by 3D-FDTD. a) Pattern across the center of the slab (xy-plane). b) and c) Hz pattern of the vertical cross section along the lines of the a). Red lines. The parameters of the simulation are: $a = 780$ nm, $r_t/a = 0.12$, $r_g/a = 0.17$, $\epsilon_{slab} = 10.1$, $\epsilon_{SiO_x} = 2.1$, $t/a = 0.304$, and area $17\mu m \times 17\mu m$.

of the field around the center of the structure is observed. Figure 4.9 shows the evolution of the 3D-FDTD calculated Q of the third band at Γ for square structures of different areas.[d] An estimation of an upper value for Q for a structure of the size of the fabricated one was done by a linear extrapolation of the last two points of Fig. 4.9 (lower than ~ 8000). It must be noted that the value of the measured Q is slightly higher than the estimated for the finite size structure. This can be explained by the finite size of the mode and the reduction of the lateral leakage. The size of the mode can be controlled by the pump beam area through the carrier generation that induces (Kerr effect) a blue-shift of the resonance [163]. This effect results in a localization of the slow Bloch mode around a high symmetry extreme of the dispersion characteristics with negative curvature. The lateral extension of the Bloch mode is therefore limited to the pumping area [149]. The lateral leakage is due to the finite size of the structure and the matching of its modes with the waveguide modes [54]. In our case the above mentioned effects are not enough to explain the important increase of the Q compared to the estimated. We attribute this increase to the effect of a small variation of the radii of the holes close to the edges of the structure. As it has been recently demonstrated [137, 68, 164] a slight variation on the size of the features close to the edges dramatically reduces the in-plane lateral leakage.

In Γ-point PC structures with finite size there are two mechanisms of the Q limitation. The first one is the lateral escape of photons at the edges of the structures. The second is due to the finite size of the mode that contains photons with $k_{||} \neq 0$, then vertical losses around Γ appear that can be significant. In the hybrid triangular-graphite lattice the Bloch mode selected presents a high Q_v for a wide range of $k_{||}$ in-plane vectors around Γ that reduces the vertical losses due to the finite size of the mode. This may allow the design of a Γ_3 point heterostructure [154] to suppress the lateral leakage with smaller lateral size and much significantly higher Q [137][e]. Moreover, the intensity of emission could be enhanced combining the structure with a bottom Bragg reflector [52].

[d] The simulation for the fabricated structure (900 μm^2) was not carried out due to the required computational power.

[e] Preliminary, results show $Q \simeq 1.5 \times 10^5$ in a microcavity PC based in this kind of confinement above the light line (see Appendix A).

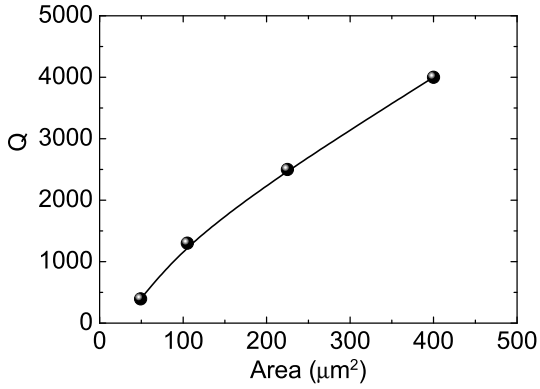

Figure 4.9: Evolution of the Qf third band of the hybrid lattice with area of the structure calculated by 3D-FDTD. The parameters of the simulation are: $a = 780$ nm, $r_t/a = 0.12$, $r_g/a = 0.17$, $\epsilon_{slab} = 10.1$, $\epsilon_{bg} = 2.1$, $t/a = 0.304$. Dots: simulated points. Black line: guide to the eye.

4.5 Summary

We have demonstrated room temperature surface emitting PC laser operating around 1.55 μm using the PC structure of the hybrid triangular-graphite lattice. By optical pumping the structure presents a low threshold of excitation power (∼70-120 μW). Qs ranging from 10000 to 12000 have been measured.

The Bloch mode (Γ_3 point) selected for the vertical emission presents a high Q for a wide range of $k_{||}$ in plane vectors around the Γ point. This high Q is explained by the correspondence of this mode above the light line with the first K point of the triangular lattice below the light line which is rendered weakly radiative due to the perturbation induced by the two sets of holes of the hybrid lattice. Furthermore, the hybrid structure provides a new physical mechanism for vertical lasing and high Q. This allows the design of a Γ_3 point heterostructure to inhibit the lateral leakage of the photons giving place to a PC structure with very high Q, relative small modal volume, and vertical directional emission.

Chapter 5

Room temperature laser operation in a PCM with a single layer of InAs/InP self-assembled quantum wires

Laser emission in a photonic crystal microcavity operating at 1.5 μm at room temperature is demonstrated in the continuous and pulsed optical excitation. The structures have been fabricated in an InP slab including a single layer of self-assembled InAs/InP quantum wires as active material. Continuous wave laser emission in air suspended membranes with thresholds of effective optical pump power of 22 μW and quality factors up to 55000 have been measured. Effective pump powers thresholds below 2 μW have been measured using pulsed pumping. In this excitation regime, asymmetric lineshapes just above the threshold and multipeak emission as the excitation power is increased have been measured. Further, the energy splitting among the peaks, which is in the range of meV to μV, is increased with the excitation power.

5.1 Laser emission under continuous wave excitation

5.1.1 Introduction

The development of high-density optoelectronic integrated circuits may benefit from the large integration capacity of micro/nanolasers. These light sources should exhibit low power consumption and low footprint and can be operated at higher temperatures and at higher modulation rates than conventional lasers [23]. Due to their ability to tailor the light in the wavelength scale, photonic crystals (PCs) have attracted strong attention enabling the development of two dimensional PC slabs with photonic crystal microcavities (PCMs) [78]. These photonic microstructures confine the light in a volume of the order of a cubic wavelength and present high quality factors (Q) [12, 102] being therefore ideal candidates for the fabrication of more efficient light sources [23, 44].

Quantum wells (QWs) or quantum dots (QDs) have been used mainly as the gain medium in PCM lasers. Our approach is to use a single layer of self-assembled InAs/InP quantum wires (QWrs) [95] as active material. Due to the reduced dimensionality of the QWrs compared with QWs we should expect several advantages like a lower threshold for laser emission [97, 165], reduced temperature sensitivity [90], reduction of the linewidth enhancement factor [166], reduced surface recombination [167] (which is very important in structures like PCM with many material-air boundaries), good lateral carrier confinement and in-plane polarization anisotropy [95]. Also, InAs/InP QWrs offer the possibility to tune the spontaneous emission beyond 1.6 μm [168, 169], which is very interesting for practical applications such as gas sensing and molecular spectroscopy. Finally, compared to QDs, the QWrs allow a good compromise between their lateral confinement and the active-medium volume and can also be fabricated isolated using patterned GaAs substrates [170] or by self-assembled methods on InP [94] for single QWr lasing applications.

Low temperature self-tuning lasing operation around 0.9 μm has been demonstrated using a single layer of low density InAs/GaAs QDs in a PCM [22]. Similarly, lasing at ~ 1.2 μm in a PCM has been obtained using a single layer of high density InAs/GaAs

QDs [171]. To demonstrate room temperature (RT) lasing around 1.3 μm in a QD based GaAs PCM, it was necessary to stack five self-assembled InAs/GaAs QD layers as active material [172, 173, 174]. Meanwhile, laser emission at 1.5 μm at RT using pulsed optical excitation has been demonstrated both, in a compact "2.5 D" PC Γ-point laser [80] and in an air suspended PCM [164], containing a single layer of InAs/InP QDs as gain medium. Continuous wave (CW) optically pumped laser operation at 1.6 μm was demonstrated in an InP slab, on top of Al_2O_3, using multiple (six) InGaAsP/InP QWs and an hexagonal PCM with a diameter size of $\sim$ 10 μm [175]. Finally, using a multiple (four) GaInAsP/InP quantum wells Nozaki *et al.* [64] showed RT continuous wave (CW) lasing at 1.5 μm in a PC nanocavity (which is the PCM with the ultimate-small modal volume,[a] $V = 0.15(\lambda/n)^3$), with thresholds around 1.2 μW of absorbed pump power (P_{eff}). All of these experiments were done with no resonant pumping.

In this first part of the chapter, it is shown RT lasing at 1.5 μm using CW non-resonant optical pumping of a PCM air suspended membrane containing a single layer of InAs/InP self-assembled QWrs. Our devices are based on L7-type [107] PCMs with high quality factors $Q \simeq 55000$ and threshold values of P_{eff} $\sim$22 μW.

5.1.2 Design and fabrication

Epitaxial material

The starting material consists of a single layer of self-assembled InAs/InP QWrs grown by solid source molecular beam epitaxy and embedded in a 237-nm-thick InP slab[b]. An $In_{0.53}Ga_{0.47}As$ layer of 700 nm thickness layer is used as sacrificial layer for the membrane realization. Fig. 5.1 a) shows an atomic force microscope image (AFM)[c] of an uncapped sample containing QWrs. The QWrs morphology is clearly elongated along the $[1\bar{1}0]$ crystal direction with average width, height and pitch period of 15 nm, 3.6 nm and 18 nm, respectively. Their length exceeds 1 μm

[a] It is remarked by the authors that is close to the lower limit for an optical cavity.
[b] The epitaxial material was provided by Dr. D. Fuster and Prof. L. González.
[c] AFM image courtesy of Dr. D. Fuster and Prof. L. González.

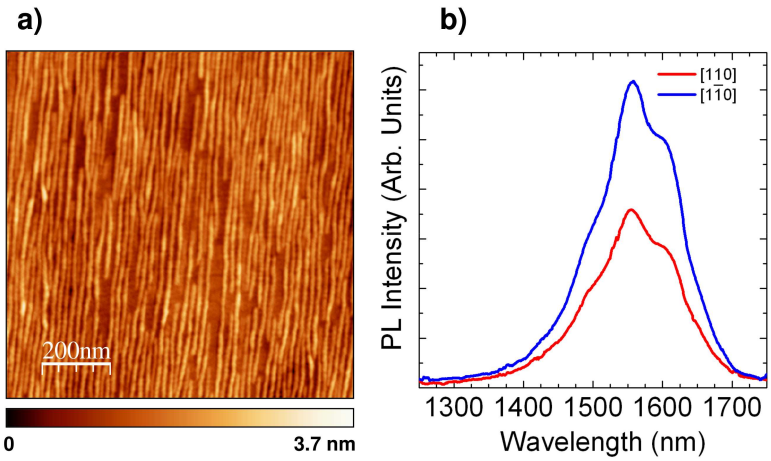

Figure 5.1: a) Atomic force microscope (AFM) image of an uncapped sample of self-assembled InAs/InP QWrs. b) Room temperature polarization resolved photoluminescence spectrum of the quantum wires sample without photonic crystal structure. Blue color [1$\bar{1}$0] crystal direction. Red color [1 1 0] crystal direction.

in most cases. Fig. 5.1 b) contains a polarization resolved RT photoluminescence emission spectra of the gain medium detected with a Ge cooled detector (detector peak sensitivity at 1.63 μm) and shows that the emission is broad and finds its maximum at 1.56 μm. These QWrs exhibit more than 20% of linear polarization anisotropy along their elongated direction in the emission range from 1450 nm to 1650 nm, in agreement with previous works [95]. More details about the growth procedure and optical properties of these QWrs can be found elsewhere [95, 168].

Photonic crystal structure

A triangular lattice of air holes was selected as the PC structure which presents a large photonic band gap for the even modes ($\sigma_{xy} = +1$), also called TE-like modes. A L7-type cavity is selected as PCM, which is created filling seven holes along the ΓK direction of the triangular lattice. The L7 cavity belongs to the Ln group of PCMs whose modes can be classified as either even ($\sigma_{xz} = +1$) or odd ($\sigma_{xz} = -1$) with respect to mirror reflection along the longitudinal direction of the cavity (XZ

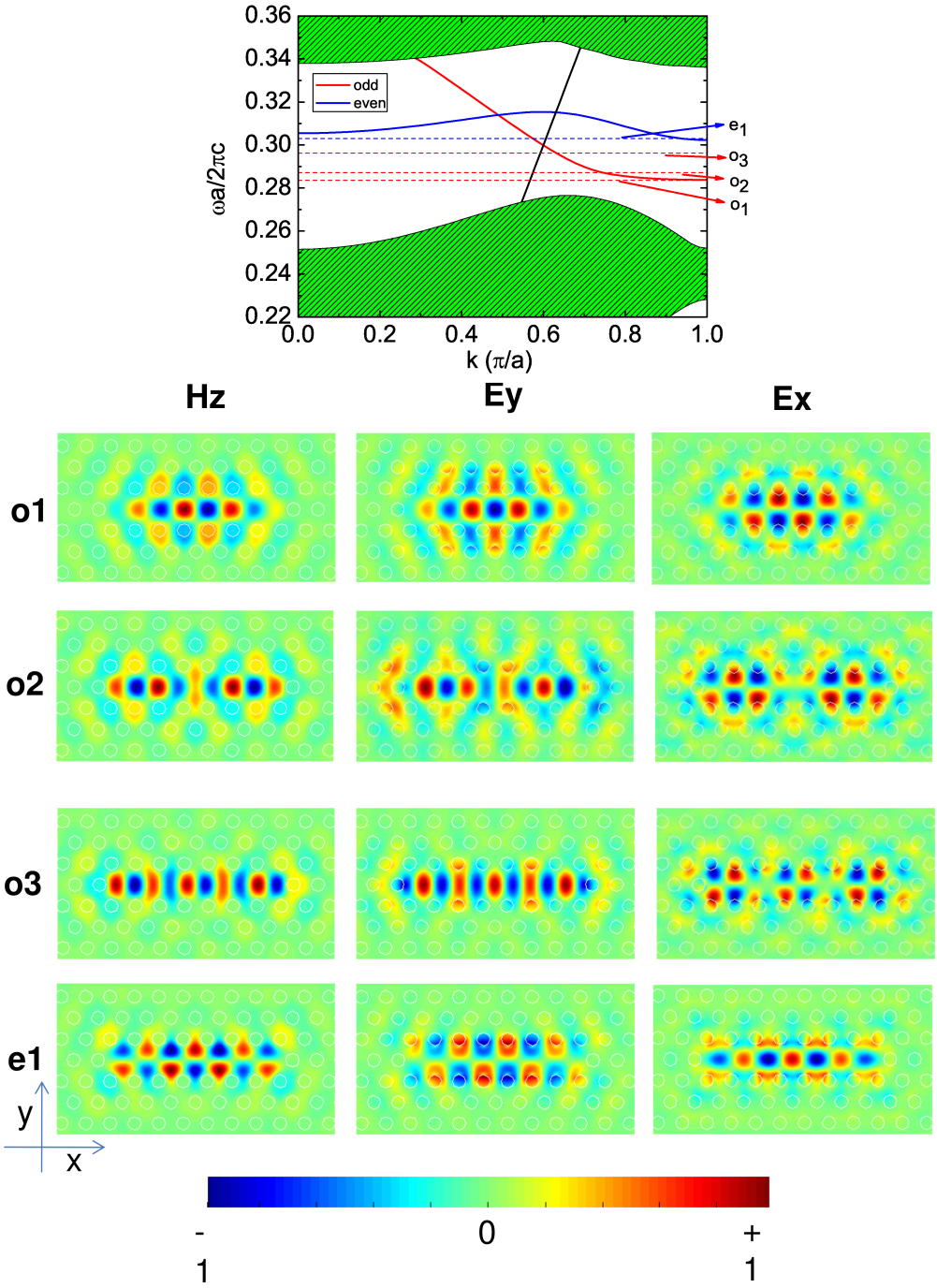

Figure 5.2: Up: Relation dispersion of the W1 PCW and spectral position of the four low-energy modes of the L7 PCM. Only even $\sigma_{xy} = +1$ are plotted. Red color $\sigma_{xz} = +1$ modes. Blue $\sigma_{xz} = +1$. Down: Normalized H_z, E_y, E_x field patterns of the four low energy modes of the L7 PCM.

plane) [62], in analogous way with a PC waveguide (W1) [176], where all holes of the row are eliminated along the ΓK direction for creating the channel. Fig. 5.2 up shows the dispersion relation of a W1 waveguide, and the four low-energy modes of the L7 cavity. Only modes which are even with respect to a mirror reflection on the XY plane are plotted ($\sigma_{xy} = +1$). The parameters of the structure are the lattice constant, a = 440 nm, the hole radius rate, r/a =0.27 and the thickness of the slab, d = 237 nm. The L7 cavity presents a low energy mode at $\omega a/2\pi c \simeq 0.283$ with calculated Q=70000, small modal volume V=1.2$(\lambda/\mathrm{n})^3$, and relative high effective index n_{eff} =2.78 calculated using the guide-mode expansion method [53].[d] In addition, the fundamental mode emission is well isolated ($\Delta(o_1 - o_2)\lambda \simeq 18$ nm) from the higher order modes and can potentially exhibit high β values as it has been demonstrated in PCMs with InAs/GaAs QDs as active material [177]. Fig. 5.2 shows the field profiles of the four low energy modes calculated by 3D-FDTD [109]. The fundamental mode (o_1), the o_3 mode, and e_1 mode have *"well-defined"* symmetry properties, i.e., the E_x, E_y field patterns are symmetric with respect to the XZ plane and the YZ plane or antisymmetric with respect to those symmetry planes. Taking into account that double symmetric (with respect to both symmetry axes) is required for the coupling to the exactly vertical scattering states of the field component and that double antisymmetric (with respect to both symmetry axes) produce the cancelation of the overlap between the confined states and scattering states, the field component considerated is inhibited [178]. Then, the y polarization is favored for the mode o_1 and the o_3 mode. Nevertheless, the x polarization is favored for the e_1 mode. It is important to note that E field patterns of the o_2 mode are not totally symmetric/antisymmetric. This does not provide purely vertical emission [178], and in order to determine which polarization component is favored, a simulation taking into account the k-range of collection of our experimental set-up is necessary. This can be done, for example, by 3D-FDTD [41][e]. Nevertheless, according to the work of S.-H. Kim *et al.* [62] polarization perpendicular to the longitudinal direction of the cavity is expected and was measured by C. F. Wang *et*

[d]The gme simulation of the L7 cavity was done by Dr. D. Gerace and Prof. L. C. Andreani from Università degli Studi di Pavia, Italy.

[e]The Lumerical package provides a tool for obtaining the far field patterns of the microcavity modes.

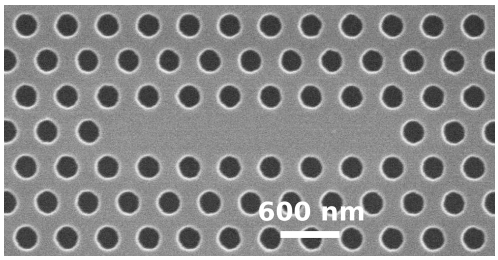

Figure 5.3: Scanning electron microscope image of the fabricated L7-type photonic crystal microcavity. The lattice parameter is $a = 440$ nm and the value of $r/a \sim 0.27$.

al. [108] in diamond material. The Qs and V obtained for the next higher energy modes are: $Q_{o2} \simeq 10000/V_{o2} \simeq 1.2(\lambda/n)^3$, $Q_{o3} \simeq 2000/V_{o3} \simeq 1.2(\lambda/n)^3$ and $Q_{e1} \simeq 3500/V_{e1} \simeq 1.3(\lambda/n)^3$ being the separation between then $\Delta(o_2 - o_3)\lambda \simeq 43$ nm, and $\Delta(o_3 - e_1)\lambda \simeq 32$ nm. In agreement to this, the cavity optical features of this PCM can be univocally determined by the optical measurements.

Fabrication

A 120 nm thick SiO_x layer was deposited by plasma enhanced chemical vapor deposition on top of the InP epitaxial material. Processing of the PC structures was done by electron beam lithography on a polymethylmethacrylate (PMMA-A4) layer on top of the SiO_2. Each cavity is surrounded by eleven rows of holes to minimize the in-plane losses. Reactive ion beam etching (RIBE) was used to open the holes in the SiO_2 by a CHF_3/N_2 mixture. The hard mask pattern was transferred to the semiconductor material by reactive ion etching (RIE) by a CH_4/H_2 mixture combined with O_2 plasma cycling. After the process, a thick layer of SiO_2 remains on top of the sample. That was eliminated using a solution of hydrofluoric acid water diluted $HF(1) : H_2O(5)$ during 90 s. For the obtention of the PC membrane the sample was submerged in a $HF(1) : H_2O_2(1) : H_2O(20)$ solution under etch rate control. For more details about the fabrication process see Ref. [157]/Chap.2. Several PCM with an evolution in the value of the r/a ratio were fabricated in the same wafer. Figure 5.3 shows a scanning electron microscope image of one of the

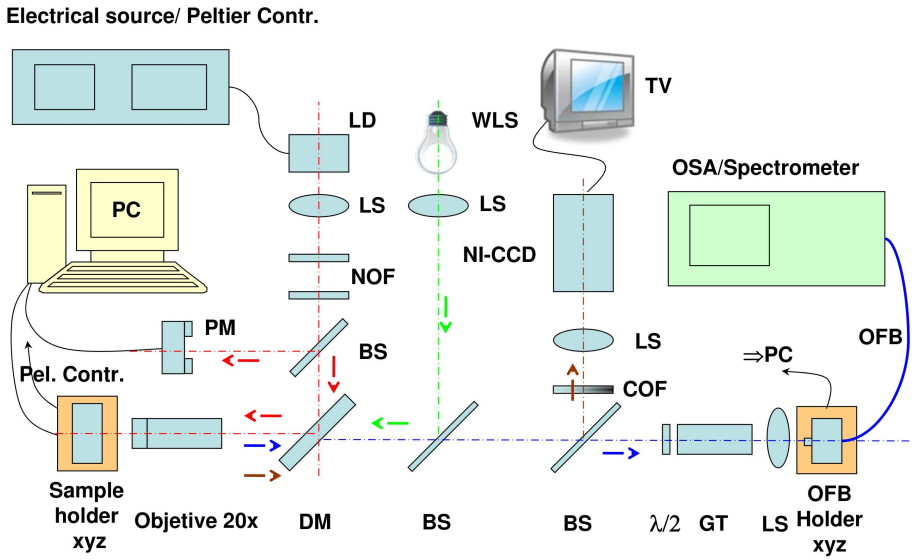

Figure 5.4: Diagram of the optical characterization set-up.

fabricated PCMs. The holes present a circular shape with a high homogeneity in position and size.

5.1.3 Optical characterization

Microphotoluminescense experimental set-up

Figure 5.4 shows a diagram of the experimental set-up used for the optical characterization. The excitation laser is a 785 nm single mode laser diode (LD), temperature controlled by a peltier module, and electrically pumped in CW or pulsed regime. The emitted light is collimated by a high numerical aperture (0.55 NA) lens (LS) and passed through two neutral variable optical filters (NOF) in order to control the optical power flux. A beam splitter (BS) is positioned after the NOF to split part of the light to a power meter (PM). The light is reflected by a dichroic mirror (DM) and focused over the sample with a long working distance microscope objective. The emitted light is collected by the same objective and focused into an

optical single/multimode fiber (OFB) by a low numerical aperture LS. The fiber is connected to an optical spectrum analyzer (OSA) or a 0.85 m focal length double spectrometer using as detector a cooled InGaAs photodiode array or a near infrared photomultiplier. Before the LS a half-wave plate ($\lambda/2$) and a Glan Thompson polarizer (GT) are placed in order to do polarization resolved measurements. The sample holder, temperature controlled by a peltier module, is placed in a stage with three piezo-electrical motors (computer-controlled) for a precise sample position control, as well as the optical fiber. Along this optical path two abatable BSs are used: The first for providing the sample light illumination with a white light source (WLS) and a LS. The second for either observing the sample image or the far field emission pattern focusing the light by a LS in a CCD/NI-VD[f] camera. Color optical filters (COF) are placed along the way in order to select the optical mode image. Changing the position of the CCD along the axis the Fourier image of the emitted light can be obtained [179].

Optical measurements

The optical characterization was performed by microphotoluminescence (μ-PL) spectroscopy at room temperature. The sample temperature was kept slightly above RT (26±0.1°C). The structures were CW optically pumped with a 785 nm laser diode. An objective lens 20× (0.40 NA) is used to focus the excitation spot (diameter $\sim 1.5\ \mu m$) over the sample. The emitted light was collected by the same objective lens and focused in a single-mode optical fiber coupled to a 0.85 m focal length double spectrometer. A cooled InGaAs photodiode array was used as detector in this case.

A spectrum of the L7-PCM over study is shown in Fig. 5.5 a) over a CW excitation power bellow the threshold of the fundamental mode. This is the typical spectrum of a L7 PCM where the three odd low energy modes and the first even mode are observed . This behavior has been observed consistently in several PC structures over the same wafer (see Fig. 5.5 b)). It is important to note that these spectra have been measured with a 0.3 m spectrometer, using an InGaAs photodiodes array as

[f]Near infrared vidicon camera (NI-VD).

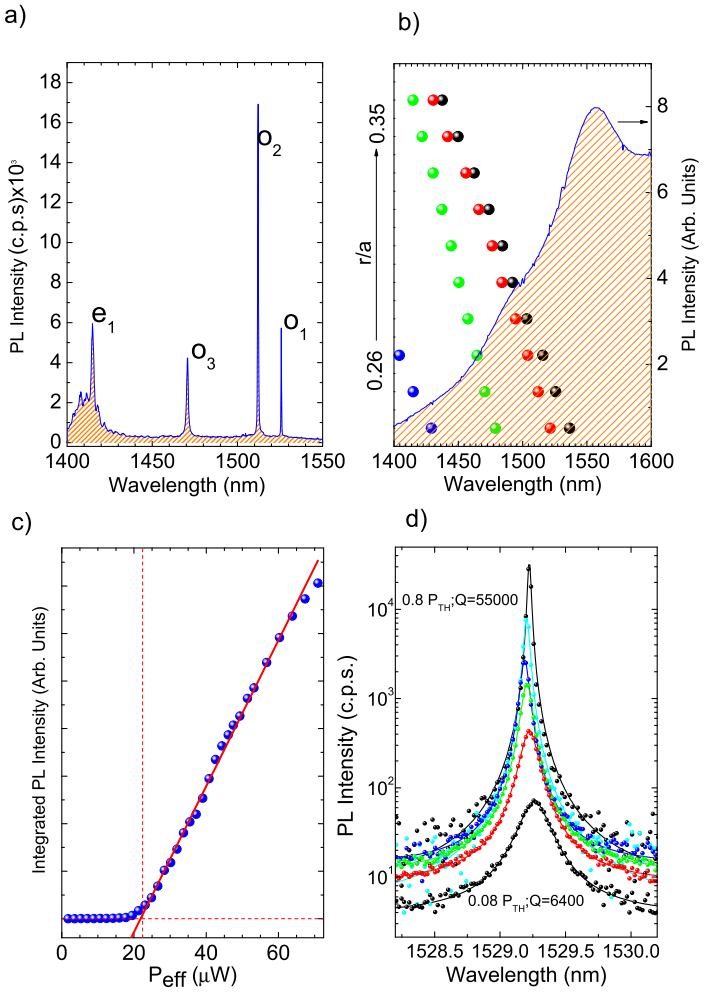

Figure 5.5: a) Spectrum of a L7 PCM below the threshold of the low-energy mode. b) Spectral position of several L7-PCMs with r/a ranging from ∼0.26 to ∼0.35. Filled dots indicates the four low energy modes. Continuous line: wafer PL. c) Integrated PL intensity versus effective excitation power (blue dots) of the fundamental mode (o_1) of the spectrum in a). Red line is the linear fitting for the data measured above the kink. Dashed line indicates the threshold power ($P_{th} = 22\mu W$). d) Logarithmic plot containing several emission spectra measured below threshold (dots). Continuous lines stand for the corresponding lorentzian fits.

detector, since the spectral range of the measurements is quite long to be measured with the high resolution spectrometer (0.85 m double spectrometer).

Figure 5.5 c) shows the non-linear behavior of the integrated emission intensity versus the absorbed pump power (L-L curve) for a PCM oriented along the $[1\bar{1}0]$ direction (parallel to the QWrs). This geometry has been investigated before using InGaAs QWrs stacked on V-groove patterns on GaAs with the result of laser emission between 2 and 70 K under pulsed excitation [170, 180]. To this respect, we must note that our PCMs fabricated along the perpendicular QWrs direction ([110]) do not show laser emission which we tentatively attribute to the enhanced surface recombination at the material/air surfaces [181]. On the other hand, laser emission was consistently observed in parallel PCMs fabricated in the same sample. The absorbed pump power was obtained by the method described in Ref. [182]. The reflectivity of the InP was estimated $\sim$ 30%, and the absorption coefficient $\alpha = 12900\ cm^{-1}$ [159] giving an absorption fraction $\sim$ 24%. The curve shows a pronounced change on the slope with a clear kink. From the linear fit of the L-L curve above the kink, a threshold pump power of $P_{th} = 22\ \mu W$ is obtained. This value is close to compare (see table 5.1) with the values obtained in PCMs containing InAs/InP QDs operating at 1.5 μm under pulsed excitation [80, 164] and with the ones obtained in PCMs with GaInAsP/InP QWs [64, 182] and microdisks with InAs/InP QWrs [167] in the CW pumping regime. Figure 5.5 d) shows a logarithmic plot of the spectra measured below threshold for effective excitation powers between $0.08P_{th}$ and $0.8P_{th}$. At the highest power, we estimate Q=55000 from lorentzian fit to the data with the minimum linewidth that we can measure with confidence in our experimental setup. The measured quality factor is among the highest obtained in active InP PCMs [64, 128, 69].

Figure 5.6 shows the evolution of the emission peak wavelength as a function of the excitation power. The spectral peak position shows an initial blue-shift for low excitation power attributed to the variation of the refractive index with carrier density as reported for air suspended PCM microlasers [183]. As the excitation power increases, due to the CW excitation, the thermal effects become important and produce an opposite change in the refractive index resulting in a red-shift of the emission peak. Similar behavior has been observed in GaAs PCM microlasers

Ref.	**Photonic structure**	**Active material**	**Pumping conditions (nm,ns,%)**	**Absorbed peak pump power (μW)**	**Q** $\times 10^4$
[80]	Γ-Point PCM	InAs/InP QDs	(780,6,1.2)	380	<1
[164]	PCM	InAs/InP QDs	(780,2,1)	80	1.6
[64]	PCM	GaInAsP/InP QWs	(980, CW)	1.2	2.0
[182]	PC-Microgear	GaInAsP/InP (5×) QWs	(980, CW)	14	—
[175]	PCM	InGaAsP/InP (6×) QWs	(980, CW)	∼900	—
[167]	Microdisk	InAs/InP QWrs	(800, CW)	$\sim 10^3$	∼0.1

Table 5.1: InP-based microlasers operating a 1.5 μm. At fourth column the excitation power conditions are indicated as follow: excitation wavelength, duty cycle width and duty cycle fraction.

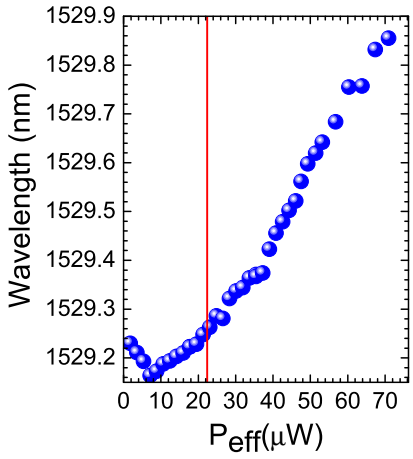

Figure 5.6: Emission peak wavelength versus effective excitation power. Red line shows the threshold power.

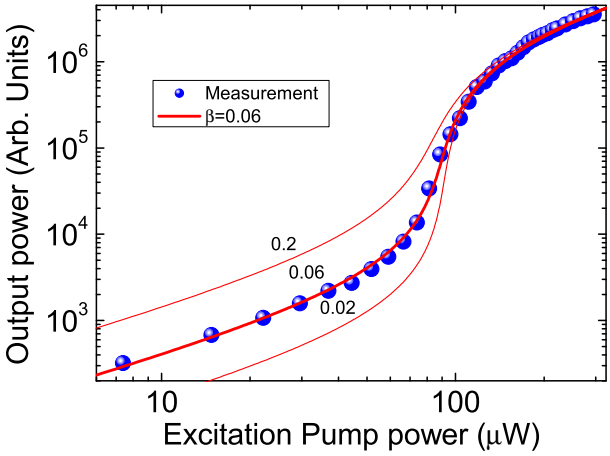

Figure 5.7: Log-log plot of the integrated emission intensity versus the excitation pump power. Blue dots are measured data. Red lines are the calculated curves extracted for the indicated β values with $g = 7.7 \times 10^{-15}$ cm^2 and $N_{tr} = 2 \times 10^{17}$ cm^{-3}.

operating at room temperature in the CW excitation regime [173] and it is absent in PCM in the pump pulsed regime where the thermal effects are overcome and only the blue-shift is observed.

Rate equations analysis

A further analysis of the emission characteristics of our QWrs based PCM laser has been done solving the microcavity laser equations [22, 150]:

$$\frac{dN}{dt} = R_p - \frac{N}{\tau_r} - \frac{N}{\tau_{nr}} - G(N)P. \tag{5.1}$$

$$\frac{dP}{dt} = \Gamma G(N)P + \beta\frac{N}{\tau_r} - \frac{P}{\tau_c}. \tag{5.2}$$

Here, N stands for the carrier density, P is the photon density, R_p is the incident

pump rate, $(\tau_r, \tau_{nr}, \tau_c)$ are the radiative, nonradiative and cavity photon lifetimes, respectively, Γ is the confinement factor, and $G(N)$ is a linear gain function $G(N) = g\frac{c}{n_{eff}}(N - N_{tr})$ with g standing for the differential gain coefficient and N_{tr} for the transparency carrier density. The β represents the rate of the spontaneous emission into the lasing mode over the total spontaneous emission in all the modes.

In equation 5.1, the first term represents the pumping rate; the second term represents the spontaneous emission decay which is enhanced in a PCM due to the Purcell effect; the third term is the non-radiative losses, and the last term the decay of the excited state due to the stimulated emission (also called the stimulated emission term). In equation 5.2 the first term represents the optical gain, i.e., the gain of photons due to the medium optical gain; the second term represents the photon spontaneous emission in the lasing mode (the gain of photon due to the spontaneous emission into the lasing mode), and the last term the photon cavity losses (given by the Q).

Figure 5.7 shows the L-L curve in double log scales and the evolution calculated using the indicated spontaneous emission factors β. The value of τ_c was obtained directly from the measured Q =55000. The radiative lifetime[g] $\tau_r = 2$ ns is approximated by the characteristic of these QWrs at 77 K [181] and Γ ∼0.02 can be estimated for our PCM lasers from the cavity mode volume and the overlap with the active medium. The non-radiative rate is given by $\frac{1}{\tau_{nr}} = \frac{v_s}{d_a} + C_{Aug}N^2$ with the propagation distance d_a and velocity v_s for surface recombination and the Auger recombination coefficient given by their nominal values in InP [150]. We have varied N_{tr}, β and g looking for the best fit to our data. Since these parameters are not independent, the value of β can not be determined without knowing the material gain $g \times N_{tr}$. In our case, given the high Q value, $N_{tr} = 2 \pm 0.5 \times 10^{17}$ cm^{-3} can be estimated from the position of the threshold with reasonable accuracy in a broad range of (β, g) from $(0.02, 10 \times g_0)$ to $(0.2, 100 \times g_0)$, where $g_0 = 3.0 \times 10^{-16}$ cm^2. Assuming a material gain ≈ 1500 cm^{-1} as for an InGaAs QW (lower gain is not expected for the QWrs) [150], we deduce a spontaneous emission factor $\beta = 0.06$ for our PCM laser based in a single layer of QWrs. As expected for one dimensional systems, the

[g]Courtesy of J. Canet-Ferrer, G. Muñoz Matutano, and Prof. J. Martínez Pastor from Universidad de Valencia.

transparency carrier density calculated this way is one order of magnitude smaller than in samples with QWs [183, 150] but still substantially larger than the value reported for PCM lasers with InAs/GaAs QDs [22, 184]. Our analysis suggests, within the uncertainties above mentioned, a differential gain $g = 7.7 \times 10^{-15}$ cm^2 and a spontaneous emission factor much larger than in conventional lasers.

5.2 Laser emission under pulsed excitation

5.2.1 Introduction

One of the characteristics of the PCM is that can exhibit a discrete modal spectrum with well separate modes and in the spectral region among the modes the spontaneous emission is strongly inhibited [46, 18]. Taking advantage of this, several high efficiency PCM lasers have been fabricated on different materials and with different active medium [22, 174, 23, 80, 164].[h] Typically a non-degenerate and high Q mode is selected providing single mode laser operation. In addition, the lineshape well above the threshold is lorentzian [83] and the linewidth collapse is prevented by carrier-carrier interaction of the gain media [185].

Our PCM laser consist of a L7-type PCM [107] fabricated on an InP slab containing as active material a single layer of self-assembled quantum wires (QWrs). The optical pumping is non resonant and it is pulsed. Room temperature (RT) laser emission at 1.5 μm with Q$\simeq$55000 and efective pump power thresholds below 2 μW have been measured. As the excitation power is increased, the peak lineshape evolves from a lorentzian to an asymmetric lineshape. Just above threshold the fundamental mode broadens and the lineshape becomes increasingly asymmetric towards lower energies. Increasing further the excitation density different peaks appear predominantly at lower energies. The energy splitting among these peaks increases with the excitation power.

[h] For a more detailed description see Section 5.1.1.

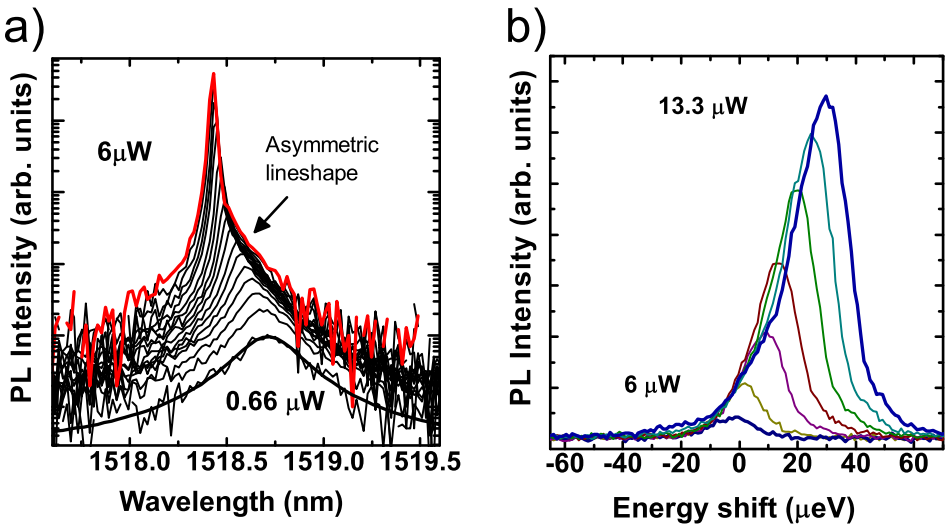

Figure 5.8: a) Logarithmic plot of the measured spectra around the threshold value. b) Linear plot of the spectra above the threshold. The zero at the x axis represents the peak energy at the threshold.

5.2.2 Optical characterization

The sample was characterized by μ-PL spectroscopy. A description of the experimental set-up is showed in the Sect. 5.3.1. All our measurements were performed at room temperature (26±0.1°C) with the sample held in a close-loop Peltier module. The fabricated PCMs were optically pumped by a 785 nm diode laser. This energy of excitation is well above the electronic InP gap and non resonant with any QWr transition. The excitation spot was focused over the sample by means of a 20× microscope objective (0.40 NA) with a spot size (∼1.5 μm). The emitted light was collected by the same objective and focus in a single mode fiber connected to a 0.85 m focal length double spectrometer using a cooled InGaAs photodiode array or a near infrared photomultiplier as detector. Due to the high thermal resistance of an

air suspended membrane the heating effects can be important, preventing in some cases the laser emission [64], stable laser action [186] and producing an emission redshift. In order to avoid the thermal issues short excitation pulses with long dwell times must be used. In our case, we chose 25 ns pulse widths which should be long enough to achieve a stationary state regarding the QWrs dynamics at RT. With a duty cycle of 2.5%, this translates into pulsing frequency of 1 MHz.

Low excitation

Figure 5.8 a) shows a logarithmic plot of the spectra of emission of a PCM for an increasing excitation power around the threshold. It can be observed that the spectra evolves from a lorentzian shape, for excitation power below the threshold, to an asymmetric lineshape toward low energies just above this power excitation. Figure 5.8 b) shows the emission spectra slightly above the threshold. The asymmetric lineshapes towards low energy are clearly observed. Since the lineshape of a laser above the threshold is lorentzian and the linewidth decreases as the excitation power is increased, the asymmetric lineshape, and the increasing width of the peak with the excitation power were unexpected in our laser.

Let us consider the excitation power range lower than three times the threshold value for two of the PCMs fabricated. In this range of excitation power only one peak is observed in the PL spectra. In figure 5.9 are plotted the peak position (λ) and Q_m (defined as $\lambda/\Delta\lambda$, which is a measure of the linewidth of the peak) as function of the average excitation power for two of the PCM fabricated. In addition, the integrated emission intensity versus the excitation pump power is also plotted. The red line indicates the excitation pump power threshold. The value of the threshold pump power has been obtained by the procedure described in Section 5.1.3. The first remarkable aspect is the evolution Q of both structures. The first one has $Q \sim 45000$, which is considered as the value $\lambda/\Delta\lambda$ just below the threshold pump power and the second one $Q \sim 55000$. Above the threshold power the value of $\lambda/\Delta\lambda$ tends to decrease. An increasing of the linewidth with the excitation pump power was measured by F. Bordas *et al.* [164] in a sample with InAs/InP QDs operating at 1.5 μm. The second remarkable characteristic is the evolution of the peak position

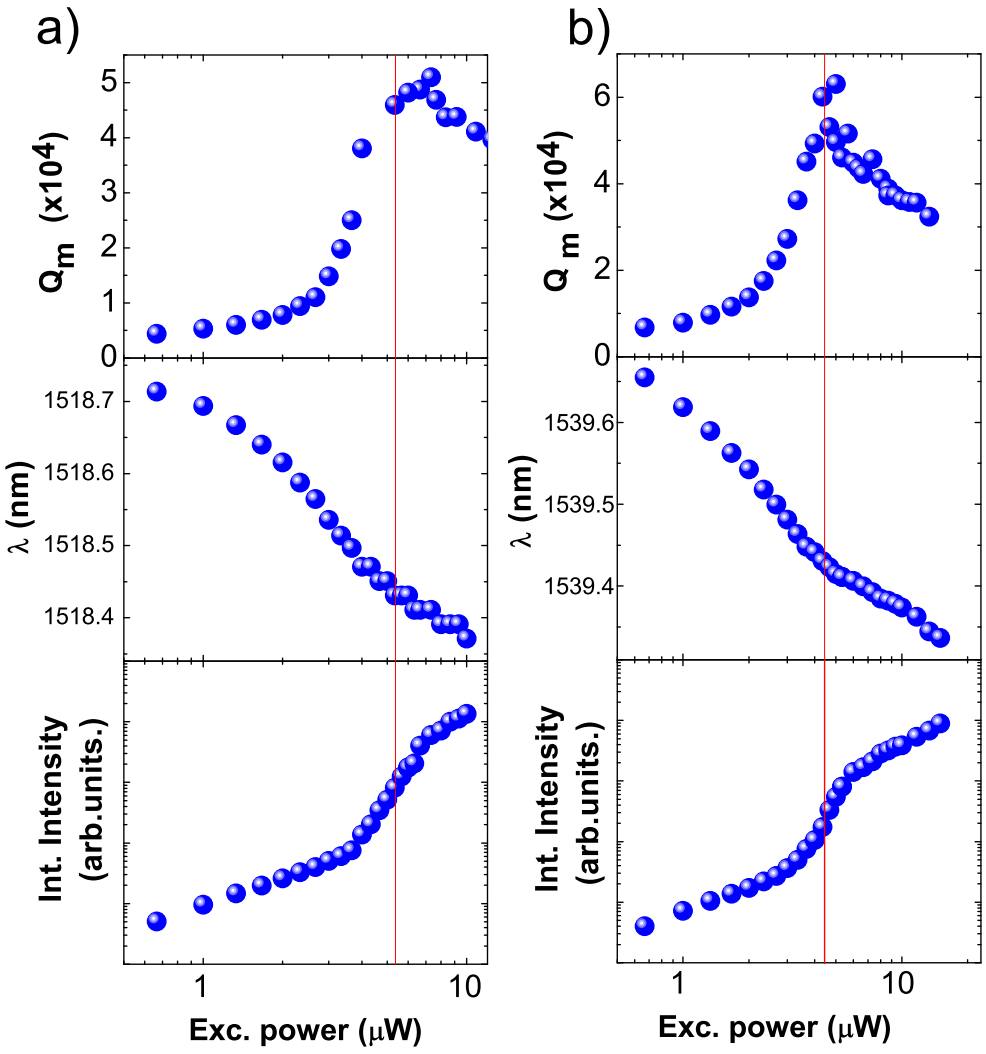

Figure 5.9: Quality factor $Q_m=\lambda/\Delta\lambda$, peak wavelengh position (λ) and integrated PL intensity plotted as function of the incident average pump power. a) PCM emitting around 1518.5 nm. b) PCM emitting around 1539.5 nm.

with the excitation power. The change in the peak position can be due to the thermal effects (red-shift) and the saturation of the material absorbtion (blue-shift). In our case, the monotonous blue-shift behavior of the peak should be due to the absorbtion reduction [164]. This behavior is similar to the one observed in PCM laser in the pump pulsed regime where there was an initial fast blue-shift becoming slower as the excitation power was increased [183]. The third data to remark is the average threshold pump power of both devices, P_{ex}=5.37 μW and P_{ex}=4.43 μW, which translates in an absorbed pump power of P_{eff}=1.3 (1.1) μW, since the absorbtion of the material is estimated on $\sim$24 % by the same procedure that in Section 5.1.3. This value is close to the one found for samples with InAs/InP QDs operating at 1.5 μm [80, 164].

High excitation

If we keep on increasing the average excitation power the differences with a "conventional" laser become more evident. Figure 5.10 shows contour plots in log color scale of the emission spectra for two PCM obtained spanning a much broader excitation range. As it can be observed, the laser threshold is just the *vertex of the pyramid*. Two regions have been highlighted and plotted separately in Fig 5.10 c) the *Region 1* and 5.10 d) *Region 2*, in order to show in more detail the complexity of the spectra.

Region 1 corresponds to the excitation range just above threshold where the spectrum changes from one single peak to multiple peaks. The number of peaks and their relative splitting increases with the excitation power leading to two distinct groups at high energy and low energy.

In region 2 the high energy peaks disappear smoothly (after P1 cross P0) and let behind an edge-like emission. Extrapolating the position of Edge 1, at higher energy, towards the low excitation region, we observe that it crosses the position of the fundamental mode just on the threshold. Edge 2, on the other hand, seems related with the disappearance of the high energy peaks and it shifts rapidly to the red until it merges with the low energy peaks group.

A further analysis inside this laser behavior has been done using the microcavity

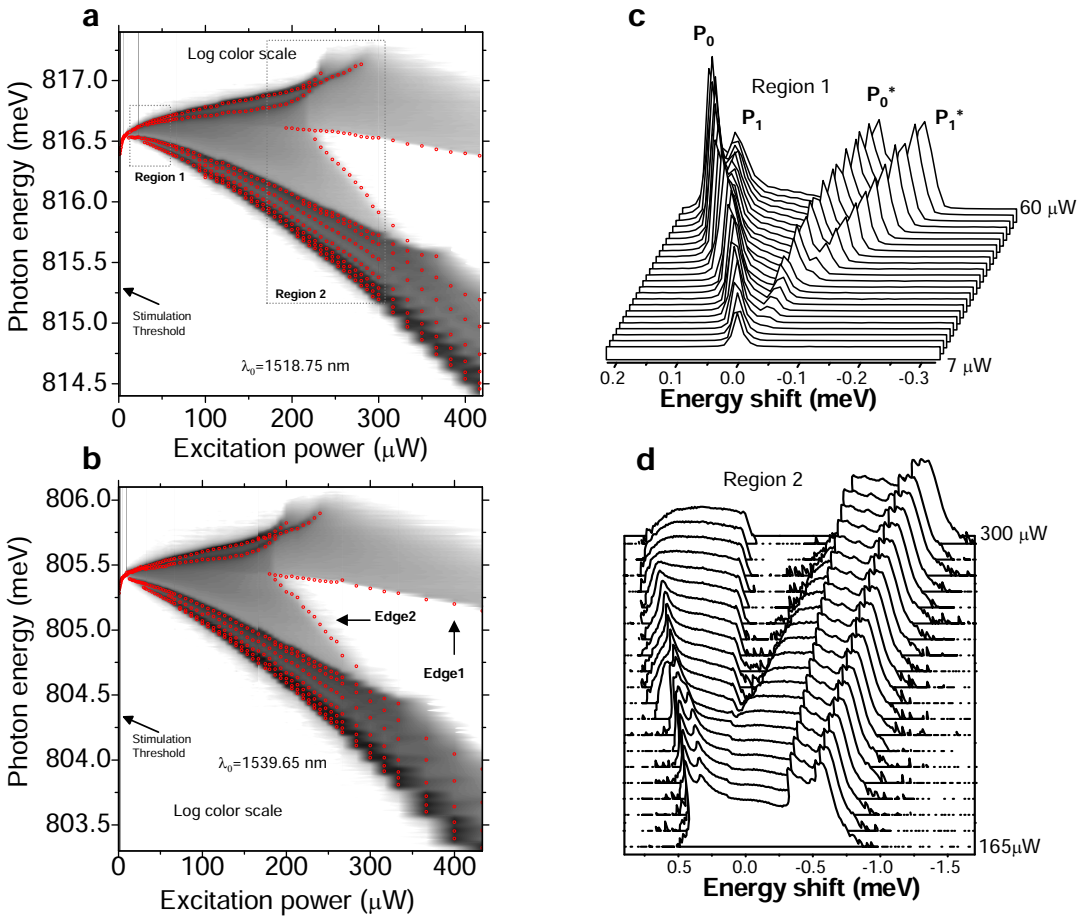

Figure 5.10: Contour plots in logarithmic scale showing the evolution of the emission spectra with the average excitation power. a) , b) two different PCMs. c), d) Detail plot of the region highlighted at a). Red dots indicate the position of the peaks/edges.

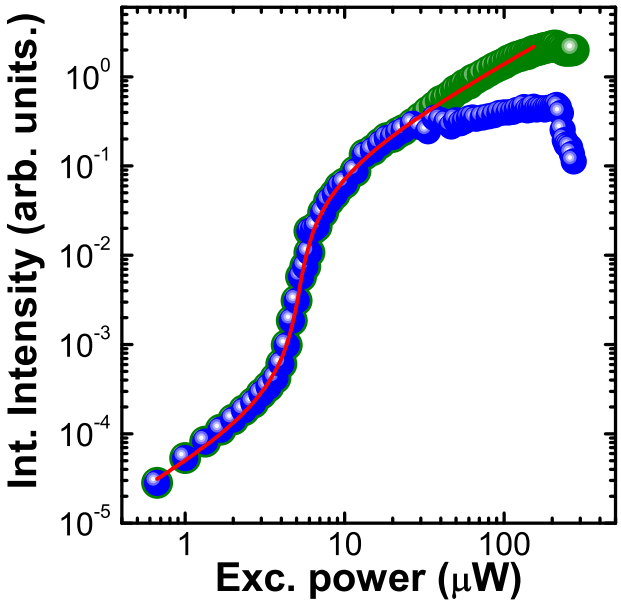

Figure 5.11: Log-log plot of the integrated PL emission intensity versus the average excitation pump power. Blue for the fundamental peak. Green dark dots for full spectrum peaks. Red line: Fitting curve.

laser equations. The microcavity laser equations used and the fitting procedure have been explained in the Section 5.1.3. In this case, the idea behind the use of the laser equations is to be able to compare the theoretical L-L curve with the measured one. We are more interested in the shape of the L-L curve rather than in the obtention of the precise values of the different parameters (β, ...), contrary to the case in Section 5.1.3. Fig. 5.11 shows two different L-L curves of the PCM emitting around 1518 nm, and the fitting using the microcavity laser equations (red color line). The first L-L curve (blue dots) is obtained integrating the first peak that appears in the emission spectra, (P0 in Fig. 5.10 c)). The second L-L curve (dark green dots) is obtained integrating all the peaks of the spectra. When the curve is fitted to the

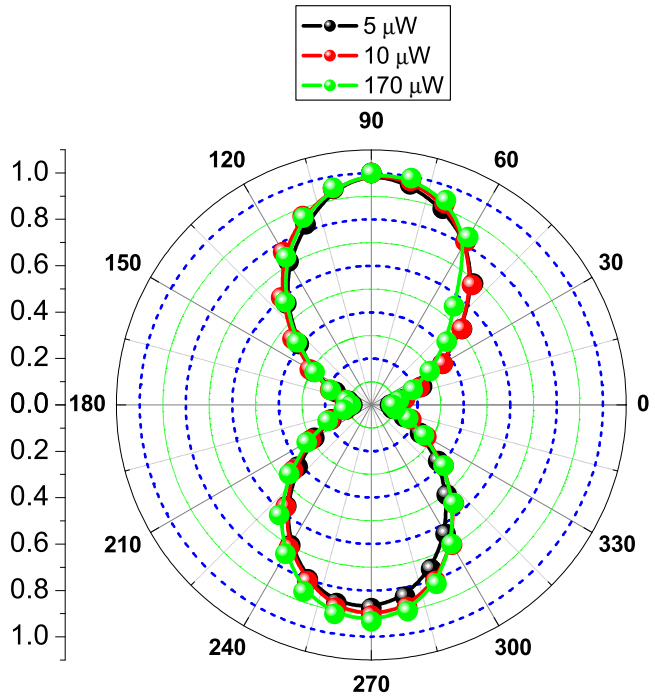

Figure 5.12: Integrated intensity for varying linear polarization angles and average excitation powers (cavity horizontal). Lines indicates a guide to the eye.

laser equations[i], the behavior of our system only can be adjusted considering all the spectrum peaks. This points out that all the spectrum is behavior like a (single mode) laser.

Finally, we have evaluated the far field polarization of the modes. Fig. 5.12 shows the polar diagram measured for three different excitation powers. The cavity mode was strongly linearly polarized perpendicular to the cavity defect independently of the excitation density and QWrs orientation. This is expected from symmetry properties of the electromagnetic mode field distribution (see, Section 5.1.2).

[i]The parameters used for the fitting are the same that in Section 5.1.3, including the β. In this case the variate parameters were the transparency current and the differential gain.

5.3 Summary

Room temperature laser emission at 1.5 μm using a single layer of self-assembled InAs/InP QWrs embedded in a L7 PCM with a Q$\simeq$55000 has been demonstrated. Under non resonant continuous wave optical pumping an effective power threshold of 22 μW has been measured. The characteristics of our laser as extracted from the analysis of the laser rate equations are in between QD and QW PCM lasers operated under similar conditions.

In the pump pulsed regime threshold values below 2 μW of effective excitation power have been measured. Below the threshold, the device shows lorentzian lineshape emission, whereas just above the threshold the lineshape becomes asymmetric towards lower energies. If the excitation power is increased the multipeaks appear on the spectra. Energy splittings in the meV and in the μeV ranges as the excitation power is increased have been measured. Altogether, the results draw a spectral scenario very different from the expected for a regular semiconductor photon laser.

Chapter 6

Fabrication of PCM on GaAs for quantum photonic devices

The fabrication process of photonic crystal microcavities on GaAs material is described. Different kinds of photonic crystal microcavities have been fabricated looking for suitable PCMs for quantum photonic devices. Coupling between the embedded quantum nanostructures and the cavity modes have been obtained. Single photon emission from a quantum ring embedded in the photonic crystal lattice has been demonstrated.

6.1 Motivation

There is a strong demand in the telecommunications market to use devices that can transmit information in a secure way using optical quantum cryptography. The possibility of using quantum states has been confirmed in the recent years, using "table-top" setups that include quantum photonic devices such single photon emitters (SPEs) [82]. One of the main goal is to obtain SPEs in the microscale, that can be integrated and packed like today's laser diodes used for telecom. A good approach consists of the use of semiconductor nanostructures, like a quantum dot (QD), in-

side of an optical cavity [187], like a photonic crystal microcavity (PCM). These nanostructures are grown by molecular beam epitaxy (MBE) on GaAs substrates, or more recently, on InP substrates. Due to this, it was necessary to development a fabrication process of photonic crystals (PCs) on GaAs material in order to obtain the semiconductor nanostructure (QD or quantum ring (QR)) coupled to a PCM mode. This chapter describes the work developed on the fabrication of PCs on GaAs material, and describes some results related to their performance as quantum light emitters.

6.2 Introduction

An increasingly important research field that involves the area of the semiconductor solid state physics and photonics is the field of the quantum information processing. The generation of single photon on demand and the ability to manipulate it is a key element of that field [188]. The generation of a single photon stream with indistinguishability, high repetition rate in high efficient sources is very important not only in quantum cryptography but also in quantum information processing [187]. In this context, since the demonstration of the MBE QDs as trigger single photon sources [189] an important effort has been done in order to improve their properties [190]. In this task the PCMs play an important role enabling the obtention of fast single photon sources, due to its low modal volume exhibiting a high Purcell effect with moderate values of the quality factor (Q), providing high degree of indistinguishability and high efficiency [191]. Moreover, the generation and transfer of single photons in a PC chip has been already demonstrated [32]. On the other hand, the ability to manipulate each photon individually and the availability of two-photon logical gates are required for the quantum information processing with photons [192]. Due to the low environment interaction of the photons, such elements require a non-linear medium with low losses. A strong non linear behavior is obtained close to the transition frequencies of an emitter, especially if the emitter is strong coupled to a microcavity mode [135]. In this context, the development of high Q microcavities with QDs embedded as non linear medium to obtain the strong coupling regime, is a mandatory task [15, 16]. Several functionalities have been demonstrated like the

transmission control in a PCM coupled to a single QD [135, 5] or the photon phase control at the single photon level [193]. Furthermore, a QD strongly coupled to the cavity modes of a PCM has been proposed as an efficient source of polarization entangled photons [194]. Finally, high Q PCM with a few QDs as active medium has been demonstrated as a high efficient and low threshold microlaser source [22], and single QD lasing in a PCM has been obtained [195]

Our approach is based in the use of QRs instead QDs. The QRs present several advantages over the QDs. The oscillator strength of the excitonic ground state of the QRs is three times higher than for QDs [196]. On the other hand, the QRs open new paths to study the magnetic field effects due to the shape of the nanostructure [197]. L3-kind [12] and Calzone-kind [198] PCMs have been fabricated in samples with a single layer of self-assembly In(Ga)As/GaAs QRs. Coupling between the QRs and the cavity modes has been obtained. Single photon emission from a QR embedded in the PC lattice has been demonstrated.

6.3 Design and fabrication

6.3.1 Epitaxial material

The design of the photonic device consists of a single layer of self-assembled In(Ga)As QRs grown by solid source MBE and embedded in a 158-nm-thick GaAs slab. An $Al_{0.7}Ga_{0.3}As$ layer of 500 nm thickness is used as sacrificial layer for the membrane realization.[a] Details about the epitaxial material growth can be found at Ref. [199]. However a briefly description concerning size and distribution is shown here, due to its relevance for the final device. Fig. 6.1 a)[b] shows an atomic force microscope (AFM) image of an uncapped layer of QRs. This layer was grown on the top of the wafer in the same conditions that the embedded in the middle of the slab in order to obtain the nanostructrures shape, size and density. The QRs density is $8{\times}10^9$ QR cm^{-2} ($\sim$80 QR μm^{-2}). AFM micrographs show a ring morphology with

[a] The epitaxial material was provided by Dr. D. Granados and Dr. J. M. García
[b] AFM image courtesy of A. G. Taboada

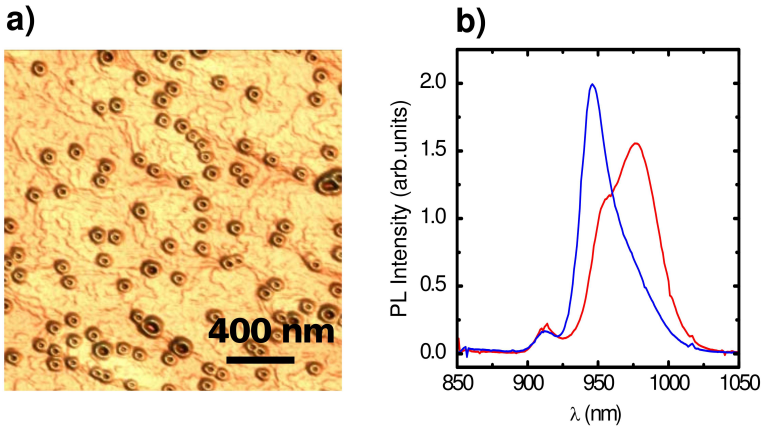

Figure 6.1: a) Atomic force microscope (AFM) image of an uncapped sample of self-assembled InAs/GaAs QRs. b) Photoluminescence spectrum of the quantum rings sample without photonic crystal structure.

an inner radius around 20 nm (measured from the bottom of the hole to the top of the ring) and an outer radius around 50 nm in the [1 $\overline{1}$ 0] direction. These values are 20% smaller in the [110] direction due to the bigger diffusion of In in the [1 $\overline{1}$ 0] direction. Cross sectional scanning tunnel microscopy (X-STM) images were recorded on QRs samples grown in the same conditions in the same MBE reactor. The images show a small In-rich asymmetric crater-like shaped core. They have smaller radius (10 nm) and larger height (2.5 nm) than the ring-shaped islands measured by AFM. Although the ring shape is not preserved after the capping process [200] the confinement potential preserves its ring character since Aharonov-Bohm related oscillation have been measured in magnetotorsion experiments [201]. Fig. 1.1 b)[c] shows photoluminescence (PL) emission spectra of the QRs sample at 20 K. The emission spectra spread from the 900 nm to 1020 nm where two size distributions of QRs are observed.

[c]Photoluminescence measurement courtesy of Dr. D. Granados.

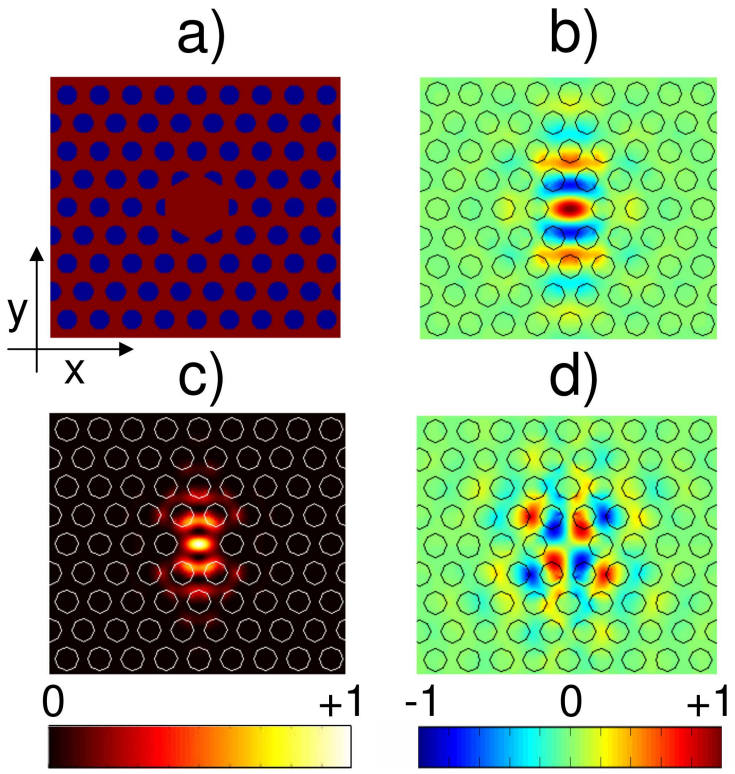

Figure 6.2: a) Sketch of calzone cavity. Normalized electric field patterns: b) E_x, d)E_y. c) Normalized E-field intensity.

6.3.2 Photonic crystal structure

The selected PC structure was the triangular lattice of air holes which presents a large photonic band gap (PGB) for the even modes ($\sigma_{xy} = +1$), also called TE-like modes. Two kinds of PCMs are created: the L3 cavity and the "calzone" cavity.

The L3-type cavity is created filling three holes along the ΓK direction of the triangular lattice[12]. The parameters selected for the structure were the lattice constant a=250 nm, the holes radius $r/a = 0.3$, and the slab thickness $d/a = 0.62$. This gives a low energy resonant mode for the L3 cavity at $\omega a/2\pi c \simeq 0.259$, with high Q $\sim$5700 and small modal volume $V \sim 0.6(\lambda/n)^3$. In addition, it is well frequency isolated from the higher order modes [178]. The simulation of the L3-PCM has been

performed by 3D-FDTD [109]. The fundamental mode has *"well-defined"* symmetry properties, i.e., the E_y field pattern is symmetric with respect to the XZ plane and the YZ plane and the E_x antisymmetric with respect to those symmetry planes (the L3 cavity lies in the X direction). These symmetry properties are the same than the fundamental mode of the L7 PCM (see Chap. 5). Taking into account that double symmetric (with respect to both X, Y axes) is required for the coupling to the exactly vertical scattering states of the field component and that doubly antisymmetric (with respect to both axes) produce the cancelation of the overlap between the confined states and scattering states, the field component considered is inhibited [178]. Then, the fundamental mode exhibits a far field polarization perpendicular to the longitudinal plane of the cavity. On the other hand, the cavity can be tuned in order to obtain very high Qs [12, 178]

The calzone cavity was created in the triangular PC lattice filling only one hole. The first closest line of holes is truncated and shifted (inwards/outwards) (see Fig. 6.2 a)) in order to improve the Q of the resonant modes. This cavity has two low energy modes which are energy degenerated and exhibit perpendicular polarization (as happens in the H1 PCMs [156]). In addiction, these modes present high (Q$\sim$ 25000) and small modal volume ($V \sim 0.5(\lambda/n)^3$) [198]. These characteristics make the cavity suitable for the obtention of polarization entangled photons [198, 194]. In our case, the parameters selected were: the lattice constant a=230 nm, the hole radius r/a=0.31, the slab thickness d/a=0.69, and the truncated holes are shifted inwards 14 nm. The resonant frequency of the fundamental modes $\omega a/2\pi$c=0.25. Fig. 6.2 shows the field profiles of one of the fundamental modes calculated by 3D-FDTD. In analogous way that in the case of the fundamental mode of the L3/L7 PCM, it has *"well-defined"* symmetry properties and hence the polarization. The other degenerated mode is ninety degrees rotated with respect to the previously shown one exhibiting perpendicular polarization.

6.3.3 Fabrication

In our path to the fabrication of PCMs on GaAs two processes have been used. The first one uses a SiO_x hard mask and combined reactive ion beam etching (RIBE)

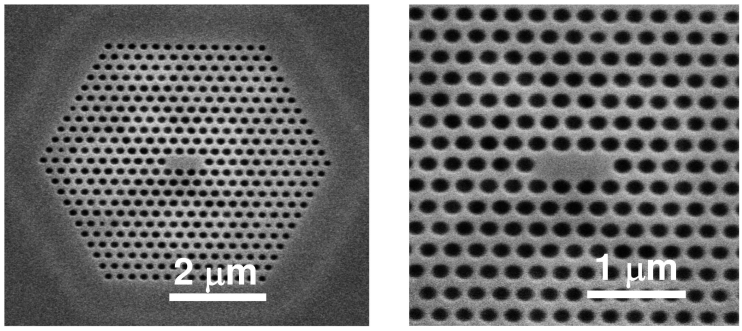

Figure 6.3: Scanning electron microscope image of the fabricated L3-type photonic crystal microcavity. Left: Complete PC structure. Right: Detail of the center of the structure.

and reactive ion etching (RIE)[d]. The second one uses only one mask, e-beam resist ZEP-520A, and inductive coupled plasma (ICP) etching for transferring the pattern directly from the resist to the semiconductor material.

Process with SiO_x hard mask

A 200 nm-thick SiO_x layer was deposited by plasma enhanced chemical vapor deposition (PECVD) on top of the GaAs epitaxial material. The sample was spin-coated with PMMA-A4 resist at 5000 rpms during 30 s, and baked in an oven at 170 °C for 70 mins. The PCMs were fabricated by e-beam lithography at an acceleration voltage of 25 kV, where the cavity defect is surrounded by eleven holes. At this time the NanoPECS module was not available in our e-beam lithography system. In order to reduce the proximity effect, low beam currents were used ($\sim$ 5 pA), giving a long e-beam time for the patterning. After development (see condition Chap. 2) the pattern is transferred to the SiO_x hard mask by RIBE. The chamber pressure was kept at a base pressure of $\sim 2 \times 10^{-7}$ Torr. Flows of 5.6 SCCM of CHF_3 and 4 SCCM of N_2 were injected, yielding a chamber pressure of $\sim 3 \times 10^{-4}$ Torr. A beam voltage of 250 V and an accelerating voltage of -450 V were selected for the etching process. The sample steel plate was not refrigerated and was rotating during all the etch process. The PMMA-A4 remanent resist was eliminated by hot

[d]Several trials with the ion-milling (RIBE with Ar gas) for etching the GaAs material were done. Holes with strong conicity and surface roughness were obtained and the process was rejected.

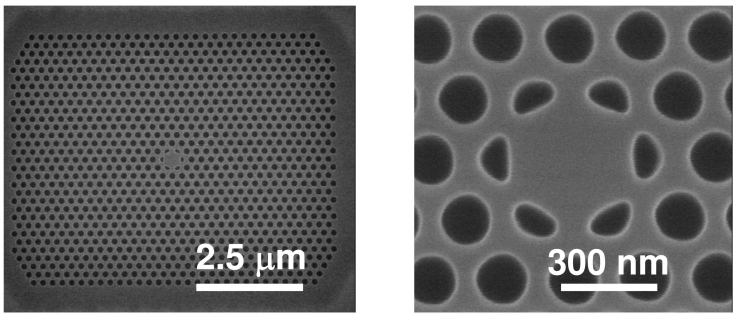

Figure 6.4: Scanning electron microscope image of the fabricated Calzone-type photonic crystal microcavity. Left: Complete PC structure. Right: Detail of the center of the structure.

acetone and oxygen plasma (see conditions Chap. 2). The transferring of the hard mask to the GaAs material was done by RIE[e] using $SiCl_4$ and Ar gas mixture. The parameters optimized for the etching were: a flow of $SiCl_4$ of 8.2 SCCM, a flow of Ar of 2.2 SCCM and a coil power of 150 W. The chamber pressure was kept at the lowest value in order to maintain a stable plasma discharge. Finally, in order to obtain the PC membrane the sample was submerged in hydrofluoric acid water diluted $HF(1) : H_2O(5)$ and time controlled (∼30 s). It is important to note that the etching speed is very sensitive to the aluminium fraction (x) of the $Al_xGa_{1-x}As$ sacrificial layer. Fig. 6.3 shows an SEM image of a fabricated PC membrane. The L3 PCMs, which spectra will be shown, have been fabricated by this method.

Process without SiO_x hard mask[f]

A way to simplify the fabrication process is to overcome the hard mask step on the fabrication process. This method has been applied in different research groups [202, 203]. The PMMA-A4 resist is replaced by ZEP-520A resist which has been proved to be more resistent than PMMA-A4 in the RIE etching process [204]. The pattern is transferred from the resist to the GaAs material in only one step. The sample was spin coated with ZEP-520A resist at 3000 rpm during 30 s in order to obtain a

[e]At this time there was not RIE machine at the IMM. The etching was performed at the Instituto de Sistemas Optoelectrónicos y Microtecnología (ISOM-UPM), Universidad Politécnica de Madrid.

[f]The approach to this fabrication process was done at the laboratory of Prof. E. L. Hu at UCSB

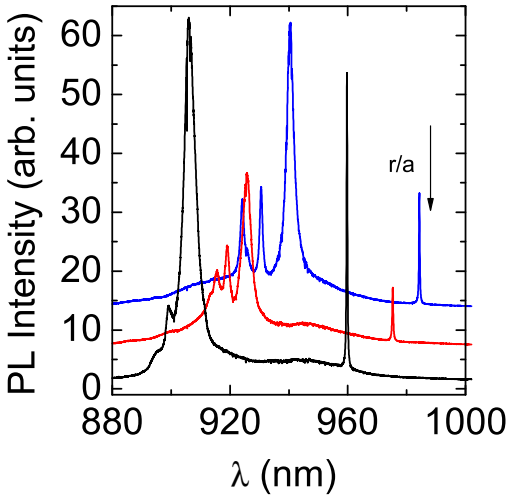

Figure 6.5: Spectra measured for three L3-PCM microcavities fabricated with different value of the radii.

resist thickness of 420 nm. The baking of the resist was performed at 175 °C for 150 s in a hotplate. An acceleration voltage of 100 kV and an e-beam current of 100 pA were used for the resist exposure. At this acceleration voltage the proximity effect is negligible and no proximity correction is necessary. After the e-beam exposure the sample was developed by submersion during 60 s in N-Amyl-acetate, 10 s Methyl isobutyl ketone (MIBK) and 10 s on Isopropanol. ICP etching was performed using a three gases mixture maintaining the chamber pressure at 2.6 mTorr. The conditions of the process were: a flow of Cl_2 of 3 SCCM, a flow of BCl_3 5.6 SCCM and a flow of Ar 12 SCCM. The ICP-power used was 600 W and the DC bias 80W[g]. The time of the etching process was 150 s. The remanet of resist was removed by means of UV exposure and remover 1156. Finally, the PC membrane was obtained by submerging the sample in a hydrofluoric acid water diluted $HF(1) : H_2O(5)$ and time controlled (∼30 s). Fig. 6.3 shown an image of a fabricated membrane and one of the sample after the dry etching. The calzone PCMs were fabricated by this method.

[g]The ICP system used does not measure the bias voltage.

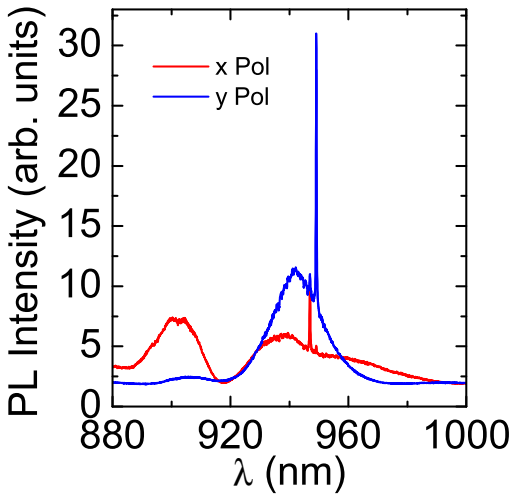

Figure 6.6: Polarization resolved spectra measured for a Calzone cavity. Red line polarizer axis along the X direction. Blue line polarizer axis along the Y direction.

6.4 Optical characterization

The optical characterization[h] was performed by microphotoluminescence (μ-PL) spectroscopy at low temperature in the range ($\sim$ 10 K - 100 K) in a continuous flow helium cryostat. The structures were continuous wave (CW) optically pumped with a HeNe laser or Ti-saphire laser. An objective lens is used to focus the excitation spot (diameter $\sim$ 2-3 μm) over the sample. The emitted light was collected by the same objective lens and focused in a double spectrometer. A cooled CCD was used as detector.

Figure 6.5[i] shows the measured emission spectra of a L3 PCM microcavity where the r/a ratio has been changed. A decrease of the wavelength of emission is observed as the filling factor is increased, due to the shift of the PCM modes towards high

[h]The optical measurement shown in this section has been performed at the Prof. José Manuel Calleja laboratory in the UAM.

[i]Spectral measurements performed by Dr. H. Van der Meulen and Dr. D. Sarkar from Universidad Autónoma de Madrid.

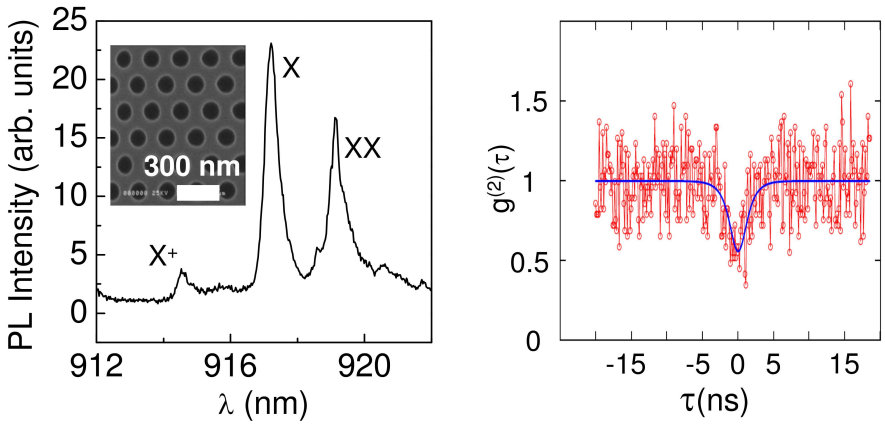

Figure 6.7: Left: Spectrum measured from an isolated QR immerse in the PC lattice area. Righ: Autocorrelation function measured for the excitonic transition of the QR.

energies. The fundamental and higher energy modes are observed in the spectra. Q values as high as 3300 have been measured for the fundamental mode[113]. This value is close to the best values published for L3 PCM [178]. Fig. 6.6[j] shows the polarization resolved spectra of one of the calzone cavities fabricated. The two low energy modes show an energy splitting due to the fabrication imperfections. This is the common case of the degenerated cavity modes [205]. On the other hand, when the intensity of emission of one mode is maximized by adjusting the polarization angle the other mode shows a minimum of intensity. Changing the polarization ninety degrees the same behavior is observed with the modes changed. This points out that both modes have perpendicular polarizations as expected from the near field cavity mode calculations.

One way to obtain a single photon emitter from an InAs/GaAs QRs in a high density sample is to use a PC lattice. In that case the PC lattice has two functions. The first one is to isolate a single QR drilling the semiconductor material. In a sample with high density of QRs there is a very low probability to find an isolated semiconductor nanostructure. Also the nanostructure has to be coupled to a cavity mode which decreases the probability even more. The second one is to enhance the extraction

[j]Spectral measurements performed by E. Gallardo from Universidad Autónoma de Madrid.

efficiency through the redistribution of the spontaneous emission inside the photonic band gap [11]. Using a triangular PC lattice (see inset Fig. 6.7 left) the emission of a single QRs isolated in the triangular lattice has been measured. The parameters of the lattice are: a=226 nm and r=65 nm, giving a separation between the air hole surfaces of 96 nm. Fig. 6.7[k] left shows the emission spectrum of the QRs isolated in the PC lattice for an excitation power of 10 μW. The excitonic and biexcitonic transitions have been identified through the emission intensity dependence with the excitation power [189]: linear behavior for the exciton transition and quadratic dependence for the biexciton [206]. Fig. 6.7^k right shows the autocorrelation function of the excitonic transition measured in a Hanbury Brown and Twiss (HBT) set-up. A description of a HBT set-up can be found at Ref. [190]. The measured value of the $g^2(0)$ $\simeq$0.5. After the background correction and the deconvolution with the temporal response of the detectors a value of $g^2(0)$=0.34 is obtained [206]. This value of $g^2(0)$ <0.5 is indicative of single photon emission.

6.5 Summary

PCMs have been fabricated on GaAs material with a single layer of InAs/GaAs quantum rings. A fabrication process combining RIBE and RIE has been developed. Coupling between the cavity modes and the quantum rings has been demonstrated. A fabrication process without hard mask has been used to fabricate PC structures. Single photon emission from a QR embedded in the PC lattice has been measured.

[k]Spectral measurements performed by E. Gallardo and A. Nowak from Universidad Autónoma de Madrid.

Chapter 7

Conclusions

The results obtained in this Thesis can be summarized as follows:

1. An enhancement of the intensity of emission between 4 and 7 times (1.9 times at k=0 point) has been measured for the "flat band" of the Suzuki-phase lattice on top of a bottom Bragg reflector. This new photonic structure provides a photonic band configuration that includes the TM-like modes due to the breaking of the mirror symmetry.

2. Laser emission with high quality factor (Q$\simeq$12000) has been measured on a wide area PC structures with vertical emission using the hybrid triangular-graphite PC lattice. This structure provides a new mechanism of formation of Bloch modes with high Qs around the Γ-point.

3. Laser emission (continuous wave) has been obtained on L7 photonic crystal microcavities (PCMs) with a single layer of self-assembly InAs/InP quantum wires (QWrs). Qs as high as $\simeq$ 55000 have been measured in structures with intrinsic Q=70000. It has been demonstrated that the spatial alignment between the QWrs an the cavity plays an important role. The behavior under pulsed excitations shows asymmetric lineshapes and peak splittings in the meV and in the μeV ranges as the excitation power is increased.

4. PCMs with In(Ga)As/GaAs quantum rings embedded have been designed and fabricated; the emission of the PC lattice has shown single photon emission.

This process opens ways to future work on solid state quantum information and quantum computing technology.

Appendix A

High Q PCM based in a Γ-point of the hybrid lattice

The third photonic band of the hybrid triangular-graphite lattice presents a high quality factor (Q) for a large range of in-plane ($k_{||}$) vectors around the Γ-point, which can overcome the vertical optical losses in a finite size structure. Using this advantage a defect is created in the lattice in order to obtain a high Q photonic crystal microcavity (PCM) mode based on a Γ-point (above the light line). This kind of optical confinement was proposed by L. Ferrier *et al.* for obtaining high Q slow-Bloch modes above the light line in the square lattice of dielectric rods embedded in air [137, 81].

The third Γ-point of the hybrid triangular-graphite lattice is selected for this purpose. A slight increase of the filling factor of the lattice yields an increase of the energy of the photonic band (see Fig. A.1, red color[a]). As this structure is surrounded by the same PC structure with a slightly smaller filling factor (lower energy band position, see Fig. A.1, blue color) the lateral photon escape is inhibited inducing a photonic-well confinement [154, 137]. This, added to the high vertical Q of the hybrid lattice for a large $k_{||}$ range, makes that a high Q for the PCM mode can

[a]It is important to note that it is a two-dimensional simulation. The photonic bands are red-shifted when a three-dimensional calculation is performed.

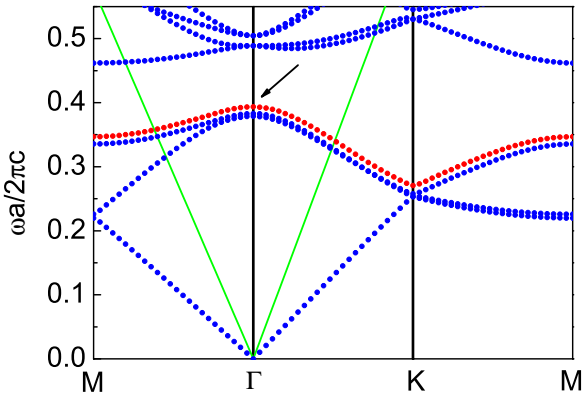

Figure A.1: Two dimensional photonic band structure of the triangular-graphite hybrid lattice on InP material (ϵ=10.1), where only even modes ($\sigma_{xy} = +1$) are showed. Blue color: surrounding PC-lattice, $R_g/a = 0.162$, $R_t/a = 0.14$. Red color: core lattice, $R_g/a = 0.18$, $R_t/a = 0.16$. Only the third band is plotted.

be expected. The parameters of the selected structure for the hybrid triangular-graphite lattice (surrounded PC-lattice) were $R_g/a = 0.162$, $R_t/a = 0.14$, a=780 nm, with a slab thickness $t = 237$ nm (air-bridge), and $\epsilon = 10.1$ (InP material). In order to create the defect in the structure the slight increment of the filling factor of the lattice was done at the center of the structure using the radii values of $R_g/a = 0.18$ and $R_t/a = 0.16$ in the "$H1$" central cell and the first closest adjacent cells. The hexagon of R_t holes (lateral size $2a$), that are the border of the cavity (see Fig. A.2), were fixed to $R_t/a = 0.15$ since a slight and continuous change in the hole radius decreases the optical losses [207, 68]. The lateral size of all the structure was fixed to 15μm$\times$ 15μm to minimize the in-plane losses. A 3D-FDTD simulation (Lumerical code [109]) of the structure was performed using symmetric conditions in order to reduce the computing requirements. A rectangular mesh (x, y, z) was used for the 3D-FDTD simulation with a meshing step of $dx = a/15\sqrt{3}$, $dy = 2a/45$, and $dz = t/10$. Fig. A.2 shows both the normalized H_z field and the electric field intensity $|E|^2$ profiles of the PCM cavity mode. The frequency of the mode is $\omega a/2\pi c$=0.479, with a $Q \simeq 148000$, $V \simeq 2.7(\lambda/n)^3$, and a $n_{eff} \simeq 2.7$, which

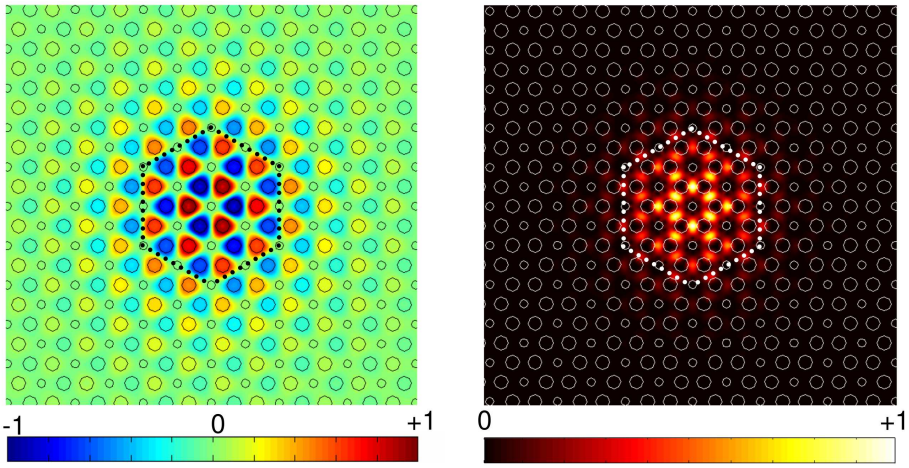

Figure A.2: Left: Normalized profile of the magnetic Hz component. Right: Normalized E-field intensity. Doted lines represents the cavity border.

provides a potential Purcell effect of $F = 4100$. The far-field pattern has been calculated using the tool provided for the Lumerical package. From this data, a coarse estimation of the fraction of photons that can be collected in a small vertical angle can be done. In agrement with to this, it is obtained that a $\sim 30\%$ fraction of the emitted light is collected in a $\pm 15^{\circ}$ angular range.

Further optimization of the PCM has to be done in order to increase the directionality of the emission that will increase the fraction of photons in the smallest collection angle possible, for example by tuning the slab bottom air-gap [41].

Appendix B

List of publications

PUBLISHED / IN PRESS (FIRST AUTHOR)

[5] **L. J. Martínez**, B. Alén, I. Prieto , J. F. Galisteo-López, M. Galli, L. C. Andreani, Ch. Seassal, P. Viktorovitch, and P. A. Postigo, "Two-dimensional surface emitting photonic crystal laser with hybrid triangular-graphite structure," **Opt. Express 17**, 15043-15051 (2009).

[4] **L. J. Martínez**, B. Alén, I. Prieto, D. Fuster, L. González, Y. González, M. L. Dotor, and P. A. Postigo, "Room temperature continuous wave operation in a photonic crystal microcavity laser with a single layer of InAs/InP self-assembled quantum wires," **Opt. Express 17**, 14993-15000 (2009).

[3] **L. J. Martínez**, I. Prieto, B. Alén, and P. A. Postigo, "Fabrication of high quality factor photonic crystal microcavities in InAsP/InP membranes combining reactive ion beam etching and reactive ion etching," **J. Vac. Tech. B 27**, 1801-1804 (2009).

Selected for: *Virtual Journal of Nanoscale Science & Technology, July, 6, (2009).*

[2] **L. J. Martínez**, A. R. Alija, P. A. Postigo, J. F. Galisteo-López, M. Galli, L. C. Andreani, Ch. Seassal, and P. Viktorovitch, "Effect of implementation of a Bragg reflector in the photonic band structure of the Suzuki-phase photonic crystal

lattice," **Opt. Express 16**, 8509-8518 (2008).

[1] **L. J. Martínez**, A. García-Martín, and P. A. Postigo, "Photonic band gaps in a two-dimensional hybrid triangular-graphite lattice," **Opt. Express 12**, 5684-5689 (2004).

PUBLISHED / IN PRESS (CO-AUTHOR)

[6] I. Prieto, B. Galiana, P. A. Postigo, C. Algora, **L. J. Martínez**, and I. Rey-Stolle, "Enhanced quantum efficiency of Ge solar cells by a two-dimensional photonic crystal nanostructured surface," **Appl. Phys. Lett. 94**, 191102 (2009).

[5] D. Sarkar, **L. J. Martínez**, I. Prieto-González, H. P. van der Muelen, J. M. Calleja, D. Granados, A. G. Taboada, J. M. García, A. R. Alija, and P. A. Postigo. "Optical emission of InAs/GaAs quantum rings couple to a two-dimensional photonic crystal microcavity," **Physica E: Low-dimensional Systems and Nanostructures**, 40, (6) 2156 (2008).

[4] P. A. Postigo, A. R. Alija, **L. J. Martínez**, M. L. Dotor, D. Golmayo, , J. Sánchez-Dehesa, C. Seassal, P. Viktorovitch, , M. Galli, A. Politi, M. Patrini, and L. C. Andreani, "Laser nanosources based on planar photonic crystals as new platforms for nanophotonic devices," **Photon. Nanostruct.: Fundam. Applic., 5**, 79-85, (2007).

[3] A. R. Alija, **L. J. Martínez**, P. A. Postigo, J. Sánchez-Dehesa, M. Galli, A. Politi, M. Patrini, L. C. Andreani, C. Seassal, and P. Viktorovitch, "Theoretical and experimental study of the Suzuki-phase photonic crystal lattice by angle-resolved photoluminescence spectroscopy," **Opt. Express 15**, 704-713 (2007).

Selected for: *Virtual Journal of Nanoscale Science & Technology, March, 5, (2007).*

[2] A. R. Alija, **L. J. Martínez**, P. A. Postigo, C. Seassal, and P. Viktorovitch, "Coupled-cavity two-dimensional photonic crystal waveguide ring laser," **Appl. Phys. Lett. 89**, 101102 (2006).

Selected for: *Virtual Journal of Nanoscale Science & Technology, September, 18, (2006).*

[1] A. R. Alija, **L. J. Martínez**, A. García-Martín, M. L. Dotor, D. Golmayo, and P. A Postigo, "Tuning of spontaneous emission of two-dimensional photonic crystal microcavities by accurate control of slab thickness," **Appl. Phys. Lett. 86**, 141101 (2005).

Selected for: *Virtual Journal of Nanoscale Science & Technology, April, 11, (2005).*

MANUSCRIPTS IN REVISION

[2] E. Gallardo, **L. J. Martínez**, A. K. Nowak, H.P. van der Meulen, J. M. Calleja, C. Tejedor, I. Prieto, D. Granados, A. G. Taboada, J.M. García, and P.A. Postigo, "Microcavity-mediated Coupling of Two Distant Semiconductor Qubits, " Submitted (2009). `http://arxiv.org/abs/0908.1161`

[1] E. Gallardo, **L. J. Martínez**, A. K. Nowak, D. Sarkar, D. Sanvitto, H. P. van der Meulen, J. M. Calleja, I. Prieto, D. Granados, A. G. Taboada, J. M. García, and P. A. Postigo, "Single photon emission by semiconductor quantum rings in a photonic crystal, " Submitted to **Opt. Lett.** (2009).

CONFERENCE PROCEEDINGS

[2] **L. J. Martínez**, A. R. Alija C. Seassal, P. Viktorovitch and P. A. Postigo., "Modal suppression and single-mode emission in photonic crystal coupled-cavity ring-like lasers," **Electron Devices, 2007 Spanish Conference on**, 266-269 (2007). `http://dx.doi.org/10.1109/SCED.2007.384043`

[1] **L. J. Martínez**, A. García-Martín, and P. A. Postigo, "Coupling between waveguides and cavities in 2D photonic crystals: the role of symmetry mode," **Proceedings of the SPIE**, 5840, 879-884 (2005). `http://dx.doi.org/10.1117/12.637306`

Appendix C

List of Abbreviations

- **AFM** Atomic Force Microscope
- **ARP** Angle-Resolved Photoluminescence
- **CW** Continuous Wave
- **FDTD** Finite-Differences Time-Domain
- **MBE** Molecular Beam Epitaxy
- **PB** Photonic Band
- **PBG** Photonic Band Gap
- **PC** Photonic Crystal
- **PCM** Photonic Crystal Microcavity
- **PCW** Photonic Crystal Waveguide
- **PECVD** Plasma Enhanced Chemical-Vapor Deposition
- **PL** PhotoLuminescence
- **PMMA** PolyMethyMethacrylateAnisole

- **PR-ARP** Polarization-Resolved Angle-Resolved Photoluminescence
- **Q** Quality factor
- **QD** Quantum Dot
- **QED** Quantum ElectroDynamics
- **QR** Quantum Ring
- **QW** Quantum Well
- **QWr** Quantum Wire
- **RIBE** Reactive Ion Beam Etching
- **RIE** Reactive Ion Etching
- **RMS** Root Mean Square
- **RT** Room Temperature
- **SEM** Scanning Electron Microscopy
- **TE** Transversal Electric
- **TM** Transversal Magnetic
- **V** Modal Volume
- **VCSEL** Vertical-Cavity Surface-Emitting Laser

Bibliography

[1] D. Gevaux, "Slow light, fast computers," *Nature Photonics* **1**, 72 (2006).

[2] S. John, "Light control at will," *Nature* **460**, 337 (2009).

[3] S. Noda, "Recent progresses and future prospects of two- and three-dimensional photonic crystals," *J. Lightw. Technol.* **24**, 4554–4567 (2006).

[4] J. Bravo-Abad and M. Soljačić, "Photonic crystals go dynamic," *Nature Materials* **6**, 799 – 800 (2007).

[5] A. Faraon, I. Fushman, D. Englund, N. Stoltz, P. Petroff, and J. Vučković, "Dipole induced transparency inwaveguide coupled photonic crystal cavities," *Opt. Express* **16**, 12154–12162 (2008).

[6] Y.-F. Xiao, J. Gao, X.-B. Zou, J. F. McMillan, X. Yang, Y.-L. Chen, Z.-F. Han, G.-C. Guo, and C. W. Wong, "Coupled quantum electrodynamics in photonic crystal cavities towards controlled phase gate operations," *New J. Phys.* **10**, 123013 (13pp) (2008).

[7] E. Yablonovitch, "Inhibited spontaneous emission in solid-state physics and electronics," *Phys. Rev. Lett.* **58**, 2059–2062 (1987).

[8] S. John, "Strong localization of photons in certain disordered dielectric superlattices," *Phys. Rev. Lett.* **58**, 2486–2489 (1987).

[9] E. Yablonovitch, "Photonic crystals: What's in a name?" *Optic & Photonics News* **18**, 12–13 (2007).

[10] S. Ogawa, M. Imada, S. Yoshimoto, M. Okano, and S. Noda, "Control of light emission by 3D photonic crystals," *Science* **305**, 227–229 (2004).

[11] M. Fujita, S. Takahashi, Y. Tanaka, T. Asano, and S. Noda, "Simultaneous inhibition and redistribution of spontaneous light emission in photonic crystals," *Science* **308**, 1296–1298 (2005).

[12] Y. Akahane, T. Asano, B. S. Song, and S. Noda, "High-Q photonic nanocavity in a two-dimensional photonic crystal," *Nature* **425**, 944–947 (2003).

[13] S. Kawashima, M. Okano, M. Imada, and S. Noda, "Design of compound-defect waveguides in three-dimensional photonic crystals," *Opt. Express* **14**, 6303–6307 (2006).

[14] A. Badolato, K. Hennessy, M. Atature, J. Dreiser, E. Hu, P. M. Petroff, and A. Imamoglu, "Deterministic Coupling of Single Quantum Dots to Single Nanocavity Modes," *Science* **308**, 1158–1161 (2005).

[15] T. Yoshie, A. Scherer, J. Hendrickson, G. Khitrova, H. M. Gibbs, G. Rupper, C. Ell, O. B. Shchekin, and D. G. Deppe, "Vacuum rabi splitting with a single quantum dot in a photonic crystal nanocavity," *Nature* **432**, 200–203 (2004).

[16] K. Hennessy, A. Badolato, M. Winger, D. Gerace, M. Atature, S. Gulde, S. Falt, E. L. Hu, , and A. Imamoğlu, "Quantum nature of a strongly coupled single quantum dot-cavity system," *Nature* **445**, 896–899 (2007).

[17] A. Laucht, F. Hofbauer, N. Hauke, J. Angele, S. Stobbe, M. Kaniber, G. Bohm, P. Lodahl, M.-C. Amann, and J. J. Finley, "Electrical control of spontaneous emission and strong coupling for a single quantum dot," *New J. Phys.* **11**, 023034 (11pp) (2009).

[18] D. Englund, D. Fattal, E. Waks, G. Solomon, B. Zhang, T. Nakaoka, Y. Arakawa, Y. Yamamoto, and J. Vučković, "Controlling the spontaneous emission rate of single quantum dots in a two-dimensional photonic crystal," *Phys. Rev. Lett.* **95**, 013904 (2005).

[19] M. Kaniber, A. Neumann, A. Laucht, M. F. Huck, M. Bichler, M.-C. Amann, and J. J. Finley, "Efficient and selective cavity-resonant excitation for single photon generation," *New J. Phys.* **11**, 013031 (9pp) (2009).

[20] O. Painter, R. K. Lee, A. Scherer, A. Yariv, J. O'Brien, P. Dapkus, and I. Kim, "Two-dimensional photonic band-gap defect mode laser," *Science* **284**, 1819–1821 (1999).

[21] H.-G. Park, S.-H. Kim, S.-H. Kwon, Y.-G. Ju, J.-K. Yang, J.-H. Baek, S.-B. Kim, and Y.-H. Lee, "Electrically Driven Single-Cell Photonic Crystal Laser," *Science* **305**, 1444–1447 (2004).

[22] S. Strauf, K. Hennessy, M. T. Rakher, Y.-S. Choi, A. Badolato, L. C. Andreani, E. L. Hu, P. M. Petroff, and D. Bouwmeester, "Self-tuned quantum dot gain in photonic crystal lasers," *Phys. Rev. Lett.* **96**, 127404 (2006).

[23] D. Englund, H. Altug, B. Ellis, and J. Vučković, "Ultrafast photonic crystal lasers," *Laser & Photonics Review* **2**, 264–274 (2008).

[24] J. D. Joannopoulos, P. R. Villeneuve, and S. Fan, "Photonic crystals: Putting a new twist on light," *Nature* **386**, 143–149 (1997). Erratum: ibid. vol. 387, p. 830 (1997).

[25] A. Chutinan and S. John, "Diffractionless flow of light in two- and three-dimensional photonic band gap heterostructures: Theory, design rules, and simulations," *Phys. Rev. E* **71**, 026605 (2005).

[26] D. M. Beggs, T. P. White, L. O'Faolain, and T. F. Krauss, "Ultracompact and low-power optical switch based on silicon photonic crystals," *Opt. Lett.* **33**, 147–149 (2008).

[27] T. Baba, "Photonic crystals: Remember the light," *Nature Photonics* **1**, 11–12 (2006).

[28] S. Noda, A. Chutinan, and M. Imada, "Trapping and emission of photons by a single defect in a photonic bandgap structure," *Nature* **407**, 608–610 (2000).

[29] C. R. Otey, M. L. Povinelli, and S. Fan, "Capturing light pulses into a pair of coupled photonic crystal cavities," *Appl. Phys. Lett.* **94**, 231109 (2009).

[30] Y. Tanaka, J. Upham, T. Nagashima, T. Sugiya, T. Asano, and S. Noda, "Dynamic control of the Q factor in a photonic crystal nanocavity," *Nature Materials* **6**, 862–865 (2007).

[31] K. Nozaki, H. Watanabe, and T. Baba, "Photonic crystal nanolaser monolithically integrated with passive waveguide for effective light extraction," *Appl. Phys. Lett.* **92**, 021108 (2008).

[32] D. Englund, A. Faraon, B. Zhang, Y. Yamamoto, and J. Vučković, "Generation and transfer of single photons on a photonic crystal chip," *Opt. Express* **15**, 5550–5558 (2007).

[33] M. Imada, A. Chutinan, S. Noda, and M. Mochizuki, "Multidirectionally distributed feedback photonic crystal lasers," *Phys. Rev. B* **65**, 195306 (2002).

[34] C. Monat, C. Seassal, X. Letartre, P. Regreny, P. Rojo-Romeo, P. Viktorovitch, M. L. V. d'Yerville, D. Cassagne, J. P. Albert, E. Jalaguier, S. Pocas, and B. Aspar, "InP-based two-dimensional photonic crystal on silicon: In-plane bloch mode laser," *Appl. Phys. Lett.* **81**, 5102–5104 (2002).

[35] H.-Y. Ryu, S.-H. Kwon, Y.-J. Lee, Y.-H. Lee, and J.-S. Kim, "Very-low-threshold photonic band-edge lasers from free-standing triangular photonic crystal slabs," *Appl. Phys. Lett.* **80**, 3476–3478 (2002).

[36] J. Mouette, C. Seassal, X. Letartre, P. Rojo-Romeo, J.-L. Leclereq, P. Regreny, P. Viktorovitch, E. Jalaguier, R. Perreau, and H. Moriceau, "Very low threshold vertical emitting laser operation in InP graphite photonic crystal slab on silicon," *Electron. Lett.* **39**, 526–528 (2003).

[37] E. Miyai, K. Sakai, T. Okano, W. Kunishi, D. Ohnishi, and S. Noda, "Lasers producing tailored beams," *Nature* **441**, 946–946 (2006).

[38] J. J. Wierer, A. David, and M. M. Megens, "III-nitride photonic-crystal light-emitting diodes with high extraction efficiency," *Nature Photonics* **3**, 163–169 (2009).

[39] B. Benbakir, C. Seassal, X. Letartre, P. Viktorovitch, M. Zussy, L. D. Cioccio, and J. M. Fedeli, "Surface-emitting microlaser combining two-dimensional photonic crystal membrane and vertical bragg mirror," *Appl. Phys. Lett.* **88**, 081113 (2006).

[40] H. Hattori, X. Letartre, C. Seassal, P. Rojo-Romeo, J. Leclercq, and P. Viktorovitch, "Analysis of hybrid photonic crystal vertical cavity surface emitting lasers," *Opt. Express* **11**, 1799–1808 (2003).

[41] S.-H. Kim, S.-K. Kim, and Y.-H. Lee, "Vertical beaming of wavelength-scale photonic crystal resonators," *Phys. Rev. B* **73**, 235117 (2006).

[42] S. Boutami, B. Benbakir, J.-L. Leclercq, and P. Viktorovitch, "Compact and polarization controlled 1.55 μm vertical-cavity surface-emitting laser using single-layer photonic crystal mirror," *Appl. Phys. Lett.* **91**, 071105 (2007).

[43] S. Boutami, B. Benbakir, X. Letartre, J. L. Leclercq, P. Regreny, and P. Viktorovitch, "Ultimate vertical fabry-perot cavity based on single-layer photonic crystal mirrors," *Opt. Express* **15**, 12443–12449 (2007).

[44] S. Noda, "Seekeing the ultimate nanolaser," *Science* **314**, 260–261 (2006).

[45] G. Kocher, W. Khunsin, S. Romanov, K. Vynck, S. Arpiainen, B. Lange, J. Ye, F. Jonsson, D. Cassagne, R. Zentel, J. Ahopelto, and C. Sotomayor Torres, "2D photonic defect layers in 3D inverted opals on Si platforms," in "*Transparent Optical Networks, 2006 International Conference on*," vol. 2 68–72 (2006).

[46] J. D. Joannopoulos, S. G. Johnson, J. N. Winn, and R. D. Meade, *Photonic Crystals: Molding the Flow of Light* (Princeton University Press, Singapore, 2008), 2nd ed.

[47] N. W. Ashcroft and N. D. Mermin, *Solid State Physics* (Brooks Cole, 1976), 1st ed.

[48] K. M. Ho, C. T. Chan, and C. M. Soukoulis, "Existence of a photonic gap in periodic dielectric structures," *Phys. Rev. Lett.* **65**, 3152–3155 (1990).

[49] Y. A. Vlasov, X.-Z. Bo, J. C. Sturm, and D. J. Norris, "On-chip natural assembly of silicon photonic bandgap crystals," *Nature* **414**, 289–293 (2001).

[50] J. D. Jackson, *Classical Electrodynamics* (John Wiley & and Songs, New York, USA, 1975).

[51] A. R. Alija, L. J. Martínez, P. A. Postigo, J. Sánchez-Dehesa, M. Galli, A. Politi, M. Patrini, L. C. Andreani, C. Seassal, and P. Viktorovitch, "Theoretical and experimental study of the suzuki-phase photonic crystal lattice by angle-resolved photoluminescence spectroscopy," *Opt. Express* **15**, 704–713 (2007).

[52] L. J. Martínez, A. R. Alija, P. A. Postigo, J. F. Galisteo-López, M. Galli, L. C. Andreani, C. Seassal, and P. Viktorovitch, "Effect of implementation of a bragg reflector in the photonic band structure of the suzuki-phase photonic crystal lattice," *Opt. Express* **16**, 8509–8518 (2008).

[53] L. C. Andreani and D. Gerace, "Photonic-crystal slabs with a triangular lattice of triangular holes investigated using a guided-mode expansion method," *Phys. Rev. B* **73**, 235114 (2006).

[54] S.-H. Kwon, H.-Y. Ryu, G.-H. Kim, Y.-H. Lee, and S.-B. Kim, "Photonic bandedge lasers in two-dimensional square-lattice photonic crystal slabs," *Appl. Phys. Lett.* **83**, 3870–3872 (2003).

[55] T. Ochiai and K. Sakoda, "Dispersion relation and optical transmittance of a hexagonal photonic crystal slab," *Phys. Rev. B* **63**, 125107 (2001).

[56] S. Fan, W. Suh, and J. D. Joannopoulos, "Temporal coupled-mode theory for the fano resonance in optical resonators," *J. Opt. Soc. Am. A* **20**, 569–572 (2003).

[57] L. J. Martínez, B. Alén, I. Prieto, J. F. Galisteo-López, M. Galli, L. C. Andreani, C. Seassal, P. Viktorovitch, and P. A. Postigo, "Two-dimensional surface emitting photonic crystal laser with hybrid triangular-graphite structure," *Opt. Express* **17**, 15043–15051 (2009).

[58] K. Sakai, E. Miyai, T. Sakaguchi, D. Ohnishi, T. Okano, and S. Noda, "Lasing band-edge identification for a surface-emitting photonic crystal laser," *IEEE J. Select. Areas Commun.,* **23**, 1335–1340 (2005).

[59] H. Matsubara, S. Yoshimoto, H. Saito, Y. Jianglin, Y. Tanaka, and S. Noda, "GaN Photonic-Crystal Surface-Emitting Laser at Blue-Violet Wavelengths," *Science* **319**, 445–447 (2008).

[60] I. Prieto, B. Galiana, P. A. Postigo, C. Algora, L. J. Martínez, and I. Rey-Stolle, "Enhanced quantum efficiency of Ge solar cells by a two-dimensional photonic crystal nanostructured surface," *Appl. Phys. Lett* **94**, 191102 (2009).

[61] L. Tang and T. Yoshie, "Monopole woodpile photonic crystal modes for light-matter interaction and optical trapping," *Opt. Express* **17**, 1346–1351 (2009).

[62] S.-H. Kim, G.-H. Kim, S.-K. Kim, H.-G. Park, Y.-H. Lee, and S.-B. Kim, "Characteristics of a stick waveguide resonator in a two-dimensional photonic crystal slab," *J. Appl. Phys.* **95**, 411–416 (2004).

[63] R. Coccioli, M. Boroditsky, K. Kim, Y. Rahmat-Samii, and E. Yablonovitch, "Smallest possible electromagnetic mode volume in a dielectric cavity," *IEE Proc.-Optoelectron.* - **145**, 391–397 (1998).

[64] K. Nozaki, S. Kita, and T. Baba, "Room temperature continuous wave operation and controlled spontaneous emission in ultrasmall photonic crystal nanolaser," *Opt. Express* **15**, 7506–7514 (2007).

[65] K. Srinivasan and O. Painter, "Momentum space design of high-Q photonic crystal optical cavities," *Opt. Express* **10**, 670–684 (2002).

[66] Y. Takahashi, H. Hagino, Y. Tanaka, B.-S. Song, T. Asano, and S. Noda, "High-Q nanocavity with a 2-ns photon lifetime," *Opt. Express* **15**, 17206–17213 (2007).

[67] S. Combrié, A. D. Rossi, Q. V. Tran, and H. Benisty, "GaAs photonic crystal cavity with ultrahigh Q: microwatt nonlinearity at 1.55 μm," *Opt. Lett.* **33**, 1908–1910 (2008).

[68] F. Bordas, M. J. Steel, C. Seassal, and A. Rahmani, "Confinement of band-edge modes in a photonic crystal slab," *Opt. Express* **15**, 10890–10902 (2007).

[69] R. Hostein, R. Braive, M. Larque, K.-H. Lee, A. Talneau, L. L. Gratiet, I. Robert-Philip, I. Sagnes, and A. Beveratos, "Room temperature spontaneous emission enhancement from quantum dots in photonic crystal slab cavities in the telecommunications C band," *Appl. Phys. Lett.* **94**, 123101 (2009).

[70] L. J. Martínez, B. Alén, I. Prieto, D. Fuster, L. González, Y. González, M. L. Dotor, and P. A. Postigo, "Room temperature continuous wave operation in a photonic crystalmicrocavity laser with a single layer of InAs/InP self-assembled quantum wires," *Opt. Express* **17**, 14993–15000 (2009).

[71] Z. Zhang and M. Qiu, "Small-volume waveguide-section high Q microcavities in 2D photonic crystal slabs," *Opt. Express* **12**, 3988–3995 (2004).

[72] S. Hughes, L. Ramunno, J. F. Young, and J. E. Sipe, "Extrinsic optical scattering loss in photonic crystal waveguides: Role of fabrication disorder and photon group velocity," *Phys. Rev. Lett.* **94**, 033903 (2005).

[73] D. Gerace and L. Andreani, "Low-loss guided modes in photonic crystal waveguides," *Opt. Express* **13**, 4939–4951 (2005).

[74] M. Notomi, K. Yamada, A. Shinya, J. Takahashi, C. Takahashi, and I. Yokohama, "Extremely large group-velocity dispersion of line-defect waveguides in photonic crystal slabs," *Phys. Rev. Lett.* **87**, 253902 (2001).

[75] A. Sugitatsu and S. Noda, "Room temperature operation of 2D photonic crystal slab defect-waveguide laser with optical pump," *Electron. Lett.* **39**, 213–215 (2003).

[76] X. Checoury, P. Boucaud, J.-M. Lourtioz, O. Gauthier-Lafaye, S. Bonnefont, D. Mulin, J. Valentin, F. Lozes-Dupuy, F. Pommereau, C. Cuisin, E. Derouin, O. Drisse, L. Legouezigou, F. Lelarge, F. Poingt, G. H. Duan, and A. Talneau, "1.5 μm room-temperature emission of square-lattice photonic-crystal waveguide lasers with a single line defect," *Appl. Phys. Lett.* **86**, 151111 (2005).

[77] T. Lund-Hansen, S. Stobbe, B. Julsgaard, H. Thyrrestrup, T. Sunner, M. Kamp, A. Forchel, and P. Lodahl, "Experimental realization of highly efficient broadband coupling of single quantum dots to a photonic crystal waveguide," *Phys. Rev. Lett.* **101**, 113903 (2008).

[78] C. Seassal, C. Monat, J. Mouette, E. Touraille, B. Benbakir, H. Hattori, J.-L. Leclercq, X. Letartre, P. Rojo-Romeo, and P. Viktorovitch, "Inp bonded membrane photonics components and circuits: toward 2.5 dimensional micro-nano-photonics," *IEEE J. Sel. Top. Quantum Electron.* **11**, 395–407 (2005).

[79] S. Boutami, B. Benbakir, P. Regreny, J. Leclercq, and P. Viktorovitch, "Compact 1.55 μm room-temperature optically pumped vcsel using photonic crystal mirror," *Electron. Lett.* **43**, 282–283 (2007).

[80] B. B. Bakir, C. Seassal, X. Letartre, P. Regreny, M. Gendry, P. Viktorovitch, M. Zussy, L. D. Cioccio, and J.-M. Fedeli, "Room-temperature InAs/InP quantum dots laser operation based on heterogeneous "2.5 D" photonic crystal," *Opt. Express* **14**, 9269–9276 (2006).

[81] L. Ferrier, O. E. Daif, X. Letartre, P. Rojo-Romeo, C. Seassal, R. Mazurczyk, and P. Viktorovitch, "Surface emitting microlaser based on 2D photonic crystal rod lattices," *Opt. Express* **17**, 9780–9788 (2009).

[82] D. F. Walls and G. J. Milburn, *Quantum Optics* (Springer, 2008), 2nd ed.

[83] Y. Yamamoto and A. Imamoglu, *Mesoscopic Quantum Optics* (John Wiley & and Songs, New York, 1999), 1st ed.

[84] L. C. Andreani, G. Panzarini, and J.-M. Gérard, "Strong-coupling regime for quantum boxes in pillar microcavities: Theory," *Phys. Rev. B* **60**, 13276–13279 (1999).

[85] E. M. Purcell, "Spontaneous emission probabilities at radio frequencies," *Phys. Rev.* **69**, 681 (1946).

[86] T. Baba, "Photonic crystal and microdisk cavities based on GaInAsGa-InP system," *IEEE J. Sel. Top. Quantum Electron.* **3**, 808–830 (1997).

[87] J.-M. Lourtioz, H. Benisty, V. Berger, and J.-M. Gerard, *Photonic Crystals: Towards Nanoscale Photonic Devices* (Springer, 2008), 2nd ed.

[88] E. Peter, P. Senellart, D. Martrou, A. Lemaître, J. Hours, J. M. Gérard, and J. Bloch, "Exciton-photon strong-coupling regime for a single quantum dot embedded in a microcavity," *Phys. Rev. Lett.* **95**, 067401 (2005).

[89] F. P. Laussy, E. del Valle, and C. Tejedor, "Strong coupling of quantum dots in microcavities," *Phys. Rev. Lett.* **101**, 083601 (2008).

[90] Y. Arakawa and H. Sakaki, "Multidimensional quantum well laser and temperature dependence of its threshold current," *Appl. Phys. Lett.* **40**, 939–941 (1982).

[91] R. Dingle, W. Wiegmann, and C. H. Henry, "Quantum states of confined carriers in very thin $Al_xGa_{1-x}As$-GaAs-$Al_xGa_{1-x}As$ heterostructures," *Phys. Rev. Lett.* **33**, 827–830 (1974).

[92] T. Utzmeier, P. A. Postigo, J. Tamayo, R. García, and F. Briones, "Transition from self-organized InSb quantum-dots to quantum dashes," *Appl. Phys. Lett.* **69**, 2674–2676 (1996).

[93] L. González, J. M. García, R. García, F. Briones, J. Martínez-Pastor, and C. Ballesteros, "Influence of buffer-layer surface morphology on the self-organized growth of InAs on InP(001) nanostructures," *Appl. Phys. Lett.* **76**, 1104–1106 (2000).

[94] D. Fuster, B. Alén, L. González, Y. González, J. Martínez-Pastor, M. U. González, and J. M. García, "Isolated self-assembled InAs/InP(001) quantum wires obtained by controlling the growth front evolution," *Nanotechnology* **18**, 035604 (2007).

[95] B. Alén, J. Martínez-Pastor, A. García-Cristobal, L. González, and J. M. García, "Optical transitions and excitonic recombination in InAs/InP self-assembled quantum wires," *Appl. Phys. Lett.* **78**, 4025–4027 (2001).

[96] J. Y. Marzin, J. M. Gérard, A. Izraël, D. Barrier, and G. Bastard, "Photoluminescence of single InAs quantum dots obtained by self-organized growth on GaAs," *Phys. Rev. Lett.* **73**, 716–719 (1994).

[97] A. Yariv, "Scaling laws and minimum threshold currents for quantum-confined semiconductor lasers," *Appl. Phys. Lett.* **53**, 1033–1035 (1988).

[98] C. Weisbuch, M. Nishioka, A. Ishikawa, and Y. Arakawa, "Observation of the coupled exciton-photon mode splitting in a semiconductor quantum microcavity," *Phys. Rev. Lett.* **69**, 3314–3317 (1992).

[99] H. Deng, G. Weihs, C. Santori, J. Bloch, and Y. Yamamoto, "Condensation of Semiconductor Microcavity Exciton Polaritons," *Science* **298**, 199–202 (2002).

[100] J. Kasprzak, M. Richard, S. Kundermann, A. Baas, P. Jeambrun, J. M. J. Keeling, F. M. Marchetti, M. H. Szymańska, R. André, J. L. Staehli, V. Savona, P. B. Littlewood, B. Deveaud, and L. S. Dang, "BoseEinstein condensation of exciton polaritons," *Nature* **443**, 409–414 (2006).

[101] A. Shinya, S. Matsuo, Yosia, T. Tanabe, E. Kuramochi, T. Sato, T. Kakitsuka, and M. Notomi, "All-optical on-chip bit memory based on ultra high Q InGaAsP photonic crystal," *Opt. Express* **16**, 19382–19387 (2008).

[102] D. Gerace and L. C. Andreani, "Effects of disorder on propagation losses and cavity Q-factors in photonic crystal slabs," *Photon. Nanostruct. Fundam. Appl.* **3**, 120–128 (2005).

[103] T. Asano, B.-S. Song, and S. Noda, "Analysis of the experimental Q factors (∼1 million) of photonic crystal nanocavities," *Opt. Express* **14**, 1996–2002 (2006).

[104] L. González, J. M. García, R. García, F. Briones, J. Martínez-Pastor, and C. Ballesteros, "Influence of buffer-layer surface morphology on the self-organized growth of InAs on InP(001) nanostructures," *Appl. Phys. Lett.* **76**, 1104–1106 (2000).

[105] D. Fuster, A. Rivera, B. Alén, P. Alonso-González, Y. González, and L. González, "Direct formation of InAs quantum dots grown on InP (001) by solid-source molecular beam epitaxy," *Appl. Phys. Lett.* **94**, 133106 (2009).

[106] L. Andreani and M. Agio, "Photonic bands and gap maps in a photonic crystal slab," *IEEE J. Quantum Electron.,* **38**, 891–898 (2002).

[107] Y.-S. Choi, K. Hennessy, R. Sharma, E. Haberer, Y. Gao, S. P. DenBaars, S. Nakamura, E. L. Hu, and C. Meier, "GaN blue photonic crystal membrane nanocavities," *Appl. Phys. Lett.* **87**, 243101 (2005).

[108] C. F. Wang, R. Hanson, D. D. Awschalom, E. L. Hu, T. Feygelson, J. Yang, and J. E. Butler, "Fabrication and characterization of two-dimensional photonic crystal microcavities in nanocrystalline diamond," *Appl. Phys. Lett.* **91**, 201112 (2007).

[109] *Lumerical Solutions, Inc.,* Vancouver, BC, Canada, (2006).

[110] M. Galli, S. L. Portalupi, M. Belotti, L. C. Andreani, L. O'Faolain, and T. F. Krauss, "Light scattering and fano resonances in high-Q photonic crystal nanocavities," *Appl. Phys. Lett.* **94**, 071101 (2009).

[111] M. Borselli, T. Johnson, and O. Painter, "Beyond the rayleigh scattering limit in high-Q silicon microdisks: theory and experiment," *Opt. Express* **13**, 1515–1530 (2005).

[112] K. Hennessy, C. Reese, A. Badolato, C. F. Wang, A. Imamoglu, P. M. Petroff, and E. Hu, "Fabrication of high Q square-lattice photonic crystal microcavities," *J. Vac. Sci. Technol. B* **21**, 2918–2921 (2003).

[113] D. Sarkar, L. J. Martínez, I. Prieto-González, H. van der Meulen, J. M. Calleja, D. Granados, A. G. Taboada, J. García, A. Alija, and P. A. Postigo, "Optical emission of InAs/GaAs quantum rings coupled to a two-dimensional photonic crystal microcavity," *Physica E: Low-dimensional Systems and Nanostructures* **40**, 2156 – 2159 (2008). 13th International Conference on Modulated Semiconductor Structures.

[114] S. A. Rishton and D. P. Kern, "Point exposure distribution measurements for proximity correction in electron beam lithography on a sub-100 nm scale," *J. Vac. Sci. Technol. B* **5**, 135–141 (1987).

[115] M. Parikh and D. F. Kyser, "Energy deposition functions in electron resist films on substrates," *J. Appl. Phys.* **50**, 1104–1111 (1979).

[116] L. Stevens, R. Jonckheere, E. Froyen, S. Decoutere, and D. Lanneer, "Determination of the proximity parameters in electron beam lithography using doughnut-structures," *Microelectron. Eng.* **5**, 141–150 (1986).

[117] R. Wüest, P. Strasser, M. Jungo, F. Robin, D. Erni, and H. Jäckel, "An efficient proximity-effect correction method for electron-beam patterning of photonic-crystal devices," *Microelectron. Eng.* **67-68**, 182 – 188 (2003). Proceedings of the 28th International Conference on Micro- and Nano-Engineering.

[118] C. Dix, P. G. Flavin, P. Hendy, and M. E. Jones, "0.1 μm scale lithography using a conventional electron beam system," *J. Vac. Sci. Technol. B* **3**, 131–135 (1985).

[119] J. R. Sendra and J. Anguita, "Reactive ion beam etching of indium phosphide in electron cyclotron resonance plasma using methane/hydrogen/nitrogen mixtures," *Jpn. J. Appl. Phys.* Pt. 2, Letters **33**, L390–L393 (1994).

[120] P. Strasser, R. Wüest, F. Robin, D. Erni, and H. Jäckel, "Detailed analysis of the influence of an inductively coupled plasma reactive-ion etching process on the hole depth and shape of photonic crystals in InP/InGaAsP," *J. Vac. Sci. Technol. B* **25**, 387–393 (2007).

[121] J. Werking, J. Schramm, C. Nguyen, E. L. Hu, and H. Kroemer, "Methane/hydrogen-based reactive ion etching of InAs, InP, GaAs, and GaSb," *Appl. Phys. Lett.* **58**, 2003–2005 (1991).

[122] J. S. Yu and Y. T. Lee, "Parametric reactive ion etching of InP using Cl_2 and CH_4 gases: effects of H_2 and Ar addition," *Semicond. Sci. Technol.* **17**, 230–236 (2002).

[123] J. E. Schramm, D. I. Babić, E. L. Hu, J. E. Bowers, and J. L. Merz, "Fabrication of high-aspect-ratio InP-based vertical-cavity laser mirrors using $CH_4/H_2/O_2/Ar$ reactive ion etching," *J. Vac. Sci. Technol. B* **15**, 2031–2036 (1997).

[124] A. Xing, M. Davanco, D. J. Blumenthal, and E. L. Hu, "Fabrication of InP-based two-dimensional photonic crystal membrane," *J. Vac. Sci. Technol. B* **22**, 70–73 (2004).

[125] M. V. Kotlyar, T. Karle, M. D. Settle, L. O'Faolain, and T. F. Krauss, "Low-loss photonic crystal defect waveguides in InP," *Appl. Phys. Lett.* **84**, 3588–3590 (2004).

[126] D. I. Elder and A. R. Clawson, "Determination of $In_{0.53}Ga_{0.47}As$ layer thicknesses from ethched steps," *J. Mater. Sci. Lett.* **3**, 340 (1984).

[127] K. Srinivasan, P. E. Barclay, O. Painter, J. Chen, and A. Y. Cho, "Fabrication of high-quality-factor photonic crystal microcavities in InAsP/InGaAsP membranes," *J. Vac. Sci. Technol. B* **22**, 875–879 (2004).

[128] S. Frédérick, D. Dalacu, J. Lapointe, P. J. Poole, G. C. Aers, and R. L. Williams, "Experimental demonstration of high quality factor, x-dipole modes in InAs/InP quantum dot photonic crystal microcavity membranes," *Appl. Phys. Lett.* **89**, 091115 (2006).

[129] A. R. Alija, L. J. Martínez, A. García-Martín, M. L. Dotor, D. Golmayo, and P. A. Postigo, "Tuning of spontaneous emission of two-dimensional photonic crystal microcavities by accurate control of slab thickness," *Appl. Phys. Lett.* **86**, 141101 (2005).

[130] C. Monat, C. Seassal, X. Letartre, P. Regreny, M. Gendry, P. Rojo-Romeo, P. Viktorovitch, M. L. V. d'Yerville, D. Cassagne, J. P. Albert, E. Jalaguier, S. Pocas, and B. Aspar, "Two-dimensional hexagonal-shaped microcavities formed in a two-dimensional photonic crystal on an InP membrane," *J. Appl. Phys.* **93**, 23–31 (2003).

[131] A. R. Alija, L. J. Martínez, P. A. Postigo, C. Seassal, and P. Viktorovitch, "Coupled-cavity two-dimensional photonic crystal waveguide ring laser," *Appl. Phys. Lett.* **89**, 101102 (2006).

[132] L. J. Martínez, A. Alija, C. Seassal, P. Viktorovitch, and P. Postigo, "Modal suppression and single-mode emission in photonic crystal coupled-cavity ring-like lasers," in "Electron Devices, 2007 Spanish Conference on," (2007), pp. 266–269.

[133] A. R. Alija, "Fabricación de nanoestructuras semiconductoras con banda prohibida para fotones y su aplicación a dispositivos optoelectrónicos integrados," Ph.D. thesis, Universidad Politénica de Madrid (2007).

[134] S. Boutami, B. Bakir, J.-L. Leclercq, X. Letartre, C. Seassal, P. Rojo-Romeo, P. Regreny, M. Garrigues, and P. Viktorovitch, "Photonic crystal-based MOEMS devices," *IEEE J. Sel. Top. Quantum Electron.* **13**, 244–252 (2007).

[135] D. Englund, A. Faraon, I. Fushman, N. Stoltz, P. Petroff, and J. Vučković, "Controlling cavity reflectivity with a single quantum dot," *Nature* **450**, 857–861 (2007).

[136] T.-C. Lu, S.-W. Chen, L.-F. Lin, T.-T. Kao, C.-C. Kao, P. Yu, H.-C. Kuo, S.-C. Wang, and S. Fan, "GaN-based two-dimensional surface-emitting photonic crystal lasers with AlN/GaN distributed bragg reflector," *Appl. Phys. Lett.* **92**, 011129 (2008).

[137] L. Ferrier, P. Rojo-Romeo, E. Drouard, X. Letatre, and P. Viktorovitch, "Slow bloch mode confinement in 2D photonic crystals for surface operating devices," *Opt. Express* **16**, 3136–3145 (2008).

[138] D. Cassagne, C. Jouanin, and D. Bertho, "Photonic band gaps in a two-dimensional graphite structure," *Phys. Rev. B* **52**, R2217–R2220 (1995).

[139] L. J. Martínez, A. García-Martín, and P. Postigo, "Photonic band gaps in a two-dimensional hybrid triangular-graphite lattice," *Opt. Express* **12**, 5684–5689 (2004).

[140] S. David, A. Chelnikov, and J.-M. Lourtioz, "Isotropic photonic structures: Archimedean-like tilings and quasi-crystals," *IEEE J. Quantum Electron.* **37**, 1427–1434 (2001).

[141] H. Altug and J. Vučković, "Two-dimensional coupled photonic crystal resonator arrays," *Appl. Phys. Lett.* **84**, 161–163 (2004).

[142] C. Monat, C. Seassal, X. Letartre, P. Regreny, P. Rojo-Romeo, P. Viktorovitch, M. d'Yerville, D. Cassagne, J. Albert, E. Jalaguier, S. Pocas, and B. Aspar, "Modal analysis and engineering on InP-based two-dimensional photonic-crystal microlasers on a Si wafer," *IEEE J. Quantum Electron.* **39**, 419–425 (2003).

[143] S. G. Johnson, S. Fan, P. R. Villeneuve, J. D. Joannopoulos, and L. A. Kolodziejski, "Guided modes in photonic crystal slabs," *Phys. Rev. B* **60**, 5751–5758 (1999).

[144] V. N. Astratov, D. M. Whittaker, I. S. Culshaw, R. M. Stevenson, M. S. Skolnick, T. F. Krauss, and R. M. De La Rue, "Photonic band-structure effects in the reflectivity of periodically patterned waveguides," *Phys. Rev. B* **60**, R16255–R16258 (1999).

[145] M. Galli, M. Agio, L. C. Andreani, M. Belotti, G. Guizzetti, F. Marabelli, M. Patrini, P. Bettotti, L. Dal Negro, Z. Gaburro, L. Pavesi, A. Lui, and P. Bellutti, "Spectroscopy of photonic bands in macroporous silicon photonic crystals," *Phys. Rev. B* **65**, 113111 (2002).

[146] A. David, C. Meier, R. Sharma, F. S. Diana, S. P. DenBaars, E. Hu, S. Nakamura, C. Weisbuch, and H. Benisty, "Photonic bands in two-dimensionally patterned multimode GaN waveguides for light extraction," *Appl. Phys. Lett.* **87**, 101107 (2005).

[147] M. Galli, A. Politi, M. Belotti, D. Gerace, M. Liscidini, M. Patrini, L. C. Andreani, M. Miritello, A. Irrera, F. Priolo, and Y. Chen, "Strong enhancement of Er^{3+} emission at room temperature in silicon-on-insulator photonic crystal waveguides," *Appl. Phys. Lett.* **88**, 251114 (2006).

[148] S.-H. Kim, H.-Y. Ryu, H.-G. Park, G.-H. Kim, Y.-S. Choi, Y.-H. Lee, and J.-S. Kim, "Two-dimensional photonic crystal hexagonal waveguide ring laser," *Appl. Phys. Lett.* **81**, 2499–2501 (2002).

[149] X. Letartre, C. Monat, C. Seassal, and P. Viktorovitch, "Analytical modeling and an experimental investigation of two-dimensional photonic crystal microlasers: defect state (microcavity) versus band-edge state (distributed feedback) structures," *J. Opt. Soc. Am. B* **22**, 2581–2595 (2005).

[150] H. Altug and J. Vučković, "Photonic crystal nanocavity array laser," *Opt. Express* **13**, 8819–8828 (2005).

[151] Y. Park, S. Kim, C. Moon, H. Jeon, and H. J. Kim, "Butt-end fiber coupling to a surface-emitting gamma-point photonic crystal band edge laser," *Appl. Phys. Lett.* **90**, 171115 (2007).

[152] C. M. Anderson and K. P. Giapis, "Larger two-dimensional photonic band gaps," *Phys. Rev. Lett.* **77**, 2949–2952 (1996).

[153] T. Trifonov, L. F. Marsal, A. Rodríguez, J. Pallarès, and R. Alcubilla, "Effects of symmetry reduction in two-dimensional square and triangular lattices," *Phys. Rev. B* **69**, 235112 (2004).

[154] B. Song, S. Noda, T. Asano, and Y. Akahane, "Ultra-high-Q photonic double-heterostructure nanocavity," *Nature Materials* **4**, 207–210 (2005).

[155] S. Johnson and J. Joannopoulos, "Block-iterative frequency-domain methods for maxwell's equations in a planewave basis," *Opt. Express* **8**, 173–190 (2001).

[156] S.-H. Kim and Y.-H. Lee, "Symmetry relations of two-dimensional photonic crystal cavity modes," *IEEE J. Quantum Electron.* **39**, 1081–1085 (2003).

[157] L. J. Martínez, I. Prieto, B. Alén, and P. A. Postigo, "Fabrication of high quality factor photonic crystal microcavities in InAsP/InP membranes combining reactive ion beam etching and reactive ion etching," *J. Vac. Sci. Technol. B* **27**, 1801–1804 (2009).

[158] T. Baba and D. Sano, "Low-threshold lasing and purcell effect in microdisk lasers at room temperature," *IEEE J. Sel. Top. Quantum Electron.* **9**, 1340–1346 (2003).

[159] E. D. Palik, *Handbook of Optical Constants of Solids* (Academic Press, INC., Orlando, Florida, USA, 1985).

[160] K. Srinivasan, P. E. Barclay, O. Painter, J. Chen, A. Y. Cho, and C. Gmachl, "Experimental demonstration of a high quality factor photonic crystal microcavity," *Appl. Phys. Lett.* **83**, 1915–1917 (2003).

[161] C. Wilmsen, H. Temkin, and L. A. Coldren, *Vertical-Cavity Surface-Emitting Lasers* (Cambridge University Press, Cambridge, UK, 1999).

[162] D. Kuksenkov, S. Feld, C. Wilmsen, H. Temkin, S. Swirhun, and R. Leibenguth, "Linewidth and alpha-factor in AlGaAs/GaAs vertical cavity surface emitting lasers," *Appl. Phys. Lett.* **66**, 277–279 (1995).

[163] F. Raineri, C. Cojocaru, R. Raj, P. Monnier, A. Levenson, C. Seassal, X. Letartre, and P. Viktorovitch, "Tuning a two-dimensional photonic crystal resonance via optical carrierinjection," *Opt. Lett.* **30**, 64–66 (2005).

[164] F. Bordas, C. Seassal, E. Dupuy, P. Regreny, M. Gendry, P. Viktorovitch, M. J. Steel, and A. Rahmani, "Room temperature low-threshold InAs/InP quantum dot single mode photonic crystal microlasers at 1.5 μm using cavity-confined slow light," *Opt. Express* **17**, 5439–5445 (2009).

[165] M. Asada, Y. Miyamoto, and Y. Suematsu, "Theoretical gain of quantum-well wire lasers," *Jpn. J. Appl. Phys.* **24**, L95–L97 (1985).

[166] Y. Arakawa, K. Vahala, A. Yariv, and K. Lau, "Reduction of the spectral linewidth of semiconductor lasers with quantum wire effects—spectral properties of GaAlAs double heterostructure lasers in high magnetic fields," *Appl. Phys. Lett.* **48**, 384–386 (1986).

[167] C. Seassal, X. Letartre, J. Brault, M. Gendry, P. Pottier, P. Viktorovitch, O. Piquet, P. Blondy, D. Cros, and O. Marty, "InAs quantum wires in InP-based microdisks: Mode identification and continuous wave room temperature laser operation," *J. Appl. Phys.* **88**, 6170–6174 (2000).

[168] D. Fuster, L. González, Y. González, M. U. González, and J. Martínez-Pastor, "Size and emission wavelength control of InAs/InP quantum wires," *J. Appl. Phys.* **98**, 033502 (2005).

[169] R. Schwertberger, D. Gold, J. Reithmaier, and A. Forchel, "Long-wavelength InP-based quantum-dash lasers," *IEEE Photon. Technol. Lett.,* **14**, 735–737 (2002).

[170] K. A. Atlasov, K. F. Karlsson, E. Deichsel, A. Rudra, B. Dwir, and E. Kapon, "Site-controlled single quantum wire integrated into a photonic-crystal membrane microcavity," *Appl. Phys. Lett.* **90**, 153107 (2007).

[171] J. Hendrickson, B. C. Richards, J. Sweet, S. Mosor, C. Christenson, D. Lam, G. Khitrova, H. M. Gibbs, T. Yoshie, A. Scherer, O. B. Shchekin, and D. G. Deppe, "Quantum dot photonic-crystal-slab nanocavities: Quality factors and lasing," *Phys. Rev. B* **72**, 193303 (2005).

[172] T. Yoshie, O. Shchekin, H. Chen, D. Deppe, and A. Scherer, "Quantum dot photonic crystal lasers," *Electron. Lett.* **38**, 967–968 (2002).

[173] M. Nomura, S. Iwamoto, K. Watanabe, N. Kumagai, Y. Nakata, S. Ishida, and Y. Arakawa, "Room temperature continuous-wave lasing in photonic crystal nanocavity," *Opt. Express* **14**, 6308–6315 (2006).

[174] M. Nomura, S. Iwamoto, N. Kumagai, and Y. Arakawa, "Temporal coherence of a photonic crystal nanocavity laser with high spontaneous emission coupling factor," *Physical Review B* **75**, 195313 (2007).

[175] J. Hwang, H. Ryu, D. Song, I. Han, H. Park, D. Jang, and Y. Lee, "Continuous room-temperature operation of optically pumped two-dimensional photonic crystal lasers at 1.6 μm," *IEEE Photon. Technol. Lett.* **12**, 1295–1297 (2000).

[176] L. C. Andreani and M. Agio, "Intrinsic diffraction losses in photonic crystal waveguides with line defects," *Appl. Phys. Lett.* **82**, 2011–2013 (2003).

[177] Y.-S. Choi, M. T. Rakher, K. Hennessy, S. Strauf, A. Badolato, P. M. Petroff, D. Bouwmeester, and E. L. Hu, "Evolution of the onset of coherence in a family of photonic crystal nanolasers," *Appl. Phys. Lett.* **91**, 031108 (2007).

[178] A. R. A. Chalcraft, S. Lam, D. O'Brien, T. F. Krauss, M. Sahin, D. Szymanski, D. Sanvitto, R. Oulton, M. S. Skolnick, A. M. Fox, D. M. Whittaker, H.-Y. Liu, and M. Hopkinson, "Mode structure of the L3 photonic crystal cavity," *Appl. Phys. Lett.* **90**, 241117 (2007).

[179] M. Richard, J. Kasprzak, R. Romestain, R. André, and L. S. Dang, "Spontaneous coherent phase transition of polaritons in cdte microcavities," *Phys. Rev. Lett.* **94**, 187401 (2005).

[180] K. A. Atlasov, K. F. Karlsson, P. Gallo, A. Rudra, B. Dwir, and E. Kapon, *Observation of stimulated emission and lasing in quantum-wire photonic-crystal nanocavities*, *IEEE/LEOS Winter Topicals Meeting Series,* 2009.

[181] J. Canet-Ferrer, G. Muñoz Matutano, L. J. Martínez, B. Alén, J. Martínez-Pastor, I. Prieto, P. Postigo, D. Fuster, Y. González, and L. González, "Photoluminescence and time resolved photoluminescence of InAs/InP quantum wires embedded in photonic crystal microcavities," (2009). Manuscript in preparation.

[182] K. Nozaki, A. Nakagawa, D. Sano, and T. Baba, "Ultralow threshold and single-mode lasing in microgear lasers and its fusion with quasi-periodic photonic crystals," *IEEE J. Sel. Top. Quantum Electron.* **9**, 1355–1360 (2003).

[183] H. Y. Ryu, M. Notomi, E. Kuramoti, and T. Segawa, "Large spontaneous emission factor (>0.1) in the photonic crystal monopole-mode laser," *Appl. Phys. Lett.* **84**, 1067–1069 (2004).

[184] K. Tanabe, M. Nomura, D. Guimard, S. Iwamoto, and Y. Arakawa, "Room temperature continuous wave operation of InAs/GaAs quantum dot photonic crystal nanocavity laser on silicon substrate," *Opt. Express* **17**, 7036–7042 (2009).

[185] L. A. Coldren and S. W. Corzine, *Diode Lasers and Photonic Integrated Circuits* (Wiley-Interscience, New York, 1995), 1st ed.

[186] D. Englund, H. Altug, and J. Vučković, "Time-resolved lasing action from single and coupled photonic crystal nanocavity array lasers emitting in the telecom band," *J. Appl. Phys.* **105**, 093110 (2009).

[187] Y. Yamamoto, C. Santori, G. Solomon, J. Vučković, D. Fattal, E. Waks, and E. Diamanti, "Single photons for quantum information systems," *Progress in Informatics* **1**, 5–37 (2005).

[188] B. Sanders, J. Vučković, and P. Grangier, "Single photons on demand," *Europhysics News* **36**, 56–58 (2005).

[189] C. Santori, M. Pelton, G. Solomon, Y. Dale, and Y. Yamamoto, "Triggered single photons from a quantum dot," *Phys. Rev. Lett.* **86**, 1502–1505 (2001).

[190] C. Santori, D. Fattal, J. Vuckovic, G. S. Solomon, and Y. Yamamoto, "Single-photon generation with InAs quantum dots," *New J. Phys.* **6**, 89 (2004).

[191] S. Laurent, S. Varoutsis, L. L. Gratiet, A. Lemaître, I. Sagnes, F. Raineri, A. Levenson, I. Robert-Philip, and I. Abram, "Indistinguishable single photons from a single-quantum dot in a two-dimensional photonic crystal cavity," *Appl. Phys. Lett.* **87**, 163107 (2005).

[192] D. Englund, A. Faraon, I. Fushman, and J. Vučković, "Single photon nonlinear optics on photonic crystal chips," *SPIE Newsroom* (2009).

[193] I. Fushman, D. Englund, A. Faraon, N. Stoltz, P. Petroff, and J. Vuckovic, "Controlled Phase Shifts with a Single Quantum Dot," *Science* **320**, 769–772 (2008).

[194] R. Johne, N. A. Gippius, G. Pavlovic, D. D. Solnyshkov, I. A. Shelykh, and G. Malpuech, "Entangled photon pairs produced by a quantum dot strongly coupled to a microcavity," *Phys. Rev. Lett.* **100**, 240404 (2008).

[195] M. Nomura, N. Kumagai, S. Iwamoto, Y. Ota, and Y. Arakawa, "Photonic crystal nanocavity laser with a single quantum dot gain," *Opt. Express* **17**, 15975–15982 (2009).

[196] H. Pettersson, R. J. Warburton, A. Lorke, K. Karrai, J. P. Kotthausa, J. M. García, and P. M. Petroff, "Excitons in self-assembled quantum ring-like structures," *Physica E: Low-dimensional Systems and Nanostructures* **6**, 510–513 (2000).

[197] A. Lorke, R. Johannes Luyken, A. O. Govorov, J. P. Kotthaus, J. M. García, and P. M. Petroff, "Spectroscopy of nanoscopic semiconductor rings," *Phys. Rev. Lett.* **84**, 2223–2226 (2000).

[198] K. Hennessy, C. Högerle, E. Hu, A. Badolato, and A. Imamoğlu, "Tuning photonic nanocavities by atomic force microscope nano-oxidation," *Appl. Phys. Lett.* **89**, 041118 (2006).

[199] D. Granados and J. M. García, "In(Ga)As self-assembled quantum ring formation by molecular beam epitaxy," *Appl. Phys. Lett.* **82**, 2401–2403 (2003).

[200] P. Offermans, P. M. Koenraad, J. H. Wolter, D. Granados, J. M. García, V. M. Fomin, V. N. Gladilin, and J. T. Devreese, "Atomic-scale structure of self-assembled In(Ga)As quantum rings in GaAs," *Appl. Phys. Lett.* **87**, 131902 (2005).

[201] N. A. J. M. Kleemans, I. M. A. Bominaar-Silkens, V. M. Fomin, V. N. Gladilin, D. Granados, A. G. Taboada, J. M. García, P. Offermans, U. Zeitler, P. C. M. Christianen, J. C. Maan, J. T. Devreese, and P. M. Koenraad, "Oscillatory persistent currents in self-assembled quantum rings," *Phys. Rev. Lett.* **99**, 146808 (2007).

[202] K. Hennessy, A. Badolato, P. Petroff, and E. Hu, "Positioning photonic crystal cavities to single InAs quantum dots," *Photon. Nanostruct. Fundam. Appl.* **2**, 65 – 72 (2004).

[203] D. G. Gevaux, A. J. Bennett, R. M. Stevenson, A. J. Shields, P. Atkinson, J. Griffiths, D. Anderson, G. A. C. Jones, and D. A. Ritchie, "Enhancement and suppression of spontaneous emission by temperature tuning InAs quantum dots to photonic crystal cavities," *Appl. Phys. Lett.* **88**, 131101 (2006).

[204] R. Wüest, P. Strasser, F. Robin, D. Erni, and H. Jäckel, "Fabrication of a hard mask for InP based photonic crystals: Increasing the plasma-etch selectivity of poly(methyl methacrylate) versus SiO_2 and SiN_x," *J. Vac. Sci. Technol. B* **23**, 3197–3201 (2005).

[205] M. Shirane, S. Kono, J. Ushida, S. Ohkouchi, N. Ikeda, Y. Sugimoto, and A. Tomita, "Mode identification of high-quality-factor single-defect nanocavities in quantum dot-embedded photonic crystals," *J. Appl. Phys.* **101**, 073107 (2007).

[206] E. Gallardo, L. Martínez, A. K. Nowak, D. Sarkar, D. Sanvitto, H. van der Meulen, J. Calleja, I. Prieto, A. Alija, D. Granados, A. Taboada, J. García, and P. Postigo, "Single photon emission by semiconductor quantum rings in a photonic crystal," (2009). Submitted to *Opt. Lett.*

[207] S.-H. Kwon, S.-H. Kim, S.-K. Kim, Y.-H. Lee, and S.-B. Kim, "Small, low-loss heterogeneous photonic bandedge laser," *Opt. Express* **12**, 5356–5361 (2004).